UNDERSTANDING THE ELECTRONIC STRUCTURE OF $LiFePO_4$ AND $FePO_4$

A Thesis Submitted to the
College of Graduate Studies and Research
in Partial Fulfillment of the Requirements
for the degree of Master of Science
in the Department of Physics and Engineering Physics
University of Saskatchewan
Saskatoon

By
Adrian Hunt

Permission to Use

In presenting this thesis in partial fulfilment of the requirements for a Postgraduate degree from the University of Saskatchewan, I agree that the Libraries of this University may make it freely available for inspection. I further agree that permission for copying of this thesis in any manner, in whole or in part, for scholarly purposes may be granted by the professor or professors who supervised my thesis work or, in their absence, by the Head of the Department or the Dean of the College in which my thesis work was done. It is understood that any copying or publication or use of this thesis or parts thereof for financial gain shall not be allowed without my written permission. It is also understood that due recognition shall be given to me and to the University of Saskatchewan in any scholarly use which may be made of any material in my thesis.

Requests for permission to copy or to make other use of material in this thesis in whole or part should be addressed to:

Head of the Department of Physics and Engineering Physics
116 Science Place
University of Saskatchewan
Saskatoon, Saskatchewan
Canada
S7N 5E2

ABSTRACT

This thesis has detailed the extensive analysis of the XAS and RIXS spectra of $LiFePO_4$ and $FePO_4$, with the primary focus on $LiFePO_4$. One of the primary motivations for this study was to understand the electronic structure of the two compounds and, in particular, shed some light on the nature of electron correlation within the samples. Two classes of band structure calculations have come to light. One solution uses the Hubbard U parameter, and this solution exhibits a band gap of about 4 eV. Other solutions that use standard DFT electron correlation functionals yield band gaps between 0 and 1.0 eV.

The RIXS spectra of $LiFePO_4$ and $FePO_4$ were analyzed using Voigt function fitting, an uncommon practice for RIXS spectra. Each of the spectra was fit to a series of Voigt functions in an attempt to localize the peaks within the spectra. These peaks were determined to be RIXS events, and the energetic centers of these peaks were compared to a small band gap band structure calculation. The results of the RIXS analysis strongly indicate that the small gap solution is correct. This was a surprising result, given that $LiFePO_4$ is an ionic, insulating transition metal oxide, showing all of the usual traits of a Mott-type insulator.

This contradiction was explained in terms of polaron formation. Polarons can severely distort the lattice, which changes the local charge density. This changes the local DOS such that the DOS probed by XAS or RIXS experiments is not necessarily in the ground state. In particular, polaron formation can reduce the band gap. Thus, the agreement between the small gap solution and experiment is false, in the sense that the physical assumptions that formed the basis of the small gap calculations do not reflect reality. Polaronic distortion was also tentatively put forward as an explanation for the discrepancy between partial fluorescence yield, total fluorescence yield, and total electron yield measurements of the XAS spectra of $LiFePO_4$ and $FePO_4$.

ACKNOWLEDGEMENTS

I would like to thank my supervisor, Alex Moewes. His professional and scientific guidance were invaluable, and he always remained supportive, even during my mother's illness in my second year of study. Also invaluable to my research were my collaborators Yet-Ming Chiang, from the Massachusetts Institute of Technology, and Wai-Yim Ching, from the University of Missouri-Kansas City. Yet-Ming produced the samples, and Wai-Yim did the calculations. Without their aid, my thesis research would never have been started.

I would like to thank my coworkers. They listened to my presentations and back-of-the-envelope ideas, and always they were supportive and had excellent ideas on how to proceed from seemingly dead ends of research.

I would like to thank my lovely wife Jodi as well as my parents, Jeanette and William. Although their support was much less technical, they all nevertheless drove me to succeed. I can be incredibly stubborn, but they persevered and helped show me the way. Always caring and always humble, they never lost faith in me when I stumbled.

Contents

List of Tables

List of Figures

List of Abbreviations

ALS	Advanced Light Source
CCD	Charge Coupled Device
DFT	Density Functional Theory
DOS	Density of States
EMA	Ellipsoidal-Mirror electron energy Analyzer
FWHM	Full Width at Half Maximum
LDA	Local Density Approximation
MCP	Multi-channel Plate
OLCAO	Orthogonal Linear Combination of Atomic Orbitals
PDOS	Partial Density of States
PFY	Partial Fluorescence Yield
RIXS	Resonant Inelastic X-ray Scattering
SXF	Soft X-ray Fluorescence
TEY	Total Electron Yield
TFY	Total Fluorescence Yield
UHV	Ultra High Vacuum
XAS	X-ray Absorption Spectroscopy
XES	X-ray Emission Spectroscopy

Part I

Introduction and Background

Chapter 1

Motivation

The overarching goal of material science, simply stated, is to understand the physics underlying the structural and electronic environments that give rise to macroscopic properties such as electrical and thermal conductivity, structural strength, and magnetic susceptibility, among many others. If researchers can realize this goal, it may eventually be possible to custom synthesize materials that have been purposefully designed to meet a certain need. Historically, the process of discovering new materials has relied heavily on trial and error. However, in recent years, researchers in physics and chemistry have begun to put forward new materials that are designed to have certain properties. As the fundamental interactions in condensed matter are understood, this knowledge fuels ever more accurate simulations of crystalline systems. One such system is $LiFePO_4$.

$LiFePO_4$ is one of several candidate materials that was proposed as an electrode material for use in Li-ion batteries [1, 2]. In particular, $LiFePO_4$ would serve as the cathode in a Li-ion cell. When the cell is charged, Li^+ ions are removed from the cathode material and stored in the anode, which is often made of carbon. Ideally, the cathode has a deficiency in Li^+ ions that is equal to the surplus in the anode, which means that the cathode is partially $FePO_4$. During discharge, the Li^+ ions leave the anode and return to the $LiFePO_4$ crystal, and the electrons, which required to change the oxidation state of the Fe ions from 3+ to 2+, flow through an externally connected circuit. It is called delithiation when the Li^+ ions are removed from $LiFePO_4$. When the Li^+ ions are reintroduced to $FePO_4$ to form $LiFePO_4$, this is called intercalation.

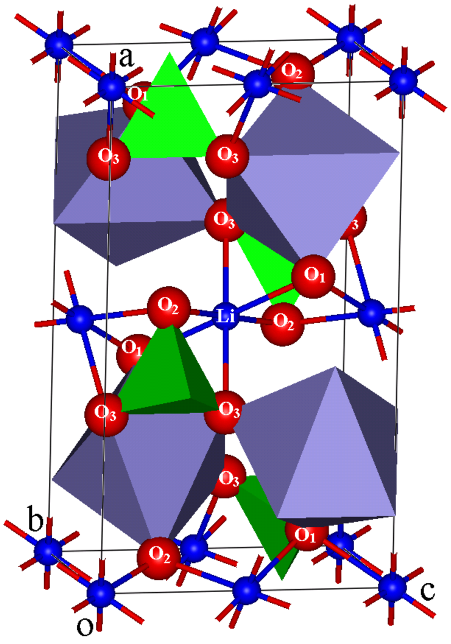

Figure 1.1: Crystal structure of $LiFePO_4$. The O and Li sites are represented by the red and blue spheres, respectively. The blue octahedra surround the Fe ions. O3-symmetry sites sit at the four equatorial corners, with one O1 site and one O2 site occupying the two other positions, respectively. The green tetrahedra surround the P atoms; the P atoms and the surrounding tetrahedra of oxygen form tightly bound, covalently bonded polyatomic anions. The unit cell axes are labeled with the letters a, b, and c. This image was adapted from Ref. 3.

$LiFePO_4$ has received much attention because it has several advantageous properties. Firstly, it is chemically stable, which is a necessary property if one does not want the electrode to degrade within the cell. Secondly, the volume that a $LiFePO_4$ electrode occupies changes very little upon delithiation. The crystal structure of $LiFePO_4$, shown in Figure 1.1, closely resembles the olivine type structure. Naturally occurring $FePO_4$ and $FePO_4$ that is produced by delithiating $LiFePO_4$ have very different crystal structures, however the latter has a crystal structure identical to that of $LiFePO_4$, only it has a slightly reduced volume. This property is desirable because it reduces the amount of mechanical stress that the cell must endure during normal operation. Thirdly, $LiFePO_4$ has a high intercalation voltage of 3.5 V relative to lithium metal, and fourthly, it has a high theoretical discharge capacity ($\approx$170 mA h g^{-1}). These two properties taken together mean that $LiFePO_4$ has a

Table 1.1: Pertinent information presented by other authors

Author	Correlation?	Band gap
Xu *et al.* [3, 16]	No	0 eV
Tang and Holzwarth [17]	No	0 eV
Shi *et al.* [18]	No	1.0 eV
Zhou *et al.* [19]	No	0.5 eV
Zhou *et al.* [19]	Yes, U = 4.3 eV	3.8 eV

great amount of energy stored within it. $LiFePO_4$ is therefore a strong candidate for use as a cathode in Li-ion cells [4–9]. In addition, $LiFePO_4$ is a naturally occurring mineral [10], and is relatively benign to the environment, at least compared to some of the typical Li-ion cell electrodes. However, this material in its pure form is highly resistive to electrical current, and as such the compound has limited practical applicability. Processes that introduce carbon coatings can appreciably improve the conductivity and discharge capacity of the pure sample while maintaining cost-effectiveness [11, 12]. An alternate way to significantly increase the conductivity of $LiFePO_4$ is to introduce either Li- or Fe-site dopants [13–15]; Li-site doping in particular has been reported by Chung *et al.* to increase the conductivity of doped $LiFePO_4$ by a factor of 10^8 [13].

This observed phenomenon in doped $LiFePO_4$ has prompted a flurry of theoretical treatments of the band structure of pure $LiFePO_4$ to understand the electronic structure of the system more completely [3, 16–19]. Although each paper cites results that are unique, the most notable controversy concerns the treatment of electron correlation. Five different authors approach the problem using various band structure theories, although all are based upon *density functional theory* (DFT). Their results show band gaps between 0 and 1 eV. In addition to a typical DFT simulation of $LiFePO_4$ and $FePO_4$, Zhou *et al.* also conduct a study using the more complex DFT + U approach [19]. These calculations predict a band gap of 3.8 eV. Table 1.1 summarizes the relevant results from each of the five authors.

The resolution of this dispute requires experimentation that probes the electronic structure of $LiFePO_4$ and $FePO_4$. However, there has been little effort expended on this goal until now. This thesis presents *x-ray absorption spectroscopy* (XAS) and *resonant inelastic x-ray scattering* (RIXS) spectra taken from $LiFePO_4$ and $FePO_4$, measured using synchrotron radiation. The highly tunable nature of synchrotron radiation allows for an element-specific, site- and momentum-selective probe of the local *partial density of states* (PDOS) of each atom. This sheds new light on the near-Fermi edge density of states and other properties of the electronic structure of $LiFePO_4$.

The thesis is structured as follows. Chapter 2 will detail the physics behind synchrotron radiation. In particular, the storage ring, insertion device, and beamline components will be discussed. Chapter 3 will discuss the experimentation techniques that were used to acquire spectra, notably the three methods commonly used to measure XAS spectra. The technique behind measuring RIXS spectra will also be covered. Chapter 4 will discuss the basics of density functional theory, because DFT calculations were used extensively for the analysis of the spectra from $LiFePO_4$ and $FePO_4$. Chapter 4 will also discuss the specifics of the *orthogonalized linear combination of atomic orbitals* (OLCAO) methodology, as OLCAO was used to calculate the DOS of the two crystals under study. Chapter 5 shows the experimental results. Within Chapter 5 one will also find the analysis whereby the experimental spectra were interpreted and understood within the framework of the simulated DOS. Chapter 6 addresses the issue of which electron correlation functional best describes $LiFePO_4$ and $FePO_4$. Finally, the summary and conclusions are in Chapter 7.

Chapter 2

Synchrotron Sources

The word *synchrotron* is used today to describe a particular type of laboratory which utilizes relativistically moving bunches of electrons to produce radiation at a wide variety of wavelengths. This is accomplished using the well-known result that electrons lose energy by emitting photons when they are decelerated; likewise, absorbing photons will cause the electrons to accelerate. Magnetic fields do not alter the speed of an electron, but do cause a change in the direction component of the velocity, which is sufficient to force the electron to emit a photon.

The discovery of synchrotron radiation was accidental. A synchrotron was built by GE in 1947 to test for phase stability in particle accelerators, and was not meant for explicit use as a radiation source. The capacity of a synchrotron for generating radiation was only discovered when someone looked in an observation window and realized the circling electron beam was glowing [20]. First generation synchrotrons were particle accelerators used for other experiments that were later coupled with apparati that used the radiation emitted by the electrons that caused them to lose energy. However, this has changed markedly in the intervening years, as synchrotron technology has been developed explicitly to provide ever brighter sources of tunable radiation. Modern synchrotrons have diverged much in function from more typical particle accelerators.

Synchrotrons can be divided into two main components. The first component is the storage ring and the magnets therein that accelerate the electrons and thus produce the radiation. There are two general configurations of magnets that are common at modern synchrotrons: *bending magnets* and *insertion devices*. An undulator, a class of insertion device, was used to measure the spectra that will later be presented in Chapters 6 and 7. Therefore, this thesis will be concerned exclusively with insertion devices. The second component is called the *beamline*. After the radiation is produced by the magnetic apparatus in the storage ring, the beamline directs the radiation to the sample under study and records the effects of the radiation on the sample.

2.1 Insertion Devices

Insertion devices are used to produce semi-coherent radiation by accelerating the electron beam. Insertion devices have a periodic lattice of alternating, antiparallel magnetic fields. This allows the electrons to be directed back and forth, accelerating them through many small loops. This is different from a bending magnet, which applies the electrons to one field only. Bending magnets are typically used in modern synchrotrons only when it is necessary to direct the electron beam around a corner. Bending magnets are analogous to the magnetic containment structures used in first generation synchrotrons to hold the electron beam on path. Figure 2.1 shows the differences between bending magnets and insertion devices.

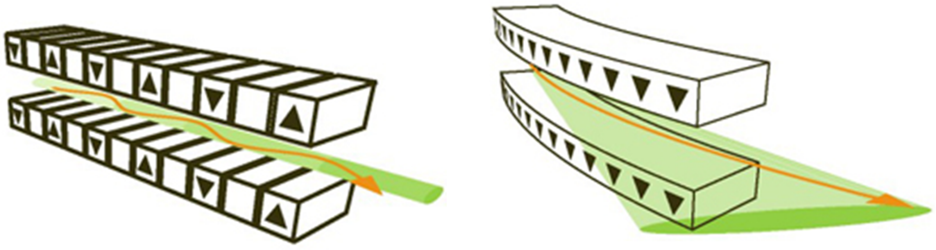

(a) Insertion device

(b) Bending magnet

Figure 2.1: The structure of bending magnets and insertion devices. The material was adapted from Ref. 21.

Insertion devices come in two different varieties: *undulators* and *wigglers*. In form they are quite similar in that both have periodic magnetic structures that oscillate the electron beam, however this is where the similarities end. Undulators are characterized by low-strength magnetic fields with a large number of periods, whereas wigglers have fewer periods and stronger fields. Undulators produce highly coherent light which is tightly confined, both spatially and energetically. Undulator radiation is characterized by bright, sharp peaks at discrete energy levels. Wiggler radiation, however, forms a continuum at high energies. Wigglers produce very intense radiation at energies that undulators typically cannot reach.

2.1.1 Undulators

Undulators produces radiation which has very high spectral brightness in comparison to light that is produced with either bending magnets or wigglers. Spectral brightness is defined as the photon flux per unit area per unit solid angle, within a given spectral bandwidth $\Delta\lambda/\lambda$ or equivalently $\Delta\omega/\omega$, where λ and ω represent wavelength and frequency respectively. Undulators are so bright because the light produced during each oscillation adds constructively. The wavelength of radiation emitted from an undulator is controlled by the *undulator equation*, shown here in Equation 2.1:

$$\lambda_n = \frac{\lambda_u}{2\gamma^2 n}\left(1 + \frac{K^2}{2} + \gamma^2\theta^2\right) \tag{2.1}$$

where λ_u is the 'wavelength' of the periodic magnetic structure of the undulator, and θ is the angle, measured from the axis of propagation, at which the observer detects the emitted radiation. The n in the equation, both the subscript and the value in the denominator, refer to the order of the light, which will be discussed later in this section. The quantity K is the dimensionless magnetic strength parameter defined by:

$$K = \frac{eB_0\lambda_u}{2\pi mc} \tag{2.2}$$

Finally, the γ in Equation 2.1 is the Lorentz factor, and it is defined by:

$$\gamma = \sqrt{1 - \frac{v^2}{c^2}} \tag{2.3}$$

The magnetic field strength parameter K gives a rough line of demarcation between undulators and wigglers. Undulators typically operate in the region around $K = 1$, whereas wigglers often have $K \gg 1$. This is not a hard rule, as what truly differentiates undulators and wigglers is their radiation profiles. K is only one factor that determines how the insertion device radiates, albeit an important factor.

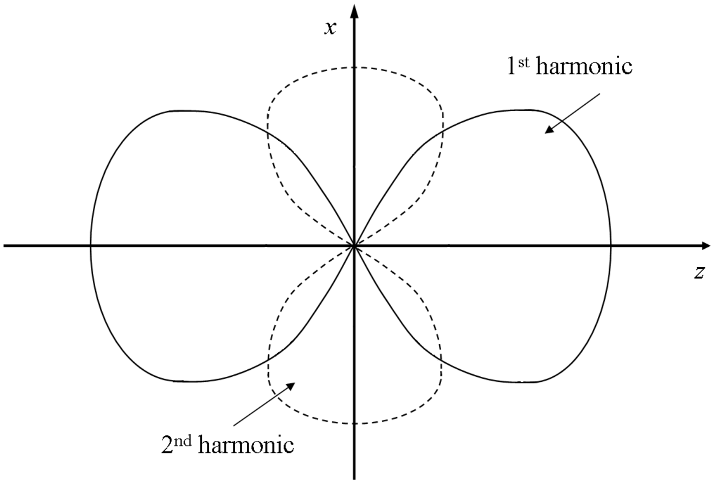

(a) Dipole radiation in the rest frame of the electron. The direction of acceleration is normal to the central axis of the lobes.

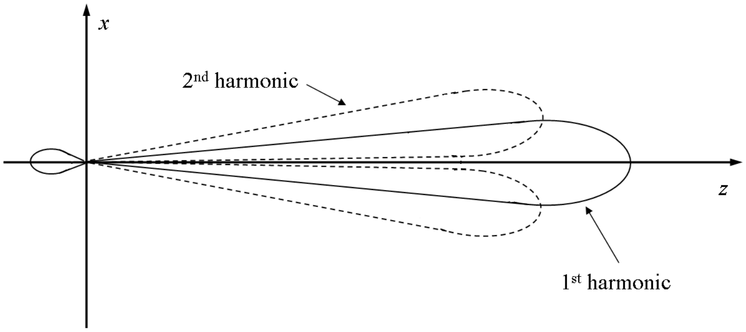

(b) Dipole radiation in the laboratory frame. The lobes have been elongated in the direction of propagation along the positive z-axis.

Figure 2.2: Spatial profiles of dipole radiation in the (a) rest frame and (b) laboratory frame.

The third term in Equation 2.1 deals with the wavelength that an off-axis observer sees. This term varies very strongly with angle; even for a small angular divergence, the wavelength increases considerably, owing to the fact that γ for highly relativistic electrons is several thousand. This third term shows the “searchlight” effect of synchrotron radiation. If one approximates the electron as an electric dipole accelerating in a plane perpendicular to the axis of propagation, then the classical double lobes of dipole radiation as seen in the rest frame of the electron are elongated into the searchlight effect as seen in the laboratory frame. This is shown by the transformation of the lobe labeled '1st harmonic' from the rest frame to the laboratory frame in Figure 2.2. The lobe labeled '2nd harmonic' in Figure 2.2 arises from an on-axis acceleration component, the origin of which will be discussed in greater detail later in the section. The searchlight effect is due to the relativistic speed of the electrons, and so all magnetic configurations cause the electrons to radiate in a similar cone-shaped structure. The details of the magnetic structure simply effect the width of the cone, and in the case of undulators, the cone is very tightly confined.

The second term in Equation 2.1 involves the dimensionless magnetic field strength parameter K. This term accounts for the fact that the magnetic fields reduce the electrons' effective propagation velocity because the electrons are forced to take a longer path as they oscillate through the insertion device. This is a necessary correction because the γ in the denominator, as well as in the third term of the numerator in Equation 2.1, assume that propagation velocity is constant everywhere in the storage ring, including through the undulator itself.

This second term is the reason for one the most vaunted characteristics of a synchrotron: tunability. Synchrotrons differ from other radiation sources because they produce high intensity radiation over a wide energy range. Given the form of the undulator equation, there are two variable quantities that one could use to adjust the energy of the photons produced by the undulator: K and γ. Adjusting γ would involve changing the energy of the electrons in the entire storage ring, which would affect all beamlines, and of course would be difficult to accomplish. Changing K involves only a local adjustment, and does not (in principle) affect other beamlines. K is usually adjusted by changing the gap between the magnetic plates on either side of the beam, called the *undulator gap*. Although Equation 2.2 is not explicitly a function of the undulator gap, the quantity B_0 is nevertheless dependant upon this quantity. A larger gap will decrease the strength of the magnetic field.

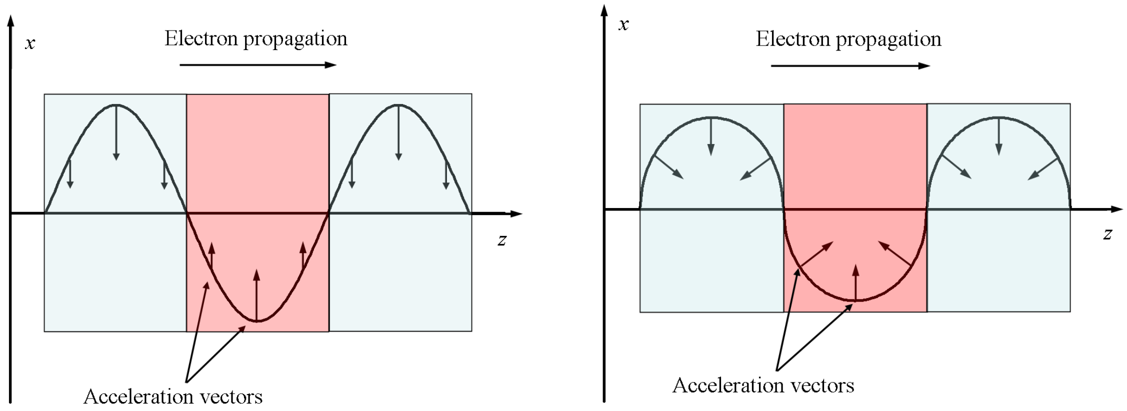

(a) The sinusoidal path of an electron as it propagates through the undulator. All acceleration vectors are perpendicular to the axis of propagation (z-axis), thus ensuring that the radiated photons are parallel to the z-axis.

(b) The simplified path of an electron as it passes through the undulator. The acceleration vectors are perpendicular to the path of the electron, giving an acceleration component parallel to the axis of propagation.

Figure 2.3: Propagation paths of an electron as it passes through an undulator. In each figure, the different colors of the colored boxes represent antiparallel magnetic fields. The left figure shows the idealized version, whereas the right figure shows a simplified view of what would actually happen to an electron passing through zones of uniform, antiparallel magnetic fields.

The undulator equation describes the wavelength of the radiation produced by an undulator with great accuracy, but it is fundamentally flawed. This flaw is in the assumption that the velocity of the electron in the plane perpendicular to the direction of propagation is a sinusoidal waveform. This assumption visualizes the electron as a simple harmonic oscillator which is oscillating back and forth across the axis of propagation, thus tracing out a sinusoidal pattern as the electron propagates through space. Although mathematically convenient, this assumption is incorrect. An electron traveling at a constant speed does not follow a sinusoidal path in a uniform magnetic field, it follows a circular path. Figure 2.3 shows the how the paths differ between the two possibilities.

The important difference is the behavior of the acceleration vectors. As seen in Figure 2.3(b), there is a component of the centripetal acceleration that lies parallel to the direction of propagation. This means that the z-component of the velocity of the electrons is not constant, and produces radiation perpendicular to the z-axis. Figure 2.2 shows the symmetric lobes of radiation labeled as '2nd harmonic' in the rest frame of the electrons. These lobes transform into the laboratory frame to produce off-axis radiation fields.

In general, all of the even-order harmonics are off-axis, with all odd orders being on-axis. The frequencies of these harmonics are integer multiples of the fundamental frequency. This is the reason for the n in the undulator equation. Higher orders have smaller wavelengths, and thus higher energies. The higher orders also have narrower bandwidths. The central radiation cone, wherein half of the power is concentrated, is defined in Equation 2.4 as follows:

$$\theta_{cen} = \frac{\sqrt{1 + \frac{K^2}{2}}}{\gamma\sqrt{nN}} \tag{2.4}$$

where n is the harmonic and N is the number of magnetic periods within the undulator. This is what is known as the *undulator condition*. Within this central cone, the spectral width of the radiation is calculated as follows:

$$\left(\frac{\Delta\lambda}{\lambda}\right)_n = \frac{1}{nN} \tag{2.5}$$

Equations 2.4 and 2.5 reflect the fact that the higher orders effectively "see" more periods within the undulator. The greater number of periods allow for greater coherence of the light, because the photons produced at each period will interfere with the photons produced at every other period. This will do more to reinforce the on-axis radiation and eliminate the off-axis radiation, tightening the radiation cone spatially and spectrally.

Higher harmonics seem to be a useful part of synchrotron radiation, as they have narrower spectral width. However, higher harmonics suffer from reduced intensity. In principle, all even-ordered harmonics should have zero intensity at the sample, given that they are off-axis and thus cannot pass the aperture stop at the entrance to the beamline. The analytical equation for the on-axis intensity of an odd-order harmonic is given in the following formula [22]:

$$I = \alpha N^2 \gamma^2 \frac{\Delta\omega}{\omega} \frac{I_b}{e} F_n(K) \tag{2.6}$$

where I_b is the beam current, e is the charge on an electron, and α is a structure factor. The $F_n(K)$ term is necessary because it describes how the intensity of the fundamental changes as the magnetic field becomes stronger. It is given by the following equation.

$$F_n(K) = \frac{K^2 n^2}{\left(1+\frac{K^2}{2}\right)^2} \left\{ J_{\frac{n-1}{2}} \left[\frac{nK^2}{4\left(1+\frac{K^2}{2}\right)} \right] - J_{\frac{n+1}{2}} \left[\frac{nK^2}{4\left(1+\frac{K^2}{2}\right)} \right] \right\}^2 \tag{2.7}$$

Figure 2.4 shows the behavior of $F_n(K)$ as a function of order n and magnetic strength K.

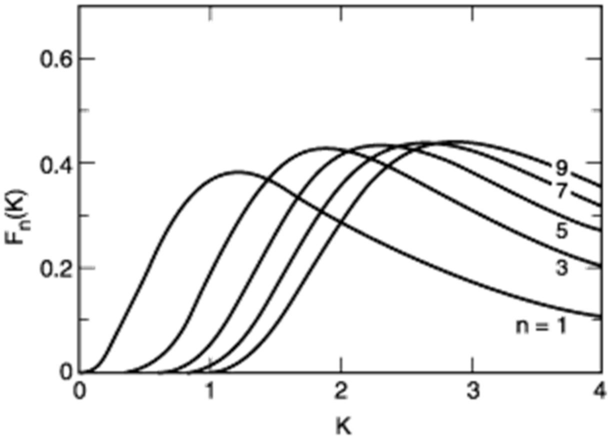

Figure 2.4: Behavior of $F_n(K)$ as a function of n and K. This graph was adapted from Ref. 22

For K values typical of undulators, the radiated photon intensity of the fundamental ($n = 1$) harmonic is clearly superior to all other orders. The higher odd harmonics do have superior spectral width, however using them to excite a sample is simply not feasible because the flux is insufficient. At higher values of K, Figure 2.4

shows that the higher orders approach and then surpass the fundamental harmonic in intensity. This trend will become important later in the discussion of wigglers.

Up until this point, it has been implicitly assumed that the electron beam has been ideal, with no spatial or angular divergences to affect the results. In reality, random motions will cause the electrons to move at an angle α with respect to the z-axis. This results in a longer path length for these electrons that do not remain near to the z-axis, and the photons radiated by these off-axis electrons are Doppler shifted to lower energies. This shift is given by:

$$\frac{\Delta E}{E} = \gamma^{*2}\alpha^2 \tag{2.8}$$

where α is the beam divergence angle. In order for the radiation profile to maintain its analytical undulator sharpness, then $\alpha^2 \ll \theta_{cen}^2$, where θ_{cen} is defined as the angle containing the central cone region, as before. In a real synchrotron facility, the beam divergence can be on the order of the central cone, and so this must be taken into account. If one assumes that the electron divergence profile to be Gaussian in shape, then one can add in quadrature the width of the ideal cone and the beam divergence. This gives the total angular radiation cone width as follows:

$$\theta_{Tx} = \sqrt{\theta_{cen}^2 + \sigma_x'^2} \tag{2.9}$$

$$\theta_{Ty} = \sqrt{\theta_{cen}^2 + \sigma_y'^2} \tag{2.10}$$

where $\sigma_y'^2$ and $\sigma_x'^2$ are the divergences in the yz-plane and the xz-plane, respectively.

Real synchrotrons are characterized by two parameters, the phase space volume of the electron beam, or *emittance* ϵ, and β, a parameter which characterizes the magnetic lattice which contains the beam. The emittance in particular is very important, because it cannot be adjusted during normal operation. Many factors that effect the emittance are tied to critical components, such as those that produce and accelerate the electrons for the storage ring, which cannot be changed without significantly retooling the facility. The parameters ϵ and β are important because they determine the spatial and angular distributions of the electron beam. These distributions are represented by $\sigma_{x,y}$, which describes the spatial deviation, and $\sigma'_{x,y}$, which describes the angular deviation. The formulae for $\sigma_{x,y}$ and $\sigma'_{x,y}$ as functions of ϵ and β are shown below:

$$\sigma_{x,y} = \sqrt{\epsilon_{x,y}\beta_{x,y}}, \tag{2.11}$$

$$\sigma'_{x,y} = \sqrt{\frac{\epsilon_{x,y}}{\beta_{x,y}}} \tag{2.12}$$

As can be seen from these formulae, it is not possible to have a perfectly divergenceless electron beam. The spatial and angular deviations are interrelated, so the characteristics of the electron beam must be optimized for the type of experiment being conducted. This is because the phase space volume of the emitted photons is dependant upon the emittance of the electron beam.

2.1.2 Wigglers

As stated earlier, the main differences between wigglers and undulators is the dimensionless magnetic strength parameter K. This value is typically in the vicinity of 1 for undulators, while for wigglers $K \gg 1$. Wigglers also have fewer periods in their magnetic structures than undulators, and the electrons travel farther afield. It would seem at first glance that wigglers and undulators are simply the same device with different parameters, and that the equations from the previous section should apply only with high values of K to represent the stronger magnetic fields characteristic of wigglers. However, many of the assumptions used in deriving those equations do not hold in the strong-field limit. Consequently, wiggler and undulator radiation profiles look nothing alike. Figure 2.5 below displays a qualitative look at the different spatial and angular profiles from the two insertion devices.

The analytical formulas derived for undulators do not hold for wigglers, because the radiation that is produced is no longer coherent. The photons radiated at each period do not interfere with each other, either constructively or destructively. The intensities, not the radiation fields, produced by the accelerating electrons add together. Mathematically, this means that one calculates a sum of squares, rather than

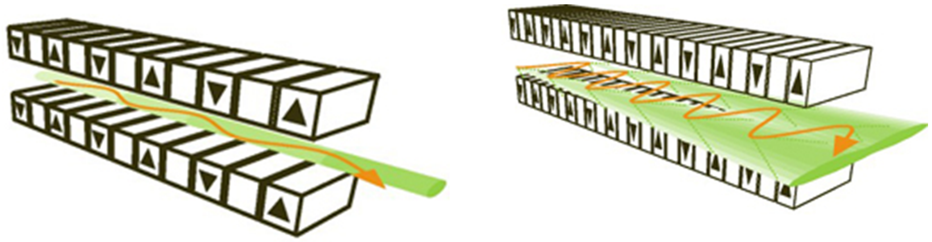

(a) Undulator (b) Wiggler

Figure 2.5: Typical spatial profiles of the radiation fields emitted from undulators and wigglers. This figure was adapted from the material found in Ref. 21.

the square of a sum. It is not surprising then that the photon flux of a wiggler, as a function of energy, looks strikingly similar to that of a bending magnet of similar K. The spectrum of the wiggler, however, is shifted to higher energies. The spectrum produced by a wiggler also benefits from a $2N$ increase in intensity, owing to $2N$ more bends that the wiggler has compared to the bending magnet.

The undulator equations may not hold explicitly, but they nevertheless give an idea of what to expect from a wiggler. Based on these formulae, one can make the following statements about the radiation pattern emitted from a wiggler:

1. The photon beam has a broader sweep zone because the electrons travel farther from the axis of propagation in the stronger magnetic field. The sweep zone is the area that the photon beam covers as it moves back and forth, a result of the searchlight effect of synchrotron radiation. The broader sweep of a wiggler allows more off-axis photons, including even-order harmonics, to be seen by the observer (beamline).

2. The angular and spatial confinement of the electron beam is lessened with wigglers. Equation 2.4 shows that high values of K and a small number of magnetic periods N both work to increase the physical size of the radiation field. This lessened confinement of the beam ultimately results in poorer energy resolution of the photon beam. Random, off-axis motions of the electrons serve to spread the energy of a given harmonic.

3. In accordance with Equation 2.4, large values of K significantly reduce the amount of power radiated though the fundamental harmonic. This power is then divided among the higher harmonics.

The third point in particular is of special importance, because this property allows wigglers to radiate significant photon flux at energies far above those that can be reached by undulators. This is because the higher harmonics radiate at frequencies that are integer multiples of the fundamental frequency, which corresponds to an integer multiple of the energy of the fundamental harmonic.

An important value to consider is that of the critical harmonic, n_c. The critical harmonic divides the intensity in two; all the harmonics below this value radiate half of the total power emitted by the wiggler, and the harmonics above it radiate the other half. The critical harmonic is calculated as follows:

$$n_c = \frac{3K}{4}\left(1 + \frac{K^2}{2}\right) \tag{2.13}$$

For undulators, the value of n_c is very small. An undulator with $K = 1$, for example, has an n_c of 9/8. This confirms the anticipated result that the fundamental harmonic carries most of the intensity. However, with the 19 period, 2.13 Tesla wiggler at the ALS, $n_c \approx 12000$. Half of the intensity of this wiggler is radiated by harmonics over 12000, which of course means that half of the radiation intensity is emitted by photons with over 12000 times more energy than the fundamental harmonic.

Wigglers and undulators are very different from one another, but one is not superior to the other. One insertion device will simply be superior to another for a given application. Undulators certainly are preferable for energy resolution and flux, which is important for the soft x-ray regime that undulators can easily reach. However, if one wants to generate very hard x-rays, then one must use a wiggler. An undulator simply cannot generate enough flux at the necessary, very high photon energies.

The information in this section on insertion devices is based primarily on the material presented in Attwood's book [23].

2.2 The Beamline

The term *beamline* is used to describe the collective instrumentation that makes use of the radiation produced by the insertion device or bending magnet within the storage ring. The beamline has two separate sections. The first section is called the *monochromator*. The purpose of the monochromator is to filter the fan of radiation produced in the storage ring so that only the desired energy band passes through to the sample. The second component is called the *endstation*. The endstation consists of all of the instrumentation used to sense how the sample reacts to the light passed by the monochromator. There are many other optical elements in a beamline that can affect the energy bandwidth and size of the photon beam, such as the mirrors necessary for proper alignment. However, these components will not be discussed in this thesis.

There are many different designs that are possible for a beamline, depending on what kind of experiment that will be conducted. There are many different parameters that characterize the performance of a beamline, not the least of which being flux throughput (efficiency), energy resolution, spatial and angular resolution, and the achievable energy range. Not surprisingly, optimizing all of these parameters independently is not possible, and design compromises are inevitable. Given the myriad possibilities for successful beamline design, this thesis will focus on discussing the particulars of Beamline 8.0.1 at the Advanced Light Source in Berkeley, CA. This beamline was used nearly exclusively to measure the data presented in Chapters 6 and 7. A diagram of this beamline is shown in Figure 2.6. Beamline 8.0.1 actually has two endstations, namely the SXF (soft x-ray fluorescence) and EMA (ellipsoidal mirror electron energy analyzer) endstations. The spectra presented in this thesis were measured with the SXF endstation.

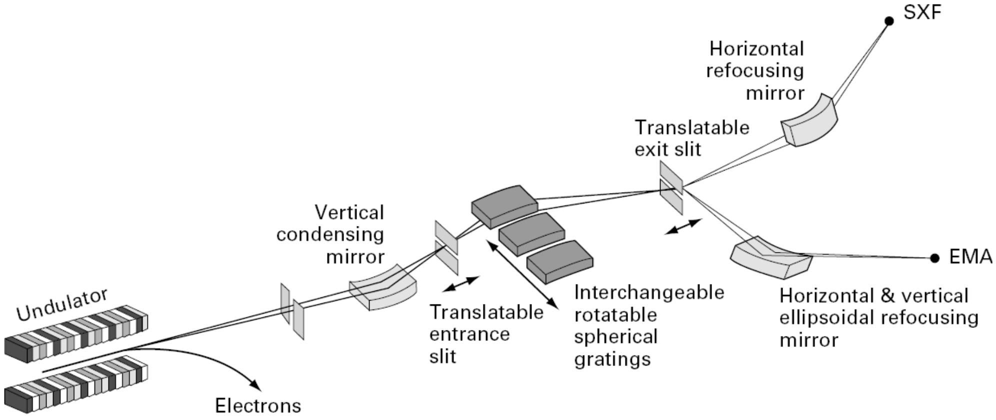

Figure 2.6: Conceptual schematic of Beamline 8.0.1 at the Advanced Light Source. This facility is part of the Lawrence Berkeley National Laboratory operated by the University of California, Berkeley in Berkeley, CA. Beamline 8.0.1 has a 5 cm period undulator. Depending on the harmonic and the energy to which the undulator is tuned, the undulator gap is typically between 10 and 25 μm. This schematic was adapted from the material presented in Ref. 24.

2.2.1 The Monochromator

The monochromator at Beamline 8.0.1 consists of three optical components: the entrance slit, the grating, and the exit slit. Together, these components act as a narrow band pass filter that reduces the spot size and energy bandwidth of the photon beam. Note that this is equivalent to reducing the phase space volume of the photon beam. As stated earlier, the phase space volume of the photon beam is dependant upon the emittance of the electron beam. The latter is a constant value because the storage ring is designed to be a near-lossless system. The phase space volume of the photon beam can therefore be reduced by introducing losses in the beamline, i.e. throwing away flux. Thus, the monochromator increases energy resolution and reduces spot size at the cost of flux. Modern synchrotrons, however, produce many more photons than is strictly necessary for common experimentation techniques, such as the ones that will be discussed later in the Experimentation Techniques section. The loss of flux is therefore not detrimental. In addition to the tunability of synchrotron radiation, the high photon flux rate is a second unique property of synchrotrons that sets them apart from, and often above, other photon-based experimentation facilities for studying condensed matter.

One of the main functions of the monochromator is to demagnify the source. Demagnification of the beam, which allows for a small spot size on the sample, is an important attribute for any beamline. The degree by which the source need be demagnified depends upon the nature of the experiment. Spectromicroscopy experiments, for example, measure photon absorption and/or emission as a function of the beam's spatial coordinates on the sample. This type of experiment obviously requires excellent spatial resolution of the beam. Other experiments also benefit from a small spot size, as it may become necessary to measure spectra from a tiny single crystal that can not be spread out to an arbitrary size like powdered samples.

The entrance slit is necessary for two major functions. Firstly, it demagnifies the source. Secondly, the entrance slit improves energy resolution by acting as an aperture stop. Beamline 8.0.1 uses an undulator, and as shown in the Undulators section above, the wavelength of the emitted light strongly depends upon the off-axis observation angle. The entrance slit stops much of the off-axis radiation from getting to the sample; a smaller slit means a tighter energy bandwidth. On the other hand, closing the slits will also limit the flux.

The on-axis radiation that passes through the slit will exhibit a typical single-slit Fraunhofer diffraction pattern. The off-axis radiation that passes through the slit will also experience diffraction, but the effect of the more complicated geometry on the diffraction pattern is beyond the scope of this thesis. A Fraunhofer diffraction pattern from a single slit is displayed below in Figure 2.7.

A Fraunhofer diffraction pattern for the on-axis radiation is described by $(\sin\beta/\beta)^2$, where $\beta = \pi Dx/\lambda R$. The definitions for x and R are displayed in Figure 2.7, and D is the width of the slit. As R is increased, β is decreased, which means that at a fixed point x below the axis, the radiated power increases with distance from the

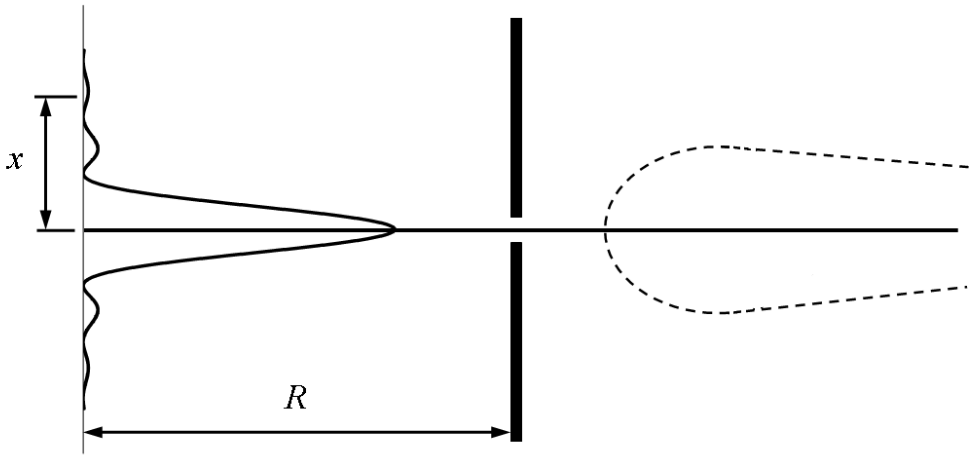

Figure 2.7: The Fraunhofer diffraction pattern expected for the on-axis radiation. On the right of the figure is the undulator radiation cone impinging upon the slit. Most of the radiation will not be passed by the slit. Any off-axis radiation that makes it through the slit will also be diffracted, but the resulting pattern is not shown in this figure.

slit. The diffraction pattern will therefore spread out the farther one measures the diffracted spectrum from the slit.

The next item is the grating. The grating can come in a variety of shapes, including planar, toroidal, and special cases of toroidal geometry, such as spherical and cylindrical. They each have their benefits and detriments, however the spherical shape is a popular choice because it is accurately manufactured and provides good resolution. Spherical gratings cannot perform sagittal focusing (unlike toroidal gratings), and they cannot demagnify the source (unlike planar gratings). Other optical elements, such as mirrors and slits, are necessary to fulfill these requirements if one wishes to use a spherical grating. The monochromator at Beamline 8.0.1 uses a grating with spherical geometry.

The grating is the part of the monochromator that is most directly responsible for narrowing the bandwidth of the radiation. The optical path function for a spherical grating, which is partially given in Equation 2.14, describes how light is focused when it interacts with the grating. The function is based on Fermat's principle, which states that the path taken by a ray of light is minimized. In general, the optical path function is an expansion with many terms that describe how effectively the grating focuses the light. Each of the terms describes a different element of the focused image. As an example, sagittal focus (focus in the plane parallel to the surface of the grating) and meridional focus (focus in the plane on which the optical components lay) are described by two separate terms in the optical path function, namely the F_{020} and F_{200} terms. All of the terms in the optical path function must equal zero for the image to be perfectly focused. If any term is not zero, the generated image has an aberration that is unique for that particular term. Equation 2.14 has six different terms; Equation 2.14a is the grating equation, Equation 2.14b is the sagittal focus, Equation 2.14c is the meridional focus, Equation 2.14d is the primary coma, Equation 2.14e is the spherical abberation, and lastly Equation 2.14f is the astigmatic coma. These terms are given below:

$$\begin{aligned}
F_{100} &= Nk\lambda - (\sin i + \sin i') && \text{(2.14a)}\\
F_{020} &= \frac{1}{r} + \frac{1}{r'} - \frac{1}{R}(\cos i + \cos i') && \text{(2.14b)}\\
F_{200} &= \left(\frac{\cos^2 i}{r} - \frac{\cos i}{R}\right) + \left(\frac{\cos^2 i'}{r'} - \frac{\cos i'}{R}\right) && \text{(2.14c)}\\
F_{300} &= \left(\frac{\cos^2 i}{r} - \frac{\cos i}{R}\right)\frac{\sin i}{r} + \left(\frac{\cos^2 i'}{r'} - \frac{\cos i'}{R}\right)\frac{\sin i'}{r'} && \text{(2.14d)}\\
F_{400} &= \frac{4}{r^2}\left(\frac{\cos^2 i}{r} - \frac{\cos i}{R}\right)\sin^2 i - \frac{1}{r}\left(\frac{\cos^2 i}{r} - \frac{\cos i}{R}\right)^2 && \text{(2.14e)}\\
&\quad + \frac{4}{r'^2}\left(\frac{\cos^2 i'}{r'} - \frac{\cos i'}{R}\right)\sin^2 i' - \frac{1}{r'}\left(\frac{\cos^2 i'}{r'} - \frac{\cos i'}{R}\right)^2 \\
&\quad - \frac{1}{R^3}(\cos i + \cos i') + \frac{1}{R^2}\left(\frac{1}{r} + \frac{1}{r'}\right) \\
F_{120} &= \left(\frac{1}{r} - \frac{\cos i}{R}\right)\frac{\sin i}{r} + \left(\frac{1}{r'} - \frac{\cos i'}{R}\right)\frac{\sin i'}{r'} && \text{(2.14f)}
\end{aligned}$$

where i and i' are the angles of incidence and diffraction, respectively. The value r is the distance from the source to the grating, and r' is the distance from the grating to the observer. In the case of the monochromator design utilized at Beamline 8.0.1, the ‘source’ is the entrance slit, and the ‘observer’ is the exit slit. The quantity R is the radius of curvature for a spherical grating. The list is arranged such that the

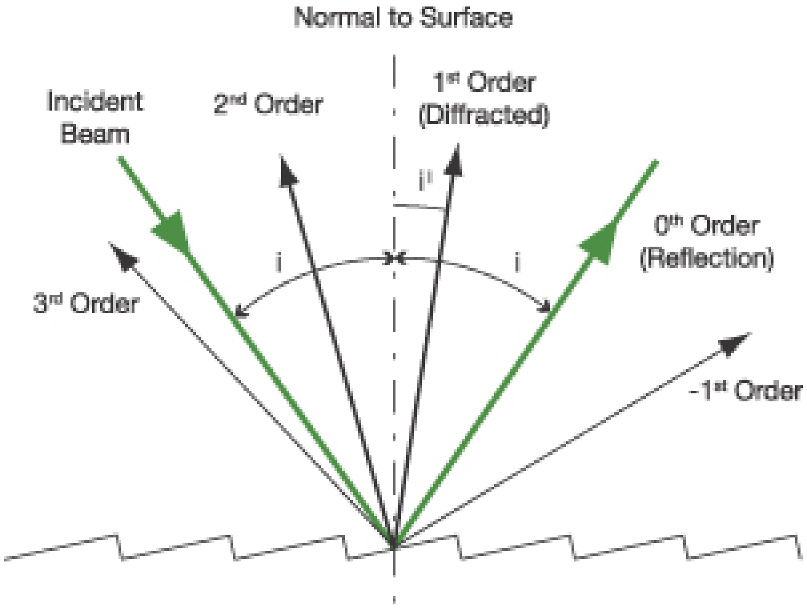

Figure 2.8: Diffraction from a grating, adapted from Ref. 25.

order of the terms increases as one reads down the list. Higher order terms have less impact, thus the most important term is F_{100} (Equation 2.14a). This is the so-called grating equation. In the grating equation, N is the groove density, k is the order, and λ is the wavelength of light. This term must be set to zero, as must all terms in the optical path function expansion for the grating to focus the light properly.

The grating equation resembles the Bragg equation for diffraction from planes within a crystal because the Bragg equation and the grating equation work on the same principle. Light reflected from a plane within a crystal, or alternatively light reflected from a groove on the surface of a grating, interferes with light reflected from other similar planes/grooves. This leads to maximal intensity zones where the light constructively interferes, separated by intensity minima. The angular separation between these maxima is determined by the number of scattering sites, which in the case of gratings, is represented by the number of grooves per unit distance N along the grating. Figure 2.8 gives an example of diffraction from a grating for one wavelength.

Figure 2.8 shows diffraction from a grating for one wavelength only, and each of the rays representing diffracted light represents a different value of the order k. Note that this is the diffraction order, and should not be confused with the orders of harmonics discussed earlier with respect to insertion devices. The diffraction angle i' depends upon wavelength as well as order, so that for a particular order the radiation incident upon the grating is split into a wide angular fan according to wavelength. If one aligns the optics according to a particular diffraction angle, the unwanted wavelengths of light will focus off-axis. The exit slit, which functions in much the same fashion as the entrance slit, absorbs the off-axis radiation and allows only the desired bandwidth to pass. As with the entrance slit, a smaller slit width will eliminate a larger section of the radiation fan that is diffracted from the grating. In doing so, however, the flux impinging on the sample is limited. Note that the fan effect only applies to the first order and higher. In the case of the zeroth order, the first term in the grating equation is 0 for all wavelengths. This is simply light reflected off the plane of the grating with no angular dependance on wavelength.

The differing angles of diffraction for wavelengths scattered from the grating introduces an interesting problem into beamline design. The dependance of diffraction angle on wavelength means that the focal length is also dependant on wavelength. With this problem in mind, the exit slit for the monochromator at Beamline 8.0.1 was built to move along the optical path, thus changing its separation distance from the grating to coincide with new focal lengths. Without this function, the exit slit may be too close or too far from the grating, depending on the desired photon energy. In addition to the movable exit slit, the grating can be rotated. These functions increase the energy range that the monochromator can reach and still have it bring a respectable flux rate to bear upon the sample. Although this design increases the energy window that the beamline can access, it nevertheless can in principle skew energy calibration if the exit slit of the monochromator is not placed in precisely the correct spot to allow through photons with the desired energy. This problem is correctable, provided that the energy calibration error does not change noticeably over an excitation threshold. If the energy calibration error is constant, then the spectrum can simply be shifted to the appropriate energy. This shift is calculated by comparing the spectrum of a commonly measured standard sample to its accepted spectrum presented in literature. Of course, the spectrum of this standard sample must be measured with the same set of parameters as the sample(s) under investigation, and its spectrum must be within the same energy range.

Figure 2.8 shows a wide angular separation between the orders of radiation that are diffracted from the grating. This is done to make the figure readable and instructive, but it is misleading because such large angles with respect to the surface of the grating are not possible in soft x-ray optics. All soft x-ray optical systems require the optics to aligned using grazing angles of incidence. This constraint is necessary simply because soft x-rays interact very strongly with matter, so grazing incidence is required to maximize the reflected portion of the radiation. This high level of interaction with matter is also the reason why soft x-ray beamlines require the optical path to be in ultra high vacuum (UHV).

2.2.2 The Endstation

The endstation is the term used to describe the systems necessary to hold the sample and keep it in UHV, as well as all of the instrumentation that is necessary to document how the sample reacts to the radiation that has been focused upon it. This part of a beamline is by far the most variable component, as there are several different ways that matter can react to radiation, and for each of these radiation-matter interactions there can be many experiments that can record the event, each in a different way. Thus, the configuration of, and the instrumentation used with, an endstation can vary substantially among beamlines, even beamlines that operate within the same energy range. As with the discussion of monochromators above, the topic of endstations will be concerned largely with Beamline 8.0.1; specifically, the Soft X-ray Fluorescence (SXF) endstation. However, the SXF endstation is not entirely unique, and variations of the instruments found therein can be found on other endstations.

There are many components to the endstation, such as the mechanisms that allow one to transfer samples into the measurement chamber. The present discussion will be limited to those components necessary to measure XAS and RIXS spectra. These components are a highly transparent gold mesh, the sample plate, the spectrometer, and a Channeltron detector. The first three will be discussed later in this section on endstation design. The function and application of the Channeltron, however, is discussed in detail in the Total Fluorescence Yield section of Chapter 3. Suffice is to say here that the Channeltron is used to measure a large portion of the total number of photons that are emitted from a sample when it is excited at a particular energy.

The second component to be discussed, the gold mesh, comes before the sample, in the sense that the beam passes the mesh before reaching the sample. It does not measure how the sample reacts to the incoming radiation per se, but it is nevertheless necessary for a proper analysis of any measured XAS spectrum. The purpose of the gold mesh is to measure the intensity of the incoming beam before it hits the sample. The gold mesh is connected to ground through a picoammeter. The picoammeter measures the amount of current that is flowing into the mesh from ground as electrons are removed because of interaction with the radiation beam. The physics that dictate how the electrons are removed from the mesh is discussed in the Total Electron Yield section in Chapter 3. The current that is flowing into the mesh increases with the intensity of the beam, simply because more electrons are removed. Thus, the mesh current shows the intensity of the radiation that the sample is receiving at that energy and bandwidth, relative to other energies. Ideally, the mesh itself is a material that has a constant probability to absorb the photons across the energy range of interest, so that the experimentalist knows the intensity of radiation explicitly without needing to be concerned with the details of how the mesh is interacting with the radiation.

Gold is a popular choice for mesh materials because it does not react strongly with any other element, including oxygen. Thus, a pure gold mesh stays relatively pure, making it highly effective because there are only the various gold resonant absorption edges to cause concern. Over time, elements such as carbon will build up on the gold mesh despite the relative chemical inertness of gold. This problem can be overcome by evaporating more gold onto the mesh, covering the contaminants. This can be done *in situ*, which minimizes contamination because the beamline does not have to be vented to replace the mesh. Also, gold is a good conductor, facilitating the replacement of electrons that have been removed.

The mesh current is important information when performing a measurement that requires scanning across an energy range. At each photon energy, the flux that is reaching the sample is measured, and a spectrum is recorded of the mesh current as a function of photon energy. This is necessary to record because the beamline itself interacts with the beam, absorbing more photons at certain energies if they happen to correspond to the energies of resonant absorption edges of materials found within the beamline. These materials may be put there deliberately, such as the SiO_2 that is commonly used to make mirrors. However, the beamline may also have some contamination. This contamination may be from gases in the non-ideal vacuum in the beamline, but contaminant solids may also have reacted with the reflective/diffactive surfaces within the beamline. Regardless of the source, the effects of the contaminants must be removed because they superimpose structure on the spectrum that is measured from the sample.

If there is a material in the beamline that absorbs photons preferentially at a certain energy, then a drop in the mesh current will be observed at that energy. This structure is removed simply by dividing the spectrum of the sample by the mesh current, called *normalization*. The normalized spectrum will therefore display only the spectral structure of the sample over the energy range in question, with no contribution from the beamline. Normalizing the absorption spectrum to the mesh current also removes any fluctuations in the intensity due to the storage ring. To summarize, normalizing the absorption spectrum to the mesh current makes the spectrum independent of the spectral curves of all materials preceding the sample.

The next component is the sample holder. Other than performing the necessary and obvious job of holding the sample in the path of the beam, the sample holder is also grounded through a picoammeter. This allows one to measure the rate at which electrons are being replaced in the sample. This is much the same as the system set up to measure the mesh current. The details of this experimentation technique are discussed in the Total Electron Yield section of Chapter 3.

The last component to be discussed on the endstation of Beamline 8.0.1 is the spectrometer. When radiation interacts with matter, that radiation may transfer energy to the matter. The substance may then de-excite by releasing a photon to carry away the excess stored energy. This is called a *photon-in photon-out* process, and the purpose of the spectrometer is to detect and analyze the outgoing photons. The Channeltron does this as well, however the Channeltron measures the photon count rate as a function of excitation energy, whereas the spectrometer measures the emitted photons as a function of emission energy. The spectrometer consists of three components: an entrance slit, a grating, and a photon detector. As before in the monochromator design, narrowing the slit will increase energy resolution but will decrease the flux illuminating the grating and ultimately the photon detector. The photons that are emitted from the sample and pass through the entrance slit shine on the grating, which splits the different wavelengths. It functions in this way much like the monochromator, however the spectrometer has a much different purpose. The various wavelengths of light emitted by the sample, separated by the grating, are then focussed onto an area sensitive photon counter, such as a charge coupled device (CCD) or a multi-channel plate (MCP). The spectrometer on Beamline 8.0.1 uses an MCP. The photon detector must be area sensitive because the wavelengths of light will focus onto different parts of the sensor. The range of energies which the sensor may detect, called the *energy window*, is therefore determined largely by the size of the detector and the angular separation between different wavelengths produced by the grating. As a rule, however, photons with longer wavelengths (smaller energy) have greater angular separation than photons with shorter wavelengths (higher energy). Thus, the window for low energy photons is smaller, but in exchange the resolution is better for low energy photons because it is easier to spatially differentiate between wavelengths.

The spectrometer on the SXF endstation of Beamline 8.0.1 is designed according to Rowland circle geometry. Rowland circle geometry is the result of a theoretical analysis performed by H. A. Rowland before the optical path function had been derived from Fermat's principle. His goal was to minimize the aberrations incurred when using a spherical grating [26]. The grouping of the terms in Equation 2.14

allows one to easily see that there are parts common to Equations 2.14c, 2.14d, and 2.14e. The terms common to all three equations are as follows:

$$\left(\frac{\cos^2 i}{r} - \frac{\cos i}{R}\right) \quad \text{and} \quad \left(\frac{\cos^2 i'}{r'} - \frac{\cos i'}{R}\right) \tag{2.15}$$

If one sets these two terms to zero and solves for r and r', then the solution is:

$$r = R\cos i \quad \text{and} \quad r' = R\cos i' \tag{2.16}$$

These are called the Rowland conditions. The conditions require that the source and target (the entrance slit and MCP, respectively) lie upon a circle of radius R, called the *Rowland circle.* In addition, the spherical grating must have a radius of curvature of $2R$. If these conditions are met, then the first five terms of the optical path function reduce to the following equations:

$$F_{100} = Nk\lambda - (\sin i + \sin i') \tag{2.17a}$$

$$F_{020} = \frac{1}{r} + \frac{1}{r'} - \frac{1}{R}(\cos i + \cos i') \tag{2.17b}$$

$$F_{200} = 0 \tag{2.17c}$$

$$F_{300} = 0 \tag{2.17d}$$

$$F_{400} = -\frac{1}{R^3}(\cos i + \cos i') + \frac{1}{R^2}\left(\frac{1}{r} + \frac{1}{r'}\right) \tag{2.17e}$$

Thus, simply by keeping the source, grating, and sensor on the Rowland circle, the F_{200} and F_{300} terms are made identically 0, and the fifth term, F_{400}, is significantly reduced. Provided that one can design a spectrometer with Rowland circle geometry that can also accommodate grazing angles of incidence, then the product is a spectrometer that is affected little by the most influential aberrations. Care must still be taken to properly focus the image in the sagittal plane, which is the focal element controlled by Equation 2.17b. Figure 2.9 below gives a visual representation of a spectrometer that is built using Rowland circle geometry.

The high brilliance of synchrotron sources is of paramount importance when using a spectrometer to record photon-in photon-out processes. Before the photon beam even reaches the sample, it must pass over two or more mirrors, as well as

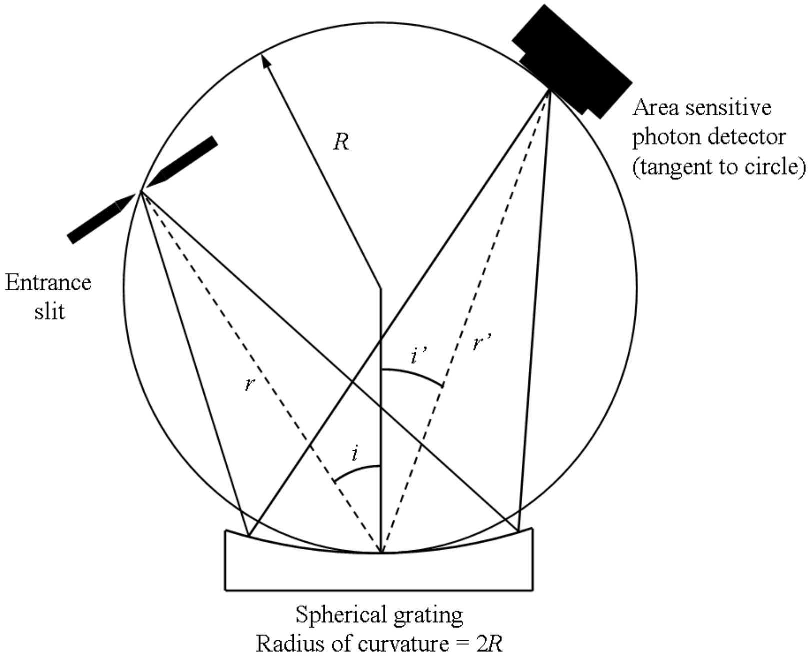

Figure 2.9: A spectrometer design that adheres to Rowland circle geometry. The entrance slit and photon sensor must remain on the circle, although they are free to move anywhere along it.

pass through two slits and at least one grating. Each of these components, the slits especially, throw away photons. When it hits the sample, the flux of the photon beam is a small fraction of what the insertion device produced. The sample, now excited, must have its excited atoms decay and produce photons. As will be discussed later, however, the probability that the sample will shed energy by radiative decay is quite low in the soft x-ray regime. To make matters worse, the photons produced by the sample radiate in all directions equally, so that only a very small solid angle of the emitted photons strike the entrance slit of the spectrometer. Once the photons are past the entrance slit, they must pass over a grating which further cuts the intensity as it absorbs photons. Taken all together, even an expertly designed beamline is highly inefficient. Thus, nothing less than the very brightest sources can deliver a sufficiently high signal-to-noise ratio for photon-in photon-out experiments.

Much of the information concerning the optical components of a beamline, namely the slits and gratings that are found within spectrometers and monochromators, was presented in the work of W. B. Peatman [27].

CHAPTER 3

EXPERIMENTATION TECHNIQUES

3.1 X-ray Absorption Spectroscopy

X-ray absorption is the process during which an incoming photon is absorbed by an atomic site within the crystal; x-ray absorption spectroscopy (XAS) measures this process. The energy is absorbed primarily by the electron cloud, where it is used to promote electrons from their ground state into unoccupied states. If the absorbed photon energy and the binding energy of the electron are nearly equal, then the electron will be promoted to previously unoccupied bound states within the crystal, such as the conduction band. These bound states may be localized to the atomic site from which the electron was promoted, or they may be delocalized, allowing the electron to move somewhat freely within the crystal. However, if the excitation energy is much greater than the binding energy of the electron, then the electron may be promoted to unbound states. The electron becomes a free particle.

It is possible to promote any electron, provided that the absorbed photon had energy greater than the energy required to complete the transition. There are many possible transitions, but not all will have equal probabilities of occurring. Selection rules determine which type of radiative absorption process will dominate for a given excitation path; the possible processes are electric dipole-allowed, electric quadrupole-allowed, or magnetic dipole-allowed transitions. The transition probability for an electric dipole transition is generally at least three orders of magnitude greater than electric quadrupole- or magnetic dipole-allowed transitions. The selection rules for an electric dipole transition are listed in Table 3.1.

The selection rules in Table 3.1 apply in the case of Russells-Saunders coupling,

Table 3.1: Electric Dipole (E1) Selection Rules

$$\begin{aligned} \Delta S &= 0 \\ \Delta L &= 0, \pm 1 \\ \Delta J &= 0, \pm 1 \\ \Delta M_j &= 0, \pm 1 \end{aligned}$$

also called LS coupling. The S, L, and J letters in Table 3.1 refer to the spin, orbital angular momentum, and total angular momentum quantum numbers that describe the state of the atom. When LS coupling holds, the spins of the electrons are well-defined, as are the orbital quantum states. One can think of the selection rules for spin and orbital angular momentum as a consequence of the requirement for conservation of momentum. A photon has quantized spin, and the quantum number that describes the spin is 1. When an atom absorbs a photon, the quantum of spin of the photon must be accounted for, so the orbital angular momentum state of the atom must change by 1. However, the total spin cannot change. The total angular momentum selection rule is a consequence of the weak coupling of electron spin and orbital angular momentum.

The energy of the exciting photon is also a crucial factor in determining which of the possible transitions are most likely to occur. If the energy of the photon is equal or close to the energy of a transition, this excitation process will be preferentially populated over all other possible excitation paths. This is called *resonant excitation*. This property gives XAS site-selective, symmetry-selective, and element-specific properties because the binding energies for the core electron shells of a given element are unique to that element alone. During an XAS experiment, one can excite one element in a compound at its core electron threshold without fear that the spectra will become contaminated with spectral weight from the other elements.

X-ray absorption spectroscopy probes the unoccupied states of the atomic site that one is exciting. This is due to the so-called final-state rule, which states that the probability that a certain transition will occur, and the energy at which it occurs, is dominated by the final state configuration of the atom. The final state of an atom after absorbing a photon has a hole in a core shell and, in the case of resonant excitation, an extra electron in the previously unoccupied states. Because of the final-state rule, XAS probes the unoccupied states of the atom.

There are different ways to measure an XAS spectrum, and three of these methods will be discussed here. The first technique is *total electron yield* (TEY). The other two techniques of note are *total fluorescence yield* (TFY) and *partial fluorescence yield* (PFY). All three techniques are unique in that they use different detection methods to probe how efficiently the sample is absorbing the incident photons.

3.1.1 Total Electron Yield

The total electron yield (TEY) technique measures the rate at which electrons are replenished within the sample. This technique takes advantage of Auger decay processes, which strongly compete with radiative decay processes in the soft x-ray energy range. Simply stated, during an Auger relaxation event, the energy released when the core hole is refilled is transferred to another electron with the same principle quantum number. This energy is sufficient to ionize the atom and create a free electron. The possible relaxation paths that may be populated are shown in Figure 3.1.

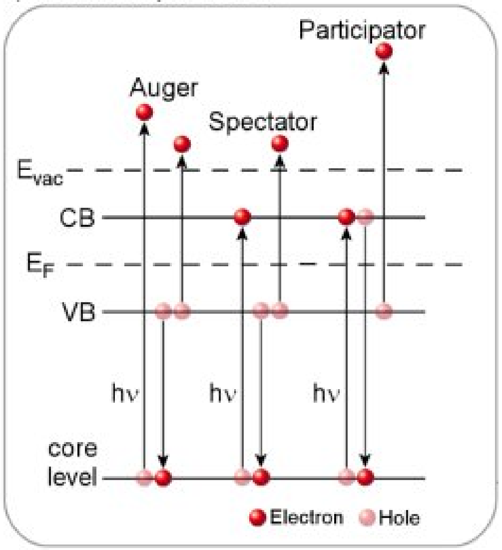

Figure 3.1: Possible Auger relaxation paths

Figure 3.1 shows three possible ways that an atom may produce an Auger electron. Firstly, the core electron may be excited to a bound state. If this electron, called the *participator*, refills its own core hole, then it may transfer the energy to a valence band electron and remove it from the atom. This is the process shown on the right. Alternatively, one of the other electrons in the atom may refill the core hole, which will typically be a valence band electron for light elements. These other electrons are referred to as *spectators*. This process is shown by the middle of Figure 3.1. Lastly, the participator electron may be removed from the atom, giving it an extra positive charge. In this case, shown on the left of the figure, only spectator electrons may refill the core hole. This Auger decay process leaves the atom doubly ionized.

Infused with energy approximately equal to the binding energy of a core electron, the free Auger electron can easily overcome the work function for the material. Before breaching the surface, the electron may scatter off other valence electrons. Each Auger electrons has energy much greater than the work function, so each one can scatter off several other valence electrons and impart each with sufficient energy to also escape. This causes a cascade of electrons, which includes the original Auger electron and any valence electrons from which it has scattered and given a significant amount of energy. This cascade escapes the sample into the vacuum surrounding the sample, which leaves a positive charge within the sample. This positive charge attracts electrons through a ground wire attached to the sample plate. This ground wire is the only external electrical connection that the sample plate is allowed, and the current that flows through it is measured using a picoammeter. A simplified setup is shown in Figure 3.2. This measurement of ground-to-sample current as a function of excitation energy constitutes a TEY spectrum.

It is implicitly assumed that the probability of an Auger relaxation occurring is constant over the energy range of the excitation threshold that is being probed. Of course, there are no Auger processes below threshold, as there is no core hole to fill. This is a very good approximation, and as such TEY is an accurate representation of the true XAS spectrum. However, this method can have some problems. TEY

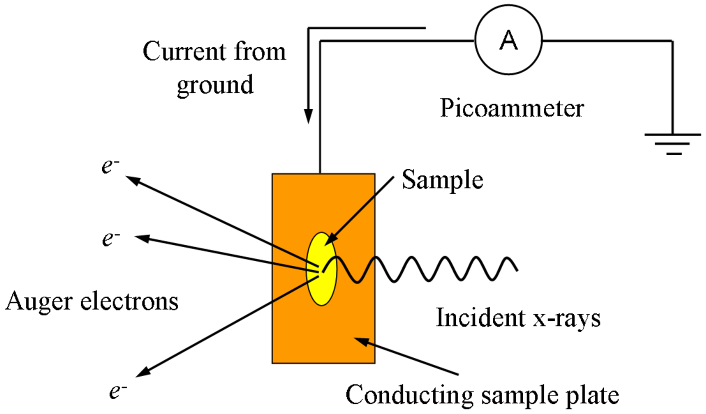

Figure 3.2: Simplified setup for a TEY experiment

measures the rate at which valence holes are replenished within the sample, which depends upon the conductivity of the sample. Conductivity can be assumed to be constant over the whole threshold, but poor conductivity, when measuring highly insulating materials, can lead to poor count rates and possibly to sample charging. Sample charging occurs when the electrons that are ejected into space cannot be replenished quickly enough by an external source. The sample builds a positive charge, which increases the amount of energy that electrons require to break free of the sample. In short, the work function is not constant across the scanned energy range. Sample charging is easily recognized by a noticeable, often steep drop in the measured ground-to-sample current. This drop is due to the inability of the Auger electrons to break free of the increasingly steep positive potential well, which leads to lower count rates. The positive charge on the sample is sufficient to inhibit photoelectrons from leaving the surface, but it is not enough to increase the current because the potential is not great enough to cause dielectric breakdown. Dielectric breakdown would of course be undesirable, as it would significantly distort the electronic structure of the sample.

TEY is also highly sensitive to surface effects. The electrons that are produced by the Auger process have a short mean free path length, on the order of a few Angstroms, which means that the electrons cannot travel far within the crystal without interacting with the lattice. Electrons produced by deep-lying atoms are recaptured by the crystal before escaping into space. Thus, electrons that exist in surface states tend to dominate a given TEY spectrum. This is problematic for metastable or highly reactive systems, such as the pure transition metals that oxidize very quickly upon exposure to atmosphere.

3.1.2 Total Fluorescence Yield

The problems inherent to TEY can be overcome to a certain extent by using the total fluorescence yield (TFY) technique. The TFY technique differs from TEY in that it measures the photons that are emitted from the sample when the atoms radiatively de-excite. This is very different from TEY, which depends upon the Auger process in which the energy of the excited state is carried away by an electron. A TFY experiment typically uses a Channeltron, a device that records the electron cascade that occurs when a photon interacts with the detector. Since electrons that strike the detector can cause a similar electron cascade, the Channeltron has a bias voltage that repels any electrons that are emitted from the sample. The spectrum produced by an absorption experiment measured in TFY mode is simply the number of counts that the Channeltron recorded as a function of excitation energy.

The TFY experimentation technique records the photons emitted from the sample, which has both its advantages and its disadvantages. The upside of TFY is that it has better penetration depth, because photons penetrate more deeply than electrons. This removes the problem of surface effects dominating the measured absorption spectrum. Also, TFY is the technique of choice when dealing with highly resistive materials, as sample charging is not a relevant problem. The downside of TFY is that it senses emitted photons. In the soft X-ray energy range, Auger and radiative processes compete to refill the core hole, and the Auger decay channel strongly dominates, especially with the lighter elements. Thus, TFY can have a prohibitively poor signal-to-noise ratio simply because the probability of a photon being produced is so small, relatively speaking. There is also the problem of self-absorption. Self-absorption is difficult to take into account because it is not uniform across the entire threshold; the more intensely photons are radiated at a certain energy, the more strongly those photons are absorbed by other atomic sites in the crystal as the photons attempt to escape the crystal. Thus, TFY spectra inherently have skewed intensity profiles, as the most intense peaks seen in the spectrum should be even larger if self-absorption was not present. When using a Channeltron to record TFY spectra, problems may arise because of the bias voltage of the Channeltron. The bias voltage is necessary to keep the Auger electrons away from the detector, but if the voltage is set too high, it may distort the electronic states of the crystal. Despite these limitations, however, the TFY technique can produce excellent spectra that are much more representative of the bulk states than a TEY experiment.

TFY and TEY share a common property in that any spectrum that is recorded using one of these two methods is not simply an absorption spectrum of the core threshold this one is resonantly exciting, but rather a spectrum of all thresholds accessible at that excitation energy. For example, consider an iron oxide compound. The $L_{2,3}$ edge of Fe requires photons of approximately 705 eV to begin resonantly exciting the $2p$ electrons. At this energy, however, it is in principle possible to excite the $1s$ electrons of the O ions that share the crystal, given that the K edge on O only requires $\approx$510 eV. Of course, photons with energies around 705 eV will not resonantly excite the K edge of oxygen; the probability of producing a $1s$ core hole on O is minuscule compared to the probability of created a $2p$ hole on Fe. Nevertheless, it can still happen. The Channeltron detects any photon that fits within its energy detection window, even if it was not produced though decay of the core hole that is being resonantly created. As a result, TFY spectra, and similarly TEY spectra, sit upon a substrate of signal produced by the decay of lower energy core holes that were produced non-resonantly as the incident radiation strikes ligand states.

This appears easy to correct. It seems logical to assume that the cross-section for the O K edge, in this example, will remain unchanged as one encounters the Fe $L_{2,3}$ edge. After all, the Fe $L_{2,3}$ edge is nearly 200 eV above the O K edge, which is well beyond any possible multiplet effects due to the O site. However, this is not the case. Experiments that probe the photoemission yields at a higher lying threshold on one element while exciting a deeper core level on another element within the same crystal clearly show that the number of photons produced though decay of higher-lying core holes is dramatically curtailed as a deeper core level is resonantly probed [28]. Thus, TFY and TEY spectra are in principle highly complicated spectra, with components from higher-lying core thresholds varying just as much as the signal from the threshold under scrutiny. However, most of the time the background signal is negligible, and the signal from the decay of the resonantly created core holes far outweighs all other components.

3.1.3 Partial Fluorescence Yield

Partial fluorescence yield (PFY) is a third technique that can be used to measure XAS. Like TFY, the PFY technique measures the photons that are produced by the sample. PFY has all the aforementioned advantages and disadvantages of the TFY technique. Unlike TFY, however, the photons are detected using a spectrometer. It is unnecessary for a spectrometer to have a bias voltage to repel emitted electrons, so there is no danger that the spectrometer will affect the electronic states of the sample.

When measuring a TFY spectrum, the Channeltron simply counts the number photons that strike the sensor. However, the spectrometer has its own transmission efficiency because the fluorescence photons must pass an entrance slit and a grating, and as such a lot of flux is lost in the process of producing a PFY spectrum. This generally means that PFY spectra have the poorest signal-to-noise ratio of all three techniques discussed thus far. The problem of low emitted photon flux can be mitigated somewhat by increasing the incident photon flux. However, this invariably reduces the resolution of the resultant spectrum.

Although the spectrometer does significantly decrease the signal-to-noise ratio, the energy detection window of the spectrometer is very much smaller than those of the Channeltron or the picomammeter. This gives the PFY technique a property that sets it distinctly apart from TEY and TFY: a PFY spectrum does not measure extraneous signal produced by the decay of holes other than the ones resonantly created. The detection window can be tuned to a particular transition energy range.

This allows the experimentalist to know explicitly what it is that he is measuring, even if the spectrum that is being measured takes an exceedingly long time to acquire.

3.2 X-ray Emission Spectroscopy

X-ray emission spectroscopy (XES) measures the photons that are emitted from the sample using a spectrometer. Just as for XAS, the final-state rule applies to XES as well, except that in the final state of all XES events, there is no core hole and one hole in the valence band. XES techniques therefore probe the occupied states, as the multiplet effects from the new hole in the occupied states gives an XES spectrum its shape. The physical mechanism that produces the photons, however, can be quite different depending on how close the energy of the exciting radiation is to a core hole excitation threshold. Excitation energies that are relatively far above threshold produce non-resonant XES spectra, whereas at excitation energies that are near- or on-threshold, the dominant process is resonant inelastic x-ray scattering (RIXS). Both of these mechanisms are photon in-photon out process, and are displayed in Figure 3.3.

Simple XES can, in principle, happen at all excitation energies. XES is a two-step process; the first step is the creation of a core hole. The photons measured in XES are produced when the core hole is refilled by either the participator electron or another spectator electron. The relevant spectator electrons are the valence electrons. In principle, any electron can refill the core hole, provided that the necessary transition satisfies the dipole selection rules, but the emitted photons are too low in energy to be seen within the detector window of the spectrometer. The left panel in Figure 3.3 shows the total process. Note that the figure shows that the electron is promoted to the unoccupied states. While this is in general true, XES is most probable in the non-resonant case at excitation energies far above threshold. In this case, the core electron is removed from the atom, leaving the atom ionized.

RIXS is the photon-out process which is the more likely for on-threshold energies. RIXS is a one-step scattering process, wherein the scattering transition is the net

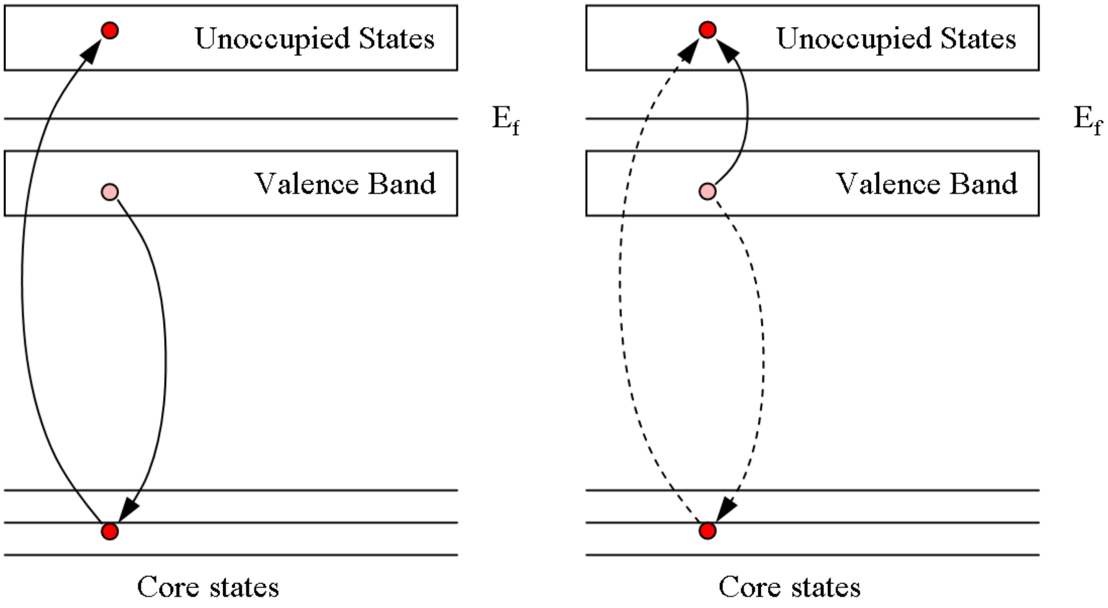

Figure 3.3: Photon-in photon-out processes. The left panel represents simple fluorescence, or XES. The photon that is emitted has energy equal to the decay of the core hole. The right panel shows the net transition of a RIXS event. The photon that is emitted is the excitation energy with the energy of the net transition subtracted from it.

result of virtual core hole creation and annihilation events [29]. The right panel in Figure 3.3 displays a RIXS event; the dashed lines are the virtual transitions, whereas the solid line is the transition that physically occurs. A RIXS event is the result of two independent dipole-allowed events, and as such, the selection rules for high-probability net transitions are slightly modified. The spin selection rule remains the same ($\Delta S = 0$), but angular momentum selection is altered to become $\Delta L = 0, \pm 2$. This allows one to efficiently probe inner-shell transitions.

Although XES and RIXS events each have the same final state, i.e. an electron in the conduction band and a hole in the valence band, the physical mechanism that promoted the electron differs greatly between the two processes. In XES, the photon that is detected by the spectrometer has energy equivalent to the energy separation of the valence and core states, because the photon is created to carry away the energy that is released when the core hole is annihilated. This energy separation does not change with excitation energy. This will have the effect that inelastic XES peaks will maintain a constant energy, even though the elastic peak will track with the excitation energy. This concept is displayed in Figure 3.4(a).

RIXS features, however, are quite different. The energy losses in RIXS typically correspond to the transition in which valence electrons are scattered to unoccupied states; the total energy necessary to complete the net transition is always the same for a given scattering transition. This energy is subtracted from the energy of the photon that is exciting the atom. The photon that is sensed by the spectrometer has an energy that is the original excitation energy minus the energy required to complete the transition. Thus, a feature that maintains the same energy separation from the elastic peak, regardless of excitation energy, is an inelastic scattering peak. An example of the evolution of an inelastic scattering feature is shown in Figure 3.4(b).

The probability that a RIXS event will occur is determined by the Kramers-Heisenberg formula. The Kramers-Heisenberg formula was originally derived without the use of quantum mechanics by H. A. Kramers and W. Heisenberg to describe the scattering of a photon by an atomic electron, but was later derived using quantum mechanics by Dirac [30, 31]. The Kramers-Heisenberg formula for the intensity of a scattered photon at a particular emission energy E_{out} is shown below:

$$I(E_{in}, E_{out}) \propto \sum_f \left| \sum_m \frac{\langle f| f \cdot A |m\rangle \langle m| f \cdot A |i\rangle}{E_m - E_i - E_{in} - i\frac{\Gamma}{2}} \right|^2 \delta(E_f + E_{out} - E_i - E_{in}) \quad (3.1)$$

where the symbol E refers to energy, with the subscripts f, m, and i refer to the final, intermediate, and initial states, respectively. The subscripts in and out refer to the incident and scattered photons.

The Kramers-Heisenberg formula has two parts that require explanation. Firstly, there is the numerator, which is the product of two matrix elements. One matrix element represents the dipole-allowed transition from an initial state to an intermediate state, and the second matrix element is the dipole-allowed relaxation of that intermediate state to a final state. The denominator is the second part of note, and its function is to magnify the intensity of the inelastic process described by

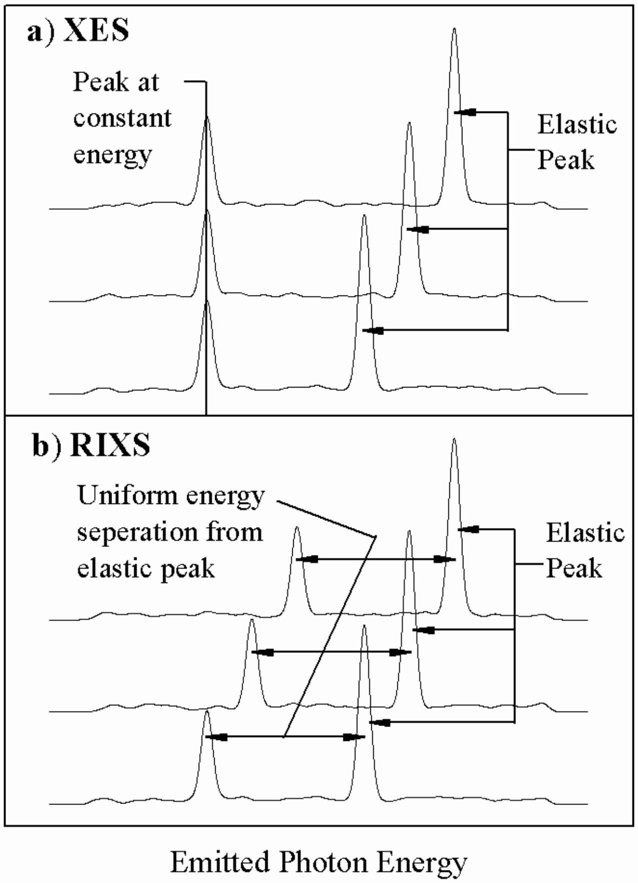

Figure 3.4: Examples of XES and RIXS peaks in experimental spectra. These spectra are not real, but have been simulated to exemplify the expected behavior of typical soft x-ray photon-out processes. Each spectrum in each panel corresponds to a different excitation energy.

the numerator when the excitation energy, E_{in}, comes near to the energy difference between the intermediate and initial states, $E_m - E_i$. To prevent the denominator from becoming undefined, an imaginary quantity Γ has been introduced, which is the lifetime broadening of the intermediate state. The denominator describes the resonance part in the term 'resonant inelastic x-ray scattering'.

RIXS, in particular, is a very powerful technique for studying the density of states of a system. Inelastic scattering features maintain a constant energy separation from the elastic peak. This energy is characteristic of the net transition. This gives information about the partial DOS, because each inelastic energy loss feature represents a transition between a local maximum in the occupied states and a local maximum in the unoccupied states. Thus, one can get specific information about the electronic structure.

Another benefit is that RIXS is element-specific. This is because a RIXS feature is the net result of two virtual transitions, one of which is core hole creation, a process that is characteristic of the element in question. This property allows one to probe site-specific states without spectral weight from other elements contributing to the measured spectrum. Optical absorption similar to RIXS, because both techniques have the same net transition and thus probe the same states. Optical absorption is superior for determining DOS fine structure that cannot be resolved using RIXS, however, optical absorption probes the near-Fermi edge DOS of every atomic site in the entire crystal. The element-specific RIXS technique allows one to probe the local DOS of only the resonantly excited element, although that local DOS will have some structure that results from inter-atomic interaction.

CHAPTER 4

ELECTRONIC STRUCTURE OF SOLIDS

4.1 Band Structure Basics

The physics of condensed matter marks a strong departure from the physics of the comparatively simpler atomic picture. The most obvious difference is that a given atom in the solid is not in a spherically symmetric environment. Electrons from neighboring atoms interact with each other, and charge clouds overlap to form bonds. In addition, if one considers a crystalline sample, wherein the atoms have bonded with long-range ordering, then the electronic structure shows periodic structure. Theory pertaining only to the electronic structure of crystals will be considered in this thesis, although in principle matter can condense in a completely unstructured (amorphous) phase.

The periodicity of the structure within a crystal, both physical and electronic, lends itself conveniently to Fourier analysis, as Fourier analysis involves expanding a function in terms of periodic functions, most commonly sinusoids. As an example, the electronic charge density $n(\mathbf{r})$ can be expanded in the following Fourier series:

$$n(\mathbf{r}) = \sum_G n_G \exp(i\mathbf{G} \cdot \mathbf{r}) \tag{4.1}$$

In this expansion, $\mathbf{G}$ is the reciprocal lattice vector, defined by the relation $\mathbf{G} \cdot \mathbf{T} = 2\pi n$, where n is an integer and $\mathbf{T}$ is the translation vector of the crystal lattice. The reciprocal lattice is a powerful concept, as it represents the crystal lattice transformed into crystal momentum space, or k-space as it is more commonly called. One important property to note is that the length of k-space and real space vectors reciprocally scale with respect to one another. Thus, a large r-space vector transforms into a short k-space vector, and vice versa.

The Bloch theorem states that solutions to the Schrödinger equation in a periodic potential must also be periodic. These solutions have the form:

$$\psi_{i,\mathbf{k}}(\mathbf{r}) = u_{i,\mathbf{k}}(\mathbf{r}) \exp(i\mathbf{k} \cdot \mathbf{r}) \tag{4.2}$$

where $\mathbf{k}$ is a reciprocal lattice vector, and i gives the state that the wavefunction is describing, including symmetry labels and quantum numbers. This formula shows that for a certain wavevector $\mathbf{k}$ and state i, there is only one possible solution to the Schrödinger equation, and thus one energy eigenvalue that can be observed. Other states may exhibit this energy at the same wavevector, if they are degenerate. However, each eigenvector can only have one eigenvalue for each $\mathbf{k}$. Recalling the periodicity of a crystal, each translationally invariant atom within the crystal will provide electrons with the same state, but with different values of $\mathbf{k}$. Because k-space vectors and r-space vectors scale reciprocally, solutions to the Schrödinger equation with index $\mathbf{k}$ are possible every $2\pi/N$ wavevectors, where N is the number of atoms in the crystal. Therefore, as the number of atoms in the crystal increases, eigenvalues $\varepsilon_{i,\mathbf{k}}$ are nearly continuous with $\mathbf{k}$ for state i.

Another way of looking at it is to consider what happens when identical atoms are brought close enough such they may interact with one another, and are arranged in a periodic fashion. As the valence electrons on each site begin to interact, the problem arises that the electrons that occupy the same orbitals on different atoms are no longer unique. The orbitals that these electrons occupy are exactly the same within an integer number of lattice translations. This is not acceptable, as no two electrons can occupy the same orbital at the same time. The solution is to modify the wavefunctions of the valence electrons such that they are no longer orthogonal, which allows the valence electrons to coexist. The result is valence electrons that have the same electronic environment but have different energies, depending on their momentum.

Either way that one looks at it, the result is the same. The interaction amongst electrons in an extended solid produces continuous band structure, with the energy of the band varying as a function of $\mathbf{k}$. Band structure calculations are powerful analytical tools, as they predict the energies of the transitions that are possible given a certain symmetry axis. However, one can also look at the electronic density of states (DOS) as a meaningful representation of the electronic structure of a crystal. The band structure and the density of states of a crystal are related simply through the following formula:

$$D(E) = \frac{V}{(2\pi)^3} \int \frac{dS_E}{|\nabla_{\mathbf{k}} E(\mathbf{k})|} \tag{4.3}$$

where S_E is a surface area element on a constant energy surface of the three dimensional band structure, and $\nabla_{\mathbf{k}} E(\mathbf{k})$ is the gradient of the band structure with respect to $\mathbf{k}$. The important property to note here is that the density of states is inversely proportional to the gradient of the band structure. A flat band produces a sharp peak in a graph of the DOS at that energy, whereas a band with a lot of structure will produce broad features in the DOS. Of course, a large gradient with respect to $\mathbf{k}$ within a band suggests a large degree of electron cloud interaction as per the discussion above. Thus, a graph of the density of states gives a visual and intuitive look at the level of interaction that the band in question is experiencing.

Although the presence of band structure is a result of the periodicity of the crystal, determining the shape of the band structure is a very complicated problem. As stated above, the shape of the band, and therefore the density of states, is directly dependant upon the symmetry and magnitude of the interactions amongst the electron clouds of the atoms, as well as the interactions between the electrons and the fixed atomic nuclei. There have been many attempts to understand and simulate the dynamics of a crystalline system. The *orthogonalized linear combination of atomic orbitals* (OLCAO) method was used to simulate $LiFePO_4$, a subject that will be discussed later in this chapter. This method is based upon the formalisms introduced by the *local density approximation* (LDA) of *density functional theory* (DFT).

4.2 Density Functional Theory

Density functional theory was formulated by Hohenberg and Kohn as an exact theory for many-body interactions. The guiding principle behind DFT is a deceptively simple one: All properties in a solid, including (but not limited to) electronic excitations, thermal and electrical conductivity, and magnetic susceptibility are all functionals of the ground state electron charge density. If one knows the ground state electron charge density, then one could in principle calculate all other macroscopic properties of a solid with this information alone.

The following formula is the Hamiltonian proposed by Hohenberg and Kohn.

$$\hat{H} = -\frac{\hbar^2}{2m_e}\sum_i \nabla_i^2 + \sum_i V_{ext}(\mathbf{r}_i) + \frac{1}{2}\sum_{i\neq j}\frac{e^2}{|\mathbf{r}_i - \mathbf{r}_j|} \tag{4.4}$$

The first term in this Hamiltonian is simply the kinetic energy operator. The second term takes into account any external fields, including all fields that are not generated by the electrons within the crystal. This term must account for the Coulomb electric field produced by the fixed ionic lattice, but in principle this term may also include fields generated outside of the crystal. The last term explicitly accounts for two-electron Coulomb interactions. Depending on the wavefunctions upon which this Hamiltonian operates, the interactions can be of the direct, exchange, or correlation type.

According to the Hohenberg-Kohn theorems, the external potential is uniquely determined by the ground state particle density, which will be stated here without proof. The kinetic energy term and the electron-electron interaction term are by definition unique to a particular electron density, and so the full Hohenberg-Kohn Hamiltonian is uniquely determined for a particular electron density. The total energy, which is simply the observable eigenvalue of the full Hamiltonian, is also uniquely determined by a given electron density. The density that minimizes the total energy is, by definition, the ground state particle density. The total energy is given as follows:

$$E_{HK}[n] = T[n] + E_{int}[n] + \int d^3r V_{ext}(\mathbf{r})n(\mathbf{r}) + E_{II} \tag{4.5}$$

The third term is the energy of the interaction between the electrons and the fixed ionic lattice. The fourth term is simply the energy of the ions interacting with one another, hence the II subscript. These are straightforward to calculate, if one knows the density. The first term is the total kinetic energy, and the second term is the so-called internal energy, which is the energy that is inherent in the electron-electron interaction. The first and second terms are much more difficult to calculate than the third and fourth terms, for different reasons. The main problem arises from the kinetic energy term. At present, there is no known way to calculate the kinetic energy directly from the electron charge density.

Despite its intractability, the Hohenberg-Kohn Hamiltonian is nevertheless exact. The Hohenberg-Kohn Hamiltonian can be generalized to include time dependance. Any state to which the system may be excited will have a different electron configuration, however the system must nevertheless start in the ground state, and thus the excited electron density must be a functional of the ground state density. This is in keeping with the Hohenberg-Kohn theorem. The exact Hamiltonian should also have the capacity to accurately calculate Fermi surfaces, as well as the transition between a conductor and a Mott insulator. Thus, density functional theory holds great promise, if only it were possible to calculate the kinetic energy of the system. Kohn and Sham were to find just such a solution with the celebrated Kohn-Sham equations.

4.2.1 Kohn-Sham Equations

The Hohenberg-Kohn theorem, and its accompanying exact Hamiltonian, provided a tantalizing goal. According to this hallmark theorem, it is possible to calculate all macroscopic properties of a crystal, although it is technically impossible to do the necessary calculations within the understanding of modern physics. This problem was impossible to solve, so Kohn and Sham simply avoided the problem by replacing the exact many-body Hamiltonian with an auxiliary independent particle one. The Kohn-Sham ansatz assumes that the ground state electron density is exactly the same for the independent particle approximation as for the full many-body solution. The power of this technique is that the electron charge density is understood in terms of independent particle wavefunctions. It is known how to calculate the kinetic energy from such wavefunctions, eliminating one of the chief restrictions to solving the full Hohenberg-Kohn equations directly. The Kohn-Sham equations are as follows, written in Hartree units.

$$H^{\sigma}_{KS}(\mathbf{r}) = -\frac{1}{2}\nabla^2 + V^{\sigma}_{KS}(\mathbf{r}), \tag{4.6}$$

$$V^{\sigma}_{KS}(\mathbf{r}) = V_{ext}(\mathbf{r}) + \int d\mathbf{r}' \frac{n(\mathbf{r}')}{|\mathbf{r}-\mathbf{r}'|} + V_{xc}[n] \tag{4.7}$$

where

$$V_{xc}[n] = \frac{\delta E_{xc}}{\delta n(\mathbf{r},\sigma)} \tag{4.8}$$

The Kohn-Sham Hamiltonian, Equation 4.6, is the operator in a Schrödinger-like equation, referred to specifically as the Kohn-Sham equation, or alternatively the KS equation.

$$\left[-\frac{1}{2}\nabla^2 + V^{\sigma}_{KS}(\mathbf{r})\right]\psi^{\sigma}_{i}(\mathbf{r}) = \varepsilon^{\sigma}_{i}\psi^{\sigma}_{i}(\mathbf{r}) \tag{4.9}$$

In these equations, the σ represents spin and $\mathbf{r}$ is the point of interest where the Kohn-Sham equations are being solved. The V_{ext} term in Equation 4.7 is the potential exerted by the ionic lattice on the electrons. The second term calculates the direct Coulomb interaction between the charge cloud located at the point of interest $\mathbf{r}$, and the charge cloud at some other field point $\mathbf{r}'$. The last term in Equation 4.7, V_{xc}, is the potential due to the exchange-correlation interaction. This term contains all of the non-direct electron-electron interaction terms, namely the exchange and the correlation effects. This potential depends upon the exchange-correlation energy, given by Equation 4.8, which will be discussed in detail later.

Rigourously speaking, the direct and exchange Coulomb interactions and the correlation interaction are all consequences of the same two-electron, four-center integral, given in Equation 4.10 [32]. As stated earlier, however, the direct Coulomb interaction is the only one that can be tractably calculated explicitly, whereas the other two interactions require some level of approximation. The direct Coulomb interaction comes out of Equation 4.10 when $\mu = \delta$ and $\gamma = \nu$, and when $I = L$ and $K = J$, thus effectively reducing the formula to a two-electron, two-center integral.

$$\langle \mu\gamma|\nu\delta\rangle = \int\int d\mathbf{r}d\mathbf{r}'\phi^*_\mu(\mathbf{r}-\mathbf{R}_I)\phi^*_\gamma(\mathbf{r}-\mathbf{R}_K)\frac{1}{|\mathbf{r}-\mathbf{r}'|}\phi_\nu(\mathbf{r}'-\mathbf{R}_J)\phi^*_\delta(\mathbf{r}'-\mathbf{R}_L) \quad (4.10)$$

The process to find the ground state electron charge density and potential that minimizes the total energy is iterative, and it begins with an initial educated guess as to what the ground state density may be. This guess may actually be in the form of a charge distribution $n(\mathbf{r})$, but much more commonly, the guess is a set of one-electron wavefunctions. These wavefunctions are usually linear combinations of some basis set, such as plane waves or atomic orbitals. The charge density may be calculated from these wavefunctions as shown in Equation 4.11.

$$n(\mathbf{r}) = \sum_\sigma \sum_{i=1}^{N^\sigma} f_i^\sigma |\psi_i^\sigma(\mathbf{r})|^2 \quad (4.11)$$

where the subscript i denotes a quantum state of spin σ characterized by the wavefunction $\psi_i^\sigma(\mathbf{r})$. The term f_i^σ is called the *density matrix.* This corresponds to the basis set representation of the one-body density operator $n(\mathbf{r},\mathbf{r}')$. This density operator is calculated from the expansion coefficients for the basis functions that add together linearly to construct the wavefunctions $\psi_i^\sigma(\mathbf{r})$ that describe the quantum states of the crystal [32].

The electron charge density, and the independent particle wavefunctions that gave rise to this density, are both necessary inputs to the total energy functional, E_{KS}, as well as the Kohn-Sham potential V_{KS} given by Equation 4.7. As stated earlier, the total energy must be at an absolute global minimum before one can unambiguously state that the ground state electron charge density has been found.

The total energy is calculated as follows:

$$E^{\sigma}_{KS}(\mathbf{r}) = T_s[n] + \int d\mathbf{r} V_{ext}(\mathbf{r}) n(\mathbf{r}) + E_{Hartree}[n] + E_{II} + E_{xc}[n] \tag{4.12}$$

The second term is the energy contribution due to the interaction of the electrons with the nuclei and any other applied external field. The third and fourth terms, $E_{Hartree}[n]$ and E_{II}, are the direct electron-electron Coulomb interaction and nuclei-nuclei interaction, respectively. As before, the $E_{xc}[n]$ is term that brings together the exchange and correlation electron-electron interactions. The first term, $T_s[n]$, is the kinetic energy term calculated as follows.

$$T_s = -\frac{1}{2} \sum_{\sigma} \sum_{i=1}^{N^{\sigma}} \int d\mathbf{r} |\nabla \psi_i^{\sigma}(\mathbf{r})|^2 \tag{4.13}$$

Once the total energy is known, then one can calculate the energy eigenvalues for each state $\psi_i^{\sigma}(\mathbf{r})$.

$$\varepsilon_i = \frac{dE_{total}}{dn_i} = \int d\mathbf{r} \frac{dE_{total}}{dn(\mathbf{r})} \frac{dn(\mathbf{r})}{dn_i} \tag{4.14}$$

The electron charge density $n(\mathbf{r})$ has, at this point, been used to calculate the Kohn-Sham potential and the energy eigenvalues that can be substituted into the Kohn-Sham equation (Equation 4.9). The Kohn-Sham equation can then be solved, through various means, to find eigenstates $\psi_i^{\sigma}(\mathbf{r})$. Unless the initial guess for the electron charge density is an exact solution of the Kohn-Sham equation, then the calculated eigenstates will not be the same as the wavefunctions used as the input. Once a solution to the Kohn-Sham Hamiltonian has been found, then one can use the new wavefunctions to calculate the charge density. This again can be used as input to the total energy functional, and the new total energy is compared to the previous value. If the total energy is *self-consistent*, i.e. if the first and second total energies differ within an acceptable margin, then the energy has been minimized and the electron charge density is the ground state density. Otherwise, the density is varied in some systematic manner, and the next educated guess as to the ground state density is used to calculate the next Kohn-Sham potential and eigenvalues. Thus continues the iterative process until self-consistency is reached.

4.2.2 Exchange and Correlation

The Kohn-Sham equations provide a plausible way to calculate the electronic structure of a crystal. One of its advantages over the exact Hohenberg-Kohn method is that the independent particle approximation allows for the calculation of the kinetic energy of the electron cloud. However, it also has the advantage that it separates the long-range kinetic and direct Coulomb interactions from the exchange and correlation interactions. Exchange and correlation are the names given to the electron-electron interactions that arise due to the overlap of electron wavefunctions, as opposed to the direct Coulomb interaction, which is simply electrostatic repulsion. The exchange interaction is primarily concerned with the overlap of electron wavefunctions with parallel spin. It naturally includes the Pauli exclusion principle, which doesn't allow electrons with parallel spin to occupy the same orbital due to the antisymmetric nature of fermion wavefunctions. Correlation deals with the interaction of electrons with antiparallel spin. The spin part of an electron wavefunction does not prohibit opposite-spin electrons from being close to one another, however opposite spin electrons do occupy orbitals wherein the spherical harmonics are orthogonal. This prevents them from overlapping in a spherical potential. Both exchange and correlation decrease the total energy, because these repulsive interactions decrease the amount of energy that the direct Coulomb interaction requires to keep electrons apart.

Correlation in particular has classically proven to be difficult to calculate, due to the incredible amount of computing power required for an exact value of the correlation energy to be obtained. However, the Kohn-Sham equations have the exchange and correlation potentials as functionals of the local density only. This makes the calculation of these energies tractable. One of the most popular forms of the exchange-correlation functional is that of the local density approximation (LDA). The energy of the exchange and correlation interactions is given by the following formula in the exact Kohn-Sham theory:

$$E_{xc}[n] = \int d\mathbf{r} n(\mathbf{r}) \epsilon_{xc}([n], \mathbf{r}) \tag{4.15}$$

where $\epsilon_{xc}([n], \mathbf{r})$ is the exchange-correlation energy density per electron at point $\mathbf{r}$ that depends only on the density $n(\mathbf{r}, \sigma)$ in some volume around $\mathbf{r}$. This quantity can be separated into the exchange and correlation parts, such that $\epsilon_{xc} = \epsilon_x + \epsilon_c$. In the LDA approach, the exchange-correlation energy density is assumed to be identical to the energy density of the homogenous electron gas with the same density. The agreement to theory therefore depends on how well the electron density in the crystal is approximated by an electron gas. With metals, this concept provides a fair approximation, but fails with highly inhomogeneous compounds. Even with metals, however, this approach has its failings, as will be discussed later in this section.

Note that the Kohn-Sham equations make a local density approximation, in the sense that the exchange-correlation functional is assumed to depend only upon the local density. This is not to be confused with the LDA formalism, which represents a family of exchange-correlation functionals that have a certain form and exhibits certain properties. Although there are different forms of the exchange-correlation functional available, such as the generalized gradient approximation, all of the them are functionals of the local density only.

The approximation that the Kohn-Sham exchange-correlation functional depends only upon the local density makes the Kohn-Sham equations calculable, but it does make them inaccurate in certain circumstances. In particular, the Kohn-Sham equations struggle when one tries to calculate the electronic structure of metals and insulators, albeit for very different reasons. The problem with metals arises because the exchange-correlation functional depends on the local density only. Although the local density will be reproduced, and the Kohn-Sham equations will correctly predict the metallic nature of the crystal, the Fermi surface will not be accurate. This is because the shape of the Fermi surface is a long-range effect that the local density approximation for the exchange-correlation functional does not adequately model. The same approximation is the reason for the failure of the Kohn-Sham equations to predict the conductor-Mott insulator transition in transition metal oxides. The local density approximation does not predict the correlation energy to be strong enough.

The capability of the Kohn-Sham equations to model Mott insulators can be improved substantially by incorporating some of the ideas put forward by Hubbard, who designed a model for interacting electrons. The Hubbard Hamiltonian accounts for electron correlation using the following interaction matrix:

$$U \sum_{R} n_{R\uparrow} n_{R\downarrow} \tag{4.16}$$

The arrows denote the spins of the electrons. The quantity U, called the Hubbard-U, is a special case of the general four-center integral that is shown as follows. The Hubbard-U is calculated when $R_1 = R_2 = R_1' = R_2'$.

$$V_{R_1 R_2 R_1' R_2'} = \frac{1}{2} \int d\mathbf{r} \int d\mathbf{r}' \phi^*(\mathbf{r} - \mathbf{R_1}) \phi^*(\mathbf{r} - \mathbf{R_1'}) \frac{1}{|\mathbf{r} - \mathbf{r}'|} \phi(\mathbf{r}' - \mathbf{R_2'}) \phi(\mathbf{r}' - \mathbf{R_2}) \tag{4.17}$$

This formula gives the interaction strength of two electrons on the same site with opposite spins. This is the definition of electron correlation. In terms of the physics, the Hubbard correlation interaction applies an orbital-dependant potential on the atomic sites.

The Hubbard Hamiltonian is instructive because it has been used successfully to model the transition between a Mott insulator and conductor in some of the highly correlated transition metal oxides. It does this through the competition of the correlation interaction U and the hopping probability t. When $4t > U$, the hopping probability dominates and the electrons can move freely about the crystal. The band structure is that of a metal. However, when $U > 4t$, the correlation interaction dominates and the occupied and unoccupied states are split apart, causing the electrical resistivity to increase dramatically. The energy difference between the upper and lower Hubbard bands is U.

For the description of highly correlated systems, the Hubbard-U approach is much better at describing the electronic structure than LDA treatments. However, for weakly correlated systems, the Hubbard Hamiltonian fails. The splitting of the conduction and valence bands is determined by the competition of U and the hopping probability t, and the competition of U and t is decided in large part by the temperature. Thus, in the case of $U > 4t$, the conduction and valence bands are always split, which of course is not the case for many systems, including metals. Thus, the LDA and Hubbard Hamiltonians each have their place in describing condensed matter physics.

The Hubbard-U has been incorporated into the LDA Hamiltonian with the following formula:

$$E_{LDA+U}[n] = E_{LDA} - \frac{1}{2}U \cdot N(N-1) + \frac{1}{2}U \sum_{i \neq j} n_i n_j \tag{4.18}$$

where n_i is the orbital occupancy. The first term deletes the interaction energy of the $d - d$ interactions that the LDA Hamiltonian calculates, and the second term replaces the first with the Hubbard correlation. Note that only the $d - d$ interactions are dealt with, because electron correlation is generally not an important concern for $s-$ or $p-$symmetry electrons.

The Kohn-Sham equations have difficulty calculating the correct electronic characteristics of insulators. The valence band is a completely full shell in the case of a classic insulator, so the conduction band is an empty band that is a different symmetry than the valence band. Calculating the size of the gap between the two bands has proven to be difficult, due to the different natures of the valence and conduction bands. Because the two bands have different symmetries, the character of the wavefunctions of the bands changes considerably. This leads to a discontinuous change in the kinetic energies of the two bands, because the kinetic energy is dependant on the independent particle wavefunctions of the bands. This discontinuity is expected from quantum mechanics, and is not an artifact of improper modeling within DFT. However, the exchange-correlation potentials that are commonly incorporated into the Kohn-Sham equations, such as the LDA and GGA functionals, do not have this discontinuity. Even in the exact Kohn-Sham theory, which assumes that the exact form of the exchange-correlation functional is known, the nature and magnitude of the discontinuity between bands is not understood.

4.2.3 OLCAO Method

The Kohn-Sham equations provide a tractable method for calculating the electronic structure of a crystal, as these equations recast the Hohenberg-Kohn equations in terms of an independent particle picture that depends upon one-particle wavefunctions. It therefore remains to find appropriate one-particle wavefunctions from which one may start solving the self-consistent Kohn-Sham equations. A natural choice for the basis functions of the one-particle wavefunctions are atomic orbitals, given that crystals are simply atoms bonded to one another. The linear combination of atomic orbitals (LCAO) method uses just such a basis of atomic-like orbitals. The orthogonalized linear combination of atomic orbitals method (OLCAO), derived originally by Ching and Lin [33] and later expanded upon by others [34], is based upon the older LCAO method. The two methods are very similar, except that the OLCAO method treats core states differently.

The OLCAO method uses a basis of atomic orbitals to form the one-electron wavefunctions that describe the electronic states within the crystal. Although the final electron wavefunctions may be very atomic-like, they will not be purely atomic because of the bonding between atoms and the non-spherical symmetry within a crystal. The OLCAO method requires that one understand how orbitals centered on neighboring atoms interact and overlap. In general, the Hamiltonian (Equation 4.19) and overlap (Equation 4.20) matrix elements are expressed as follows. The equations are expressed in Rydberg units.

$$H_{i\alpha\kappa,j\beta\kappa'}(\mathbf{k}) = \int d\mathbf{r}\chi^*_{i,\kappa,\alpha}(\mathbf{k},\mathbf{r})\hat{H}\chi_{j,\kappa',\beta}(\mathbf{k},\mathbf{r}) \tag{4.19}$$

$$S_{i\kappa\alpha,j\kappa'\beta}(\mathbf{k}) = \int d\mathbf{r}\chi^*_{i,\kappa,\alpha}(\mathbf{k},\mathbf{r})\chi_{j,\kappa',\beta}(\mathbf{k},\mathbf{r}) \tag{4.20}$$

where $\chi^*_{i,\kappa,\alpha}(\mathbf{k},\mathbf{r})$ is a Bloch sum of the localized atomic state i centered on atomic site α of element κ. The normalized dependance of the Bloch sum $\chi_i(\mathbf{r})$ on the state i is given by the following equation:

$$\chi_{i,\kappa,\alpha}(\mathbf{r}) = \sum_{\mathbf{T}} e^{i\mathbf{k}\cdot\mathbf{T}} \phi_i(\mathbf{r} - [\tau_{j,\kappa} + \mathbf{T}]) \tag{4.21}$$

Thus, the Hamiltonian and overlap integrals are defined with respect to a basis consisting of atomic orbitals. The Hamiltonian and overlap integrals can be written in terms of a secular equation, which is shown below in Equation 4.22. The solution of this secular equation produces energy eigenvalues ϵ which are solutions to the Schrödinger equation using the wavefunctions built from the Bloch basis functions shown in Equations 4.19 and 4.20.

$$|H_{i\alpha\kappa,j\beta\kappa'} - \epsilon S_{i\alpha\kappa,j\beta\kappa'}| = 0 \tag{4.22}$$

The Hamiltonian operator $\hat{H}$ is divided into kinetic and potential terms:

$$\hat{H} = \frac{1}{2}\nabla^2 + \sum_{T\kappa j} V^{\kappa}\left[|\mathbf{r} - (\tau_{j,\kappa} + \mathbf{T})|\right] \tag{4.23}$$

where V^{κ} is the potential on the atom centered at $\tau_{j,\kappa}$ in the primitive unit cell. T is simply the vector between translationally invariant unit cells.

The use of atomic-like orbitals as the basis means that the basis functions have distinct *centers*, which are the atoms from where the radial components of the wavefunctions radiate. Thus, the overlap matrix elements are defined as either one-center or two-center integrals, depending on whether or not the χ^* and χ functions in Equation 4.20 originate from the same atom. The Hamiltonian matrix elements are more complicated, as there can be one-, two-, or three-center integrals, because there are three parts of the equation that are functions of spatial coordinates: the χ^* function, the χ function, and the potential V^{κ}. As stated earlier, the direct Coulomb electron-electron interaction is one of the two-center integrals that needs to be calculated, whereas the kinetic energy is a one-center integral.

The OLCAO method is fully *ab initio*, which means that a program that uses the OLCAO formalism requires only the configuration of the crystal as input. There are no other parameters for the user to adjust. The OLCAO method solves the full Kohn-Sham equations. The OLCAO Hamiltonian therefore has an exchange-correlation functional. Combining Equation 4.8, the Kohn-Sham exchange-correlation potential, and Equation 4.15, one obtains a formula for the exchange-correlation potential as a function of the exchange-correlation energy density.

$$V_{xc} = \frac{d[n(\mathbf{r})\epsilon_{xc}([n],\mathbf{r})]}{dn(\mathbf{r})} \tag{4.24}$$

where, as before, $\epsilon_{xc} = \epsilon_x + \epsilon_c$. The specific form that it uses for the correlation part is the Wigner interpolation formula, originally formulated by E. Wigner as a way to bridge the gap between the correlation energies of the low and high density limits of the free electron gas [35, 36]. His interpolation formula for the correlation energy density is given below:

$$\epsilon_c = \frac{-0.88}{r_s} + 7.8 \tag{4.25}$$

where r_s is defined as the radius of a sphere in which it is expected to find only one electron, when the crystal is in the ground state. The exchange part of the exchange-correlation energy density, ϵ_x, is determined by the Gáspár-Kohn-Sham exchange potential:

$$V_{GKS}(\mathbf{r}) = \frac{d[n(\mathbf{r})\epsilon_x([n],\mathbf{r})]}{dn(\mathbf{r})} = -2\left[\frac{3n(\mathbf{r})}{\pi}\right]^{1/3} \tag{4.26}$$

One may rewrite the exchange-correlation potential V_{xc} in the form of Equation 4.27, in which the term $\beta(r_s)$ contains the correlation potential [37]:

$$V_{xc} = \beta(r_s)V_{GKS}(\mathbf{r}) \tag{4.27}$$

The Wigner interpolation formula is used for the correlation energy density in the OLCAO Kohn-Sham Hamiltonian [38], so $\beta(r_s)$ is calculated as follows [37].

$$\beta_W(r_s) = 1 + \frac{0.9604r_s(r_s + 5.85)}{(r_s + 7.8)^2} \tag{4.28}$$

where the W subscript identifies the correlation potential as the Wigner interpolation formula.

The density used to calculate r_s in the Wigner correlation potential, and the density that is used by the Gáspár-Kohn-Sham exchange potential, is the same density calculated by the Kohn-Sham equations. Although the Kohn-Sham equations calculate an electron charge density for the crystal in question, both the exchange and correlation potentials assume that charge density of the crystal has the same properties as a free electron gas of the same density.

The Bloch wavefunctions that represent the quantum states of the crystal are constructed of atomic-like wavefunctions. The separable radial parts of the atomic wavefunctions, in turn, are represented as linear combinations of Gaussians multiplied by polynomials. The use of Gaussians to represent the radial wavefunctions is motivated simply by the need for computational efficiency. Gaussians and polynomials are highly analytical, in the sense that the product of two Gaussians is simply another Gaussian, and the product of two polynomials is also another polynomial. Because of this property, most integrals involving expansions of Gaussians and/or polynomials can be handled analytically. This greatly reduces the computation power needed. Some of the benefit of using Gaussians is lost when calculating the Hamiltonian matrix elements, however. The exchange-correlation functional in particular is a non-linear functional of the density, and cannot be easily represented as a finite sum of Gaussians. This is true even if the density itself is represented as a sum of Gaussians. Nevertheless, the speed and power of using Gaussians to represent the wavefunctions involved in the other integrals necessary to solve the Kohn-Sham equations warrants their continued use.

Computation power is often a concern when performing simulations. The LCAO method especially can be very computationally expensive because of the large number of atomic-like wavefunctions that are present in the unit cell of a crystal. With the heavier elements, such as the transition metals, the number of states present on these atoms can give the Hamiltonian and overlap matrices very large dimensions. Each of these wavefunctions contributes to the band structure of the crystal, and so they must all be included. However, the core states are not as important as the valence states for describing the inter-atomic bonding within the crystal, and the temptation exists to simply exclude them. Such an action, while reducing the size of the Hamiltonian and overlap matrices, can substantially and erroneously lower the energies of all the states in the system.

The OLCAO method outlined in Ref. 33 addresses this problem by drawing a clear line between core states and valence states that are principally involved in bonding. A new set of Bloch sums are then defined, as shown in Equation 4.29. These new Bloch sums are the basis sets for the crystal.

$$\chi'^{n}_{i\alpha}(\mathbf{k},\mathbf{r}) = \chi^{n}_{i\alpha}(\mathbf{k},\mathbf{r}) + \sum_{l,\gamma} a_{i\alpha,j\gamma}\chi^{c}_{j\gamma}(\mathbf{k},\mathbf{r}) \tag{4.29}$$

where the indices i and j denote orbitals on atoms α or γ, respectively. The subscript κ has been removed, as all of the atoms in the unit cell have been assumed to be identical, without loss of generality. The superscripts n and c refer to non-core and core states, respectively. χ as before refers to a Bloch sum of the orbital i or j on the atom α or γ, as denoted by the indices. The new basis functions χ' are made orthogonal to the core level Bloch sums.

$$\langle \chi'^{n}_{i\alpha}(\mathbf{k},\mathbf{r}) | \chi^{c}_{j\gamma}(\mathbf{k},\mathbf{r}) \rangle = 0 \tag{4.30}$$

It now remains to find the find the expansion coefficients $a_{i\alpha,j\gamma}$. However, if one assumes that the overlap between core states on neighboring atoms is negligible,

$$\langle \chi^{c}_{i\alpha}(\mathbf{k},\mathbf{r}) | \chi^{c}_{j\gamma}(\mathbf{k},\mathbf{r}) \rangle = 0 \tag{4.31}$$

where $\alpha \neq \gamma$, then the expansion coefficients assume the form given below:

$$a_{i\alpha,j\gamma} = -\langle \chi^{n}_{i\alpha}(\mathbf{k},\mathbf{r}) | \chi^{c}_{j\gamma}(\mathbf{k},\mathbf{r}) \rangle = 0 \tag{4.32}$$

Thus, the expansion coefficients are simply the overlap of the non-core and core states on neighboring atoms.

As long as the assumption holds that the overlap between core states on neighboring atoms is negligible, then this method greatly reduces the size of the Hamiltonian and overlap matrices. This is because the new non-core basis functions are identically orthogonal to the core states, and so they can be completely removed from the matrices. Of course, the new primed basis functions χ' produce Hamiltonian matrix elements $H'_{i\alpha,j\gamma}$ and overlap matrix elements $S'_{i\alpha,j\gamma}$. These are related to the unprimed elements via Equation 4.29.

The OLCAO method provides a much more computationally efficient algorithm than the LCAO method, although the physics behind both techniques remains very similar. The efficiency boost with the OLCAO method comes with the type of calculation required. The LCAO method requires a rigorous calculation involving all atomic states; many of these calculations are integrals that require numerical solutions, such as the exchange-correlation contribution to the Hamiltonian matrix elements. The OLCAO method requires some matrix manipulation, but these calculations are simple because the basis functions in Equation 4.32 are linear combinations of Gaussians and possibly polynomials. As stated before, any integration that involves only Gaussians and polynomials can be done analytically. Such integrations are quickly and easily accomplished. The advantage of using OLCAO over LCAO is that the program must do more analytical overlap integrals in order to transform the basis sets, but in exchange fewer numerical integrals must be done to calculate the Hamiltonian matrix elements.

The fault with OLCAO comes with the necessary assumption that the core states on neighboring atoms do not interact. If this assumption is invalid such that Equation 4.31 fails to hold true, then Equation 4.32 is incorrect. Thus, the success or failure of an OLCAO method calculation depends upon whether or not the user has correctly defined a state as ‘core’ or ‘non-core’. For the light elements, the difference between core and non-core states is clear, but for heavy elements, distinguishing the nature of the states that fall between the tightly bound core electrons ($1s$, $2sp$) and the valence shell can be difficult. If an atomic shell falls in this semi-core grey area, then there are two solutions that one may implement. Firstly, the shell can be labeled as core-level. Of course with this case, Equation 4.31 does not hold and all of the expansion coefficients $a_{i\alpha,j\gamma}$ for the non-core states must be rigorously calculated by solving a system of linear equations. The second option is that the shell is simply labeled as non-core. If this is the case, Equation 4.31 hold and the expansion coefficients can be calculated using Equation 4.32. However, as more shells are added to the non-core listing, the Hamiltonian and overlap matrices get larger, which defeats the purpose of implementing the OLCAO method. Either option will suffice to complete the calculation, and the choice is made simply to optimize efficiency.

Unless otherwise stated, much of the information and many of the equations seen in this chapter were adapted from the work of R. M. Martin [39].

Part II

Experimentation Results and Discussion

CHAPTER 5

EXPERIMENTAL RESULTS AND ANALYSIS

The spectra for $LiFePO_4$ and $FePO_4$ were measured at Beamline 8.0.1 at the Advanced Light Source, Lawrence Berkeley National Laboratory [40]. The experimental geometry is such that the spectrometer is fixed at a 90° angle with respect to the incoming radiation. The sample plate can be rotated to reach angles of incidence within the range of almost 0° to nearly 90°. This is very important for studies of single crystals, as the energy required to excite an electron will depend upon which symmetry axis is parallel to the momentum vector of the incident photon. However, $LiFePO_4$ and $FePO_4$ are powders. Thus, the plate is simply rotated to optimize the amount of flux entering the spectrometer.

The resolution of the incident x-rays is controlled by the monochromator slits; they were set to have a resolving power $E/\Delta E \approx 4000$ while measuring the XAS spectra. However, the slits had to be opened for the RIXS experiment, such that the resolution of the monochromator was reduced to $E/\Delta E \approx 700$. This was done to increase the flux impinging on the sample. As explained in Chapter 3, the probability of a radiative decay occurring to refill the core hole is very small compared to that of the competing Auger decay process. Therefore, more incident radiation flux must be allowed to pass through the monochromator to produce many more core holes so that one may see a sufficiently high signal-to-noise ratio from the emitted photons. The resolution of the emitted x-rays is controlled by the spectrometer, which has a resolving power $E/\Delta E \approx 500$ for this experiment.

The Fe $L_{2,3}$ XAS spectra for $LiFePO_4$ and $FePO_4$ are displayed on the top portions of Figure 5.1(a) and Figure 5.1(b), respectively. They have been normalized to the incident photon flux, I_0, as described in the X-ray Absorption Spectroscopy section.

The RIXS spectra for the samples, measured while exciting through the entire Fe $L_{2,3}$ threshold, are displayed on the larger bottom portions of the same figures. Each RIXS spectrum is labeled with its excitation energy. Also, the positions of the excitation energies are displayed as arrows in the top portions of the Figure where the XAS spectra are displayed, so that one may see where the excitation energies fall with respect to the $L_{2,3}$ XAS spectra. The two figures also display non-resonant XES spectra, which are the 731.9 eV and 728.4 eV spectra in the $LiFePO_4$ and $FePO_4$ panels, respectively. All XES and XAS spectra have been calibrated with respect to characteristic emission and absorption energies of the metallic Fe reference sample used in Ref. 41.

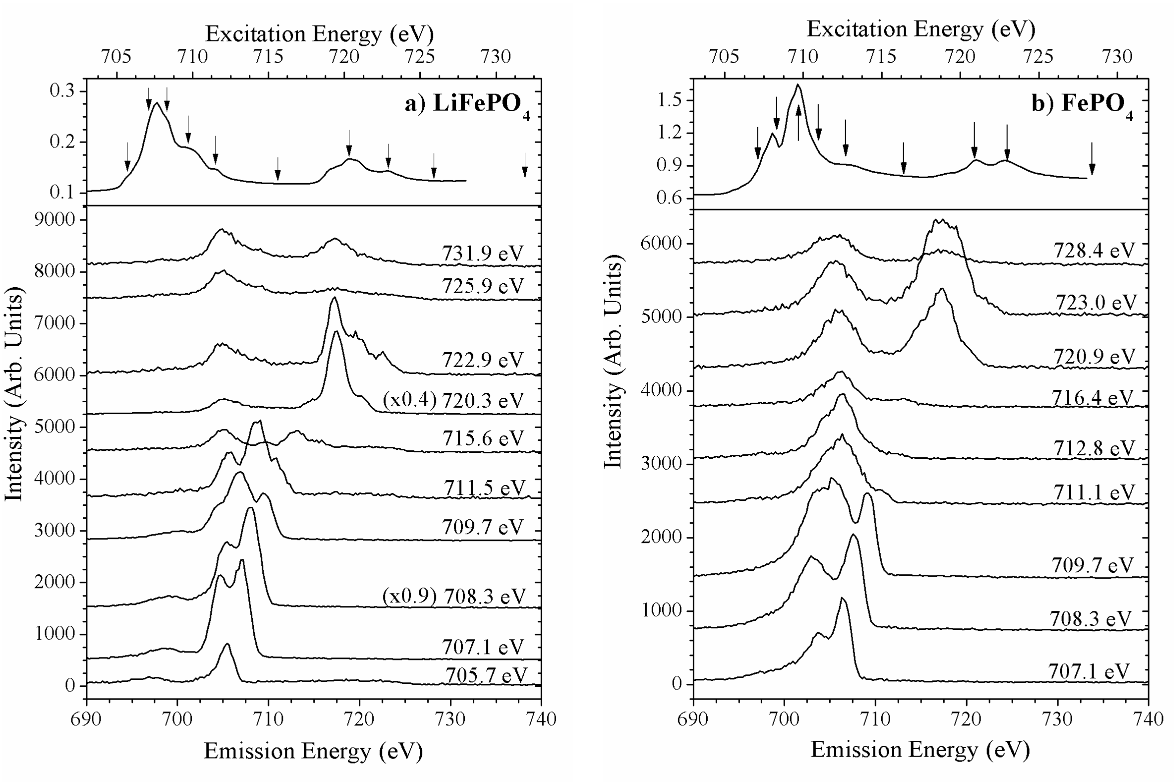

Figure 5.1: XAS and RIXS data measured from (a) $LiFePO_4$ and (b) $FePO_4$ displayed on the emission energy axis. Each RIXS spectrum is labeled with its excitation energy. The XAS spectrum for each compound is accompanied by arrows; each indicates the excitation energy for a RIXS spectrum.

The emission spectra displayed in Figure 5.1 show the evolution of scattering into regular fluorescence. As explained previously, the hallmark difference between RIXS and XES spectra is that RIXS peaks track with the excitation energy, whereas XES peaks remain at a constant energy. RIXS is the process which dominates for excitation energies that are on-threshold. As can be easily seen in the $LiFePO_4$ data, the five spectra that have excitation energies near the L_3 threshold, namely the 705.7 eV, 707.1 eV, 708.3 eV, 709.7 eV, and 711.5 eV spectra, are each characterized by peaks that track with the excitation energy. However, the 715.6 eV spectrum, which is the first spectrum to be measured off the L_3 threshold, is also the first spectrum to show the peak at about 705 eV. This feature remains a constant in all spectra measured at higher energies. This peak represents the refilling of the $2p_{3/2}$ core hole with an electron from the occupied $3d$ band through the non-resonant XES process. There is a similar trend in the $FePO_4$ spectra, however, the transition from scattering to fluorescence can be first seen in the 711.1 eV spectrum. This transition is much closer, energetically speaking, to the L_3 edge for $FePO_4$ than for $LiFePO_4$.

5.1 Voigt Function Fitting

The purpose of this study of $LiFePO_4$ and $FePO_4$ is to understand the electronic structures of the compounds and to determine which of the several theoretical models presented in the literature best describes each of them. The technique that would best provide the desired information is resonant inelastic x-ray scattering. Recall from the discussion in the Experimentation Techniques chapter that inelastic scattering peaks give unique insight into the electronic structure of a compound because the characteristic energy loss of a given scattering peak represents the energy separation of the maxima in the occupied and unoccupied states involved in the net transition. With this understanding in mind, the structure in RIXS spectra can be directly compared to theoretical density of states (DOS) calculations without simulating the full RIXS lineshape. Another benefit of RIXS is that there is no core hole. Although one excites the atomic site at a core threshold, RIXS is a one-step process that involves the valence and conduction bands. This property is a big advantage, as it provides the desired chemical selectivity but with no overlap of the core and valence states that is typical for core-level excitations involving the *d*-shell. Thus, the ground state DOS remains a valid description of the Fe site throughout the RIXS excitation event.

For transition metals, RIXS is a powerful technique for studying the electronic structure of a compound, as it allows one to directly probe the structure of the valence and conduction band DOS. However, gleaning specific information directly from RIXS spectra can be difficult because of the low resolving power of spectrometers such as the one found on Beamline 8.0.1. With a resolving power of $\mathrm{E}/\Delta\mathrm{E} \approx 500$, the spectrometer can only reliably resolve features that are greater than 1.3 eV apart for photons in the energy range around 710 eV. This resolution is insufficient to properly compare experimental spectra to the DOS presented in the literature, as low intensity features will simply be subsumed by their more intense neighbors, thereby eliminating the necessary level of detail.

This problem can be overcome to a certain extent by fitting Voigt functions to the experimental spectra. This analysis technique has not been done previously with RIXS spectra because of the inherently low flux typically associated with RIXS experiments. The low signal-to-noise ratio typically makes finding an unambiguous, reproducible fit difficult. During this type of analysis, a linear combination of Voigt function is used to simulate the experimental spectrum; each Voigt function represents an inelastic scattering transition at a certain energy. Voigt peak fitting allows for the identification of all constituent energy loss features that overlap to form the measured RIXS spectrum. Voigt peaks were chosen because a Voigt function is the convolution of a Gaussian peak and a Lorentzian peak. The mathematical form of the normalized Voigt profile is described as follows:

$$V(x;\sigma,\gamma) = \int_{-\infty}^{\infty} G(x';\sigma)L(x-x';\gamma)dx', \tag{5.1}$$

where

$$G(x;\sigma) = \frac{1}{\sigma\sqrt{2\pi}} exp\left(\frac{-(x-x_0)^2}{2\sigma^2}\right) \tag{5.2}$$

$$L(x;\gamma) = \frac{\gamma}{\pi\left[(x-x_0)^2+\gamma^2\right]} \tag{5.3}$$

$G(x;\sigma)$ is the Gaussian component with full width at half maximum (FWHM) = 2.354σ, and $L(x;\gamma)$ is the Lorentzian component with FWHM = 2γ. The function is centered at x_0. The Gaussian part of the Voigt function represents any broadening due to instrumental effects, while the Lorentzian part will simulate any broadening due to lifetime effects inherent to the system under study. The spectra chosen for the Voigt function fitting were excited near the L_3 edge; these spectra were the 705.7 eV, 707.1 eV, 708.3 eV, 709.7 eV, and 711.5 eV for $LiFePO_4$ and 707.1 eV, 708.3 eV, and 709.7 eV for $FePO_4$. This edge is preferable for fluorescence experiments because non-radiative decay processes, such as Coster-Kronig transitions, are not as significant when exciting on the L_3 edge as when exciting on the L_2 edge [42]. Before Voigt functions were fit to the RIXS spectra, all were smoothed using a second-order Savitsky-Golay function to suppress noise. The experimental spectra are displayed in Figure 5.2 before any manipulation, other than to subtract the excitation energy. Figure 5.2(a) shows the $LiFePO_4$ spectra, whereas Figure 5.2(b) shows those spectra from $FePO_4$.

The Savitsky-Golay method for suppressing noise involves fitting by least squares regression of a small subset of data to a polynomial of order n. The Savitsky-Golay method is implemented by running a 'window' of $2m+1$ points over the data, where the point in the center of the window is found after fitting the polynomial to the data within the window. In other words, after a polynomial is fit to the data using least squares regression, the central data point is fit to the polynomial. In this sense, the Savitsky-Golay method is no different from other polynomial regression algorithms, however the Savitsky-Golay approach allows for much less laborious calculation by the way that Savitsky and Golay ordered the data set [43]. This noise suppression method was chosen over others methods because it preserves peak information much better than, for example, a moving average smoothing function. A moving average smoothing method simply sets the central data point to the average calculated using the points within the window. Such a method is superior to the Savitsky-Golay smoothing method for noise suppression in low signal-to-noise ratio situations, but inferior for preserving real peak information, such as peak height and width. This difference in performance between a moving average noise filter and a Savitsky-Golay filter becomes more apparent when the peaks within a spectrum are very sharp. In the case of this analysis, it was more important to preserve spectral features than suppress noise completely.

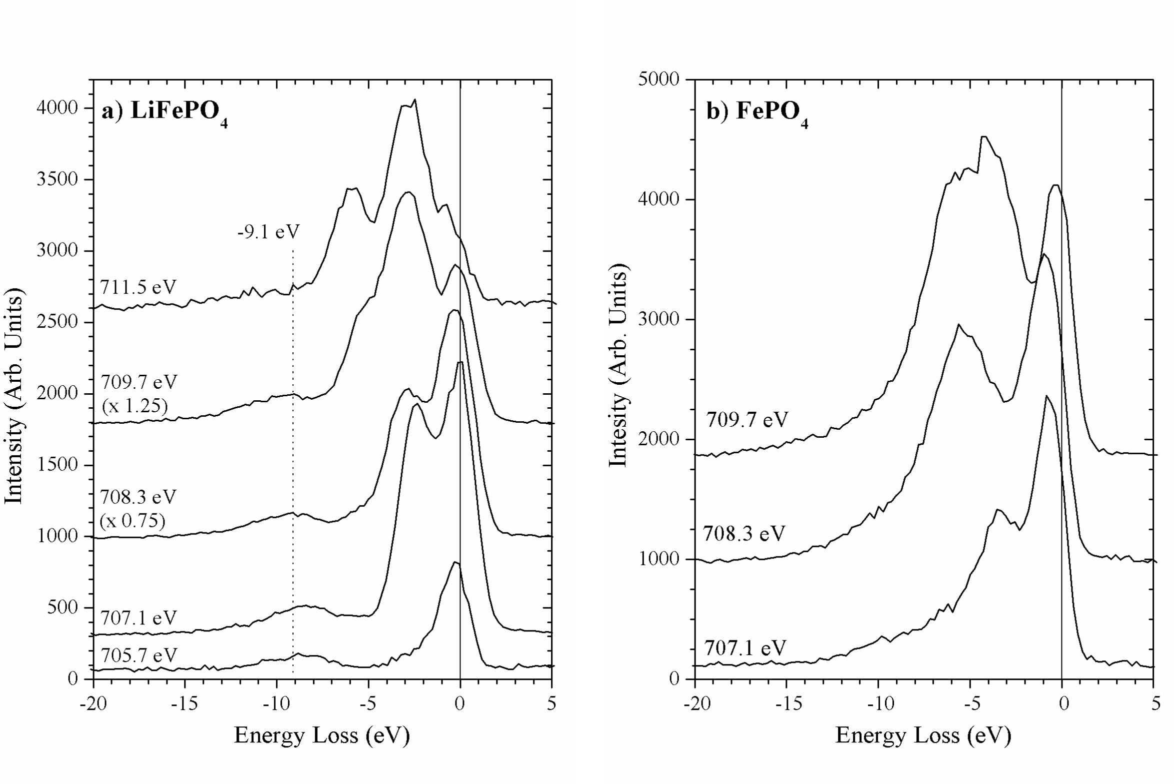

Figure 5.2: RIXS spectra on the energy loss scale for a) $LiFePO_4$ and b) $FePO_4$. The solid line represents the excitation (elastic) energy. In a), the dotted line labeled -9.1 eV is the approximate center of a broad inelastic feature common to all $LiFePO_4$ spectra.

The RIXS spectra displayed in Figure 5.2 are displayed on the energy loss scale. The translation between the emission energy scale shown in Figure 5.1 and the energy loss scale is accomplished by subtracting the excitation energy from the energy scale. This will put the elastic peak at 0 eV, and and all inelastic features will be at negative energies. The spectra were shifted to the energy loss scale because it allows one to see those spectral features that remain at a fixed energy distance from the elastic peak. Recall from the comparison of RIXS and XES in Chapter 3 that inelastic scattering features are characterized by the energy of the net transition. This net transition allows one to glean information about the valence and conduction bands.

The Voigt function fitting analysis was performed using the following hierarchy of four criteria. Firstly, the fitted curve must reproduce the experimental curve as closely as possible. This must be verified mathematically by minimizing the χ^2-value, which represents how much the experimental spectrum differs from the fit. However, interpreting the minimized χ^2-value is not a simple task, as this number takes into account the number of degrees of freedom available during the fitting process. A fit that utilizes only three Voigt functions as its basis set may have a lower χ^2-value than a fit that uses six Voigt functions, even though the second fit more accurately reproduces the features of the experimental spectrum. Thus, the quality of a fit must be verified visually. This is accomplished by inspecting the curves to see how well the sum of Voigt functions reproduces the structure of the experimental spectrum.

Secondly, all Voigt functions used in the fit must maintain a reasonable FWHM with respect to the other peaks in the fit and the experimental spectrum. This is especially necessary for the Gaussian component of the Voigt functions, because the Gaussian component represents instrumental broadening. Since the same instrument was used to record all spectra, with no changes to the resolving power of either the monochromator or the spectrometer, the instrumental broadening should in principle be constant for all Voigt functions in the fit. This criterion is necessary to represent the physics of the instrumentation, but it is also meant to prevent the addition of extremely narrow or wide peaks that may be mathematically beneficial in reducing the χ^2-value of the fit, but are physically unreasonable.

Thirdly, the fit must be reproducible within a certain error. Each time the fitting program is given the same number of peaks with roughly the same centers and FWHM values as inputs, the program should produce the same fit, regardless of the quality of the fit. If this is not the case, there are too many degrees of freedom available to the fitting program. In other words, the amount of information available to the fitting routine is redundant, and the experimental spectrum is over-represented by the number and/or position of Voigt peaks.

Lastly, there is the constraint that, if possible, the Gaussian peaks that constitute a given fit should appear in the fits of adjacent spectra. This last criterion is based in the idea that the Voigt functions represent real inelastic transitions. It stands to reason that the same transition will appear in multiple spectra, although the peak intensity will change depending on the proximity of the excitation energy to the resonant energy of that excitation path. This rule is not set in stone, of course. The $LiFePO_4$ fits, for example, show an inelastic scattering event of -2.4 eV energy loss in the 707.1 eV spectrum only. Whether one sees the same scattering event in multiple spectra is strongly affected by many properties, including the lifetime of the intermediate state. A small FWHM (long lifetime) of the intermediate state means that there is a limited range of excitation energies over which the atom may be efficiently excited through the transition in question. If one has to choose between different fits to describe a given experimental spectrum, it is preferable to choose the fit which has some similar peaks to those of its neighboring spectra.

The process to find the proper fit for a RIXS spectrum amounts to a delicate balancing act between different priorities. The fitting process for $LiFePO_4$ was relatively simple because the spectra are not as complicated. However, $FePO_4$ was another matter entirely. The fits that were eventually chosen for the 707.1 eV, 708.3 eV, and the 709.7 eV spectra are not the only ones that can reproduce the experimental spectra as accurately as is seen in Figure 5.3. However, the fits that are displayed are the only fits that satisfy all criteria, especially the second and fourth criteria, simultaneously. The Voigt function fits shown in Figure 5.3 are unique, in as much as they are the only fits to reproduce the spectra and fulfill all of the criteria.

Finding the perfect fit for a RIXS spectrum is not as simple as finding the optimal χ^2-value.

The results of the Voigt function fits are displayed in Figure 5.3 and Tables 5.1 and 5.2. Figure 5.3(a) and Table 5.1 pertain to $LiFePO_4$, and Figure 5.3(b) and Table 5.2 concern $FePO_4$. In Figure 5.3, each frame in the figure displays the smoothed experimental spectrum of interest (dotted line), the final fit (solid line), the individual Voigt peaks that constitute the fit, and a difference line that quantifies the difference between the smoothed experimental spectrum and the fit. The difference line is the thicker, dark line displayed at the bottom of each frame. Tables 5.1 and 5.2 give more precise data for every peak in each fit for $LiFePO_4$ and $FePO_4$, respectively. In the Tables, the center, the total area, and the Lorentzian, Gaussian, and total FWHM are displayed for each peak in a given fit. The total FWHM is simply the FWHM of the peak that is the superposition of the Lorentzian and Gaussian components.

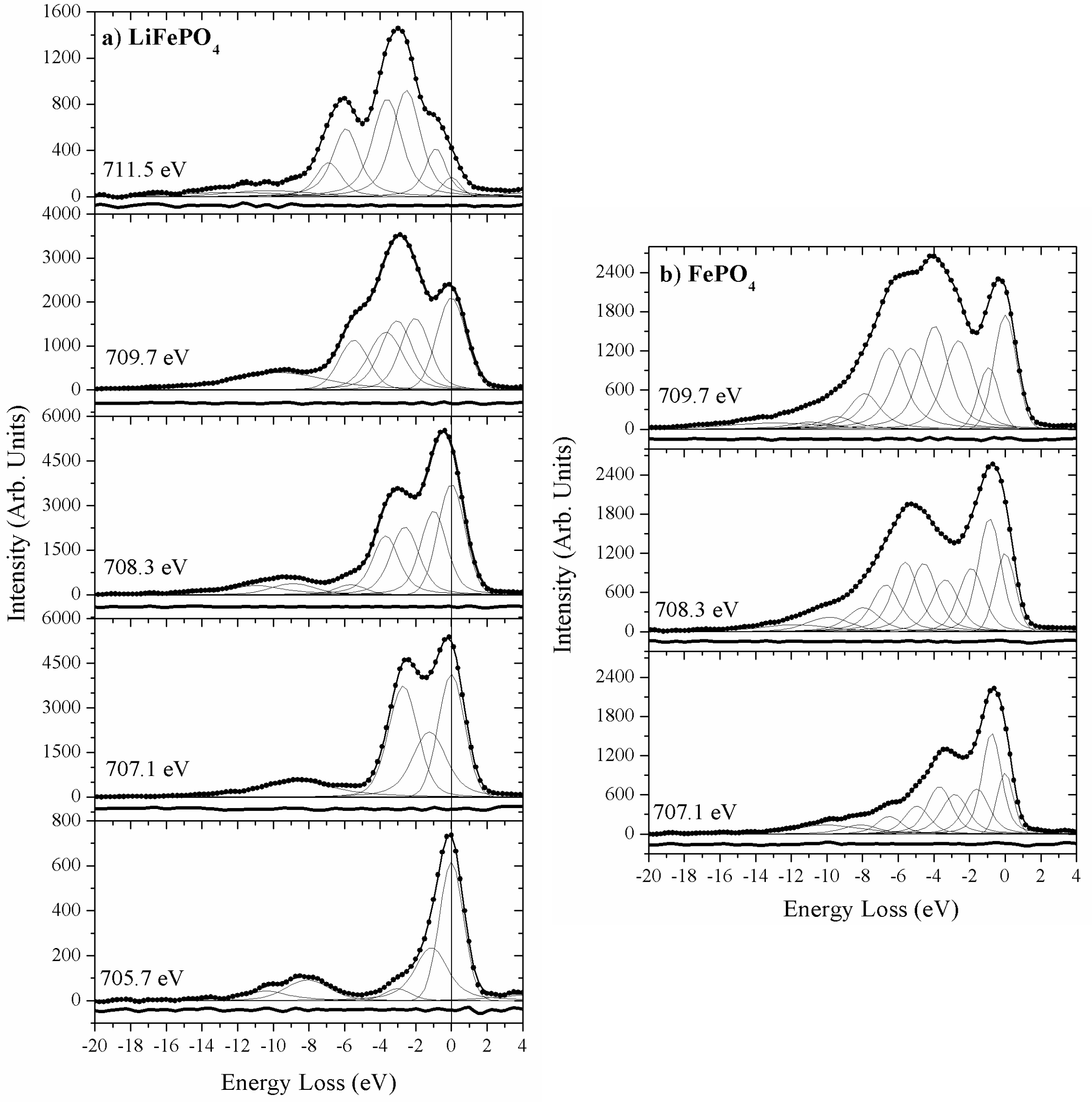

Figure 5.3: Peak fitting analysis results for each of the seven selected spectra from (a) $LiFePO_4$ and (b) $FePO_4$. In each of the panels, the smoothed experimental spectrum is represented by the scatter plot, shown by the dots. Each experimental spectrum is simulated by a sum of Voigt functions; the sum is shown by the dark black line running nearly through each of the dots. The Voigt functions that add together to make the simulated line are the lighter curves beneath the experimental spectra. Finally, the very dark line at the bottom of each panel is a difference between the fitted and measured lines.

Table 5.1: Peak data for $LiFePO_4$

Peak data: 711.5 eV spectrum

Peak No.	Peak Center	Total FWHM	Gaussian FWHM	Lorentzian FWHM	Integrated Area
1	-12.20	7.00	7.00	0.00	278
2	-10.24	5.64	5.64	0.00	315
3	-6.89	1.68	1.14	0.88	656
4	-5.92	1.78	1.01	1.18	1459
5	-3.61	1.93	1.24	1.11	2188
6	-2.52	1.87	1.22	1.04	2294
7	-0.88	1.40	0.82	0.90	806
8	0.00	1.20	1.20	0.00	213
9	7.45	7.67	7.67	0.00	483

Peak data: 709.7 eV spectrum

Peak No.	Peak Center	Total FWHM	Gaussian FWHM	Lorentzian FWHM	Integrated Area
1	-9.62	6.16	3.67	3.87	3315
2	-5.47	1.98	1.77	0.38	2579
3	-3.68	2.31	1.85	0.79	3704
4	-3.07	2.13	1.59	0.90	4229
5	-2.03	1.96	1.63	0.57	3806
6	0.00	1.94	1.94	0.00	4312

Peak data: 708.3 eV spectrum

Peak No.	Peak Center	Total FWHM	Gaussian FWHM	Lorentzian FWHM	Integrated Area
1	-10.96	3.94	0.33	3.91	1916
2	-8.88	2.93	2.23	1.19	1401
3	-5.67	1.99	1.64	0.62	818
4	-3.69	1.78	1.16	1.00	4713
5	-2.61	1.90	1.46	0.74	5373
6	-0.99	1.75	1.37	0.64	6072
7	0.00	1.80	1.80	0.00	7090

Peak data: 707.1 eV spectrum

Peak No.	Peak Center	Total FWHM	Gaussian FWHM	Lorentzian FWHM	Integrated Area
1	-8.64	4.91	2.37	3.70	3806
2	-2.71	1.95	1.70	0.44	8506
3	-1.23	2.26	1.59	1.10	6436
4	0.00	1.74	1.74	0.00	7650

Peak data: 705.7 eV spectrum

Peak No.	Peak Center	Total FWHM	Gaussian FWHM	Lorentzian FWHM	Integrated Area
1	-10.35	2.84	0.00	2.84	195
2	-8.07	2.91	2.46	0.80	320
3	-3.02	1.76	1.46	0.54	112
4	-1.13	2.19	1.35	1.32	701
5	0.00	1.59	1.59	0.00	1046
6	6.56	7.34	7.34	0.00	278
7	14.19	8.00	8.00	0.00	584

Table 5.2: Peak data for $FePO_4$

Peak data: 709.7 eV spectrum

Peak No.	Peak Center	Total FWHM	Gaussian FWHM	Lorentzian FWHM	Integrated Area
1	-12.89	6.71	6.71	0.00	684
2	-10.90	2.96	0.00	2.96	508
3	-9.47	2.25	0.00	2.25	682
4	-7.89	2.10	1.18	1.40	1590
5	-6.50	2.08	1.18	1.38	3587
6	-5.29	2.25	1.45	1.28	3737
7	-3.96	1.91	1.14	1.20	4126
8	-2.61	2.00	1.55	0.76	3370
9	-0.93	1.35	1.34	0.02	1366
10	0.00	1.49	1.49	0.00	2771

Peak data: 708.3 eV spectrum

Peak No.	Peak Center	Total FWHM	Gaussian FWHM	Lorentzian FWHM	Integrated Area
1	-11.84	4.68	3.36	2.18	634
2	-9.90	2.90	2.38	0.90	770
3	-7.97	2.15	1.37	1.23	1064
4	-6.70	1.87	1.19	1.09	1799
5	-5.61	1.72	1.07	1.03	2490
6	-4.57	1.77	1.20	0.93	2438
7	-3.35	1.80	1.33	0.79	1814
8	-1.90	1.67	1.37	0.52	1954
9	-0.88	1.51	1.26	0.45	3150
10	0.00	1.32	1.32	0.00	1681

Peak data: 707.1 eV spectrum

Peak No.	Peak Center	Total FWHM	Gaussian FWHM	Lorentzian FWHM	Integrated Area
1	-9.99	4.59	0.00	4.59	1004
2	-8.12	2.34	1.20	1.70	471
3	-6.50	1.63	1.16	0.79	572
4	-4.95	1.64	1.23	0.70	890
5	-3.69	1.64	1.17	0.77	1537
6	-2.83	1.76	1.19	0.93	1411
7	-1.60	1.66	1.24	0.71	1450
8	-0.76	1.30	1.01	0.50	2496
9	0.00	1.09	1.09	0.00	1077

Recall that one of the guiding criteria used in the creation of the displayed Voigt function fits is that the Gaussian FWHM of each peak should be equal to all other peaks within the fit. In the so-called central region, i.e. that region less than 7.0-8.0 eV below the elastic peak for $LiFePO_4$ and $FePO_4$, this criterion was achieved. Considering the 707.1 eV, 708.3 eV, and 709.7 eV spectra for $LiFePO_4$, the central region had an average Gaussian FWHM of 1.63 eV, with a standard deviation of 0.21 eV. For $FePO_4$, the average was 1.25 eV with a standard deviation of 0.14 eV. However, outside of the central region, the Voigt functions do not exhibit such well-ordered behavior. These Voigt functions include those that are used to describe the broad, high-energy loss features in $LiFePO_4$ and $FePO_4$. The Gaussian FWHM of these features were inconsistently reported among fitting results, which is attributed to the fact that the statistics in the region of -15.0 eV to -8.0 eV loss are too poor for reproducible results to be achieved.

There are also peaks on the positive side of the elastic peak in the 711.5 eV and 705.7 eV $LiFePO_4$ spectra. Information about these peaks is shown in Table 5.1 for completeness, but the peaks are not displayed in Figure 5.3(a) because they are not relevant to the discussion of the RIXS features in $LiFePO_4$. These are not real inelastic features due to light scattering from $LiFePO_4$. It is likely that these features are the result of a systematic, instrumentation effect, a problem that is eliminated in the 707.1 eV, 708.3 eV and 709.7 eV spectra because they were measured at a different time, and they were measured over a longer time interval. These three spectra exhibit better statistics and do not show any sign of these positive side peaks. The unknown contribution of this instrumentation effect is the reason why the FWHM of the Voigt functions from the 711.5 eV and 705.7 eV spectra are not included in the FWHM average for $LiFePO_4$.

With the exception of the elastic peaks, the Lorentzian FWHM was not nearly so consistent among the well-defined central region peaks for both materials. Not including the elastic peaks, the Voigt functions for $LiFePO_4$ showed a mean Lorentzian width of 0.72 eV, with a standard deviation of 0.23 eV; for $FePO_4$, the mean was 0.91 eV with a standard deviation of 0.39 eV. However, consistency of width for the Lorentzian component for energy loss peaks is not nearly so strict a guideline as for Gaussian broadening. Whereas Gaussian broadening defines the systematic instrumental effects, which should be identical for all inelastic scattering events, the Lorentzian component describes the lifetime broadening. This property may vary considerably from peak to peak depending on the stability of the virtual intermediate and final states that make up the net transition. In sharp contrast to the inelastic features, the Lorentzian broadening of every elastic peak was non-existent for both materials. This is to be expected; a large part of the elastic peaks is simply reflected radiation, which has no lifetime broadening.

Experiment and theory are compared in Figure 5.4. Figure 5.4(a) and 5.4(b) display the calculated ferromagnetic Fe spin-polarized partial density of states (PDOS) for $LiFePO_4$ and $FePO_4$. Spin-polarized DOS are displayed as a function of electron spin; the DOS for spin-down electrons is displayed pointing down from the line at O 1/eV. The spin-down DOS, conversely, points up from the O 1/eV line. The Figure displays several arrows; these represent $3d$ inner-shell electronic transitions. During a transition, an electron is scattered from the states indicated by the left arrowhead to the states represented by the right arrowhead. The arrow lengths are the energy values of the centers of the peaks that constitute the Voigt function simulations shown in Figure 5.3.

Note that each arrow only denotes a possible transition with the corresponding energy loss. In some cases, such as the 3.0 eV energy loss feature, there are four possible combinations of initial and final states that can occur, and any or all of the displayed transitions can contribute to the peak measured in the experimental RIXS spectrum. Information concerning the relative weighting of the transitions with the same energy loss cannot be obtained using this method.

The analysis clearly shows that the calculated density of states has accurately predicted the relative energy positions of the occupied and unoccupied states. The power of the Voigt function fitting technique is shown through the discovery of the ≈-0.95 eV and ≈-1.2 eV features, which otherwise were not detectable. With a resolving power of $E/\Delta E \approx 500$, the spectrometer could only resolve peaks that were separated by energies greater than about 1.3 eV, thus the -1.2 eV and -0.95 eV energy loss features were not visually differentiable from neighboring peaks. However, the inclusion of these peaks was necessary, for both a proper simulation of the spectral lineshape and a reasonable Gaussian FWHM for the elastic peak.

Despite the limited resolving power of the spectrometer, it is nevertheless obvious that the $FePO_4$ RIXS spectra are broader than $LiFePO_4$ spectra with the same excitation energy, in the sense that the $FePO_4$ RIXS spectra are spread over a greater energy range. The greater broadness of the $FePO_4$ RIXS spectra results from the delocalization of the Fe valence electrons due to greater overlap and hybridization of the Fe 3*d* states with neighboring O 2*p* states, as Tang *et al.* first predicted [17]. The greater covalency is due to the inductive effect of the phosphorous sites as suggested by Padhi *et al.* [1], an effect in which the Fe and P sites compete with one another for the greater share of the bonding with their mutual oxygen neighbors. The stronger covalent bonding and greater mixing leads to lessened degeneracy of the Fe valence states, which separates the Fe 3*d* states. This creates more local maxima within the Fe 3*d* occupied states, which allows for many possible scattering transitions in

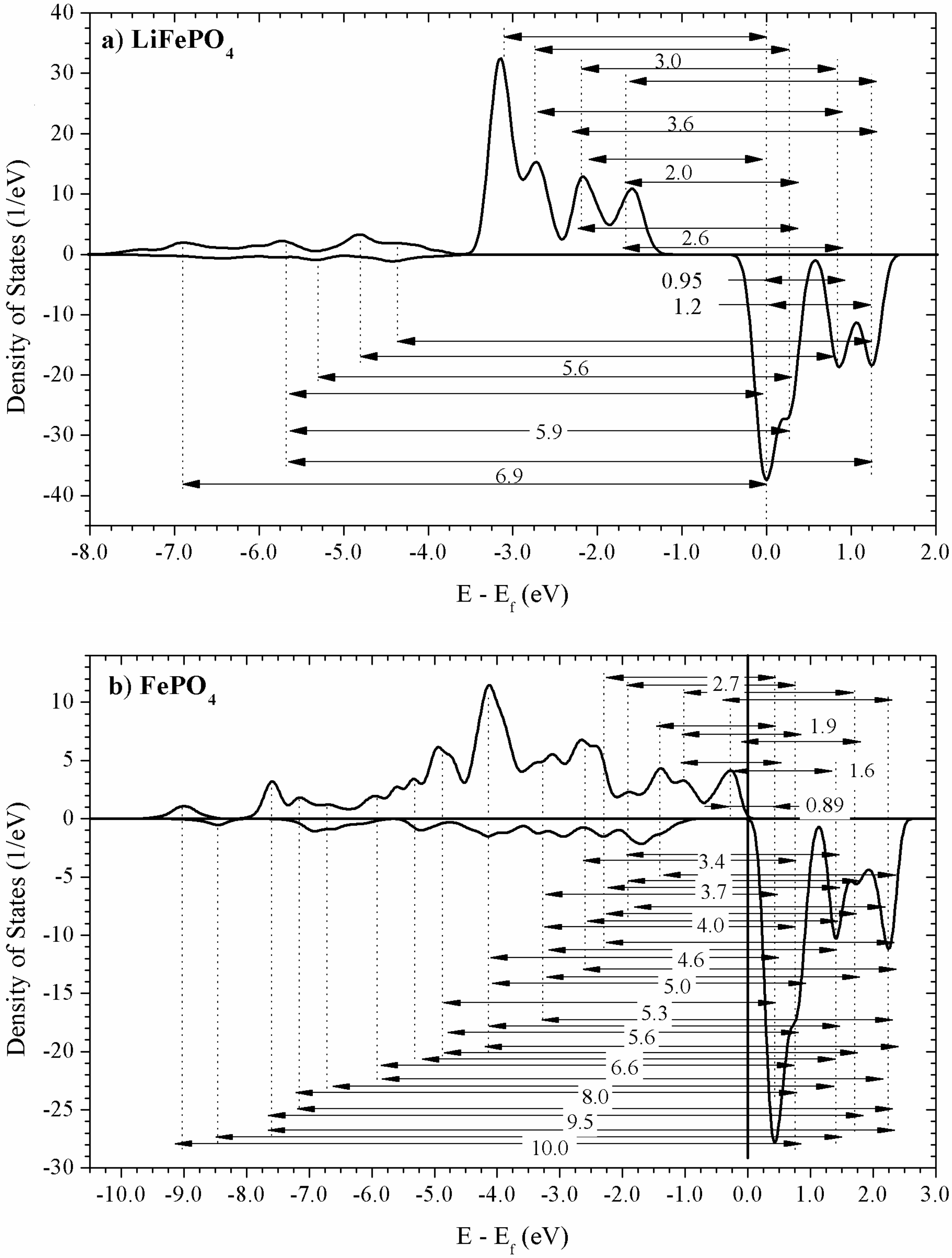

Figure 5.4: Fe 3d PDOS calculations and assignment of energy losses found during Voigt peak fitting for (a) LiFePO$_4$ and (b) FePO$_4$. Note that the DOS was broadened by 0.3 eV in both cases to make it easier to see where lie the points of greatest density.

the $FePO_4$ RIXS spectra, as is displayed by the greater number of peaks uncovered by Voigt function fitting. This rich structure, when measured with insufficient resolution, blends together to produce the broader lineshape that is characteristic of $FePO_4$.

The lessened degeneracy of the $FePO_4$ Fe PDOS is most likely the reason why the Voigt functions in the $FePO_4$ fits have smaller FWHM than their $LiFePO_4$ counterparts. Recall that the $FePO_4$ spectra had an average Gaussian FWHM of 1.25 eV, which is very close to the resolution of the spectrometer, but the $LiFePO_4$ average Gaussian FWHM was 1.63 eV. The greater energy separation of the states in the $FePO_4$ $3d$ band means that every inelastic feature in the RIXS spectra represents only one transition. However, in $LiFePO_4$, the degeneracy is greater and the states are more difficult to distinguish, meaning that each inelastic feature is the average of several transitions that are separated by less than 0.1-0.2 eV. Peaks that are separated by such a small energy value cannot be differentiated in the Voigt function fitting process, so the 'average' peak that describes the entire group has to be wider to cover all transitions. Unfortunately, at present it is impossible to differentiate these closely degenerate states from one another. A RIXS spectrometer that can resolve features that are 200 meV apart would require a resolving power somewhere between 3500 and 4000 on the Fe $L_{2,3}$ absorption threshold. There are currently no soft x-ray spectrometers that have this capability, although advances in grating manufacturing techniques and better photon sensor technology will probably change this in the near future. In particular, the spectrometer designed by Moewes and coworkers promises to show unprecedented resolution [44].

There are other transitions predicted by the DOS that are not seen in any of the RIXS spectra. This is especially noticeable for $LiFePO_4$, as there are many obvious combinations of peaks in the occupied and unoccupied DOS that could give rise to new scattering events. Regardless, the displayed DOS calculations have proven to be an accurate representation of $LiFePO_4$ and $FePO_4$, in the sense that while not all predicted transitions are seen in the RIXS spectra, all experimental energy loss features can be identified in the DOS. It is likely that these other inelastic scattering events do exist, but are not sufficiently probable to be a significant part of the spectrum. At this point in the analysis of $LiFePO_4$ and $FePO_4$, the displayed RIXS results support the idea that one does not have to explicitly account for the effects of electron correlation when calculating the band structure of these materials.

5.2 Analysis

The Voigt function fitting analysis routine has given much information concerning the transitions that lay unresolved within the $LiFePO_4$ RIXS spectra. However, there are areas that need to be explored further. Firstly, there is the problem of the broad, flat feature seen at approximately -9.1 eV energy loss in all of the $LiFePO_4$ spectra. This feature was not conveniently explained by matching energy loss features to *d*-*d* transitions in Figure 5.4, and thus this feature at -9.1 eV warrants further investigation. Secondly, there is the problem of spin flipping. All of the unoccupied Fe 3*d* DOS is spin-down, whereas the vast majority of electrons in the occupied states have spins of the opposite orientation. Inner-shell scattering of 3*d* electrons therefore violates the spin selection rule, which states that $\Delta S = 0$ in all dipole-allowed transitions that obey Russells-Saunders coupling. Both of these issues will be discussed presently.

5.2.1 High Energy Loss Features

In the $LiFePO_4$ experimental spectra, there is a broad feature centered at approximately -9.1 eV energy loss, as seen in Figure 5.2(a). The center of the feature does not, in fact, remain at -9.1 eV in all of the five displayed RIXS spectra. In the 705.7 eV spectrum, this feature is jointly represented by the -10.4 eV and -8.1 eV Voigt functions. This energy loss feature is modeled by the peak at -8.6 eV in the 707.1 eV spectrum, by the peaks at -11.0 eV and -8.9 eV in the 708.3 eV spectrum, by the peak at -9.6 eV in the 709.7 eV spectrum, and finally by the peaks at -12.2 eV and -10.2 eV in the 711.5 eV spectrum. Despite its wandering center, however, the broad features at high energy loss in all of the RIXS spectra will be jointly referenced by the term '-9.1 eV feature', so as to avoid confusion. It is obvious by inspection that the feature is much wider than the other energy loss features shown in Figure 5.3(a) and grows ever wider at higher excitation energies. At 709.7 eV, the Voigt function used to model the energy loss feature has a total FWHM of 6.2 eV, which is approaching threefold that of the other peaks. This width covers most of the Fe valence band.

Inner-shell scattering transitions have the highest probability of occurring during on-threshold XES experiments in the soft x-ray energy range [29]. However, it is highly improbable that this feature is due to one $3d$ inner-shell scattering transition, because the character of this feature deviates so strongly from all the other scattering transitions. As explained earlier, the Gaussian FWHM for all features measured at the same time within the same spectrum must be reasonably close to identical, as all of the peaks are being measured by the same equipment. The -9.1 eV feature does not adhere to this constraint at all. Thus, this feature cannot simply be one peak, however it can certainly be the superposition of many less intense transitions that cannot be individually resolved. Even should all of the smaller peaks hold to the Gaussian FWHM constraint, the peak that results from their superposition need not adhere to the same constraint. At higher excitation energies, these transitions in the $LiFePO_4$ spectra become more numerous as the greater photon energy accesses a greater number of transitions, thereby increasing the overall width of the feature.

It is highly unlikely that the broad -9.1 eV feature is due to a singular $3d$-$3d$ inner-shell transition, but rather a group of tightly spaced transitions that cannot be easily resolved. There are two possibilities that are the most obvious. Either the feature is due to several $3d$ inner-shell transitions, or that the feature is due to some kind of charge transfer mechanism. Figure 5.5 shows the PDOS for the Fe, P, and O sites in $LiFePO_4$. The DOS in the figure have not been differentiated according to spin; the spin-up and spin-down DOS for all three sites have been added together to lessen the complexity of Figure 5.5. The purpose of the Figure is to show which states could possibly be involved in making the -9.1 eV feature. There are two different colors; the green box highlights the near-Fermi region that is chiefly dominated by the Fe $3d$ states. There are some contributions from O and P here, but they are insignificant in comparison. The red box, on the other hand, highlights unoccupied bands that are mostly due to p and d states originating from the ligand sites. During a transition, an electron may be scattered from the occupied states on the left of the Fermi edge to the unoccupied states to the right of the Fermi edge (indicated by 0 eV), provided that the occupied and unoccupied states are highlighted by the same color of box. So, for example, an electron may be promoted from a state in the green box on the left to the green box on the right during a RIXS event.

The sizes of the boxes were difficult to approximate, as they had to encompass the range of states that could reliably be expected to contribute to the feature. This is a difficult prospect considering that the tightly-spaced peaks cannot be resolved to provide information on where the centers of the peaks sit on the energy axis. The sizes of the boxes were estimated as follows. Assuming that the many peaks that constitute the -9.1 eV feature have similar Gaussian and Lorentzian FWHM to the rest of the peaks in the $LiFePO_4$ Voigt function fits, albeit with much smaller intensities, then there should not be a peak within $\approx$1 eV of the ends of the feature. The larger peaks within the fits do not go to zero until 2.5 - 3.0 eV away from the center, depending on the height of the peak. This particular feature of the Voigt peaks is a consequence of their Lorentzian component, which is characterized by a very sharp peak and a very long tail. Thus, for a very small peak, it seems reasonable that it would go to zero within 1 eV of the center. Judging where the -9.1 eV feature goes to zero is difficult, but inspection suggests that the peak vanishes around 6 eV away from the center. According to the argument above, all peaks must reside within a distance of 5 eV of -9.1 eV (within 1 eV of the edges), which would make the outermost transitions around -14.1 eV and -4.1 eV energy loss.

Limits on how much energy a photon may lose completing a net RIXS transition were then defined. With this information in hand, the boxes on the left side of the Fermi level were drawn according to the following guidelines. Firstly, the occupied DOS box must be centered at -9.1 eV with respect to the center of the unoccupied DOS to which electrons are scattered. The center line of a box is shown by the thick vertical line that is the same color as the box itself. Two lines of the same color must

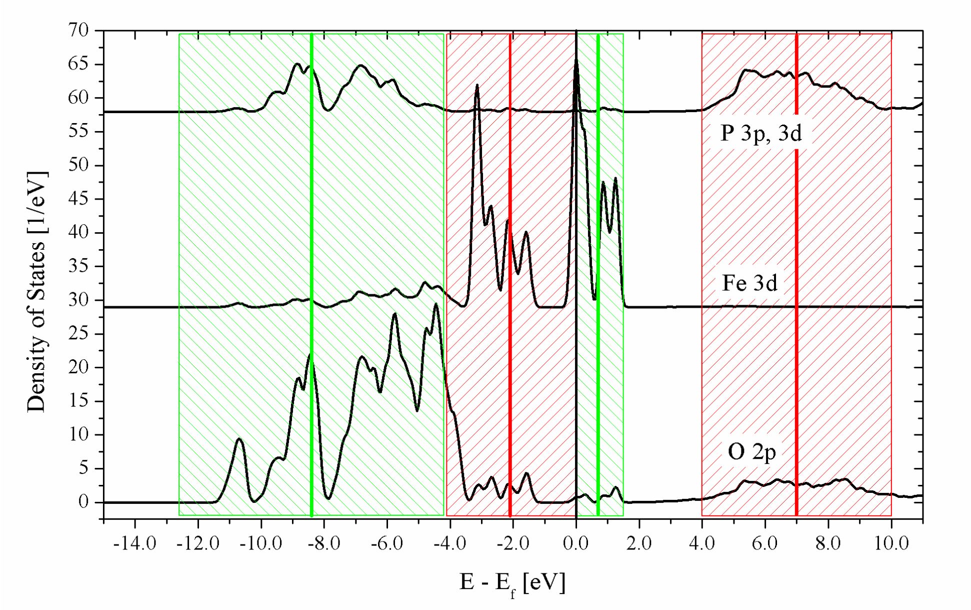

Figure 5.5: Phosphorous (top), iron (middle), and oxygen (bottom) total PDOS for $LiFePO_4$. The DOS were broadened with a Gaussian profile with FWHM of 0.2 eV simply to show structure. Groups of transitions are divided up according to color. The occupied states in the left green slashed box may scatter to the green box in the occupied states; likewise, the occupied states in the left red slashed box may scatter to the unoccupied states in the right red slashed box.

be separated by 9.1 eV. Secondly, the energy separation between the low-energy (left) side of the occupied (left) box and the high-energy (right) side of the unoccupied (right) box represents the highest possible energy loss transition, and this must be approximately 14 eV. Lastly, the energy separation between the high-energy (right) side of the occupied (left) box and the low-energy (left) side of the unoccupied (right) box represents the lowest possible energy loss transition. This is approximately 4 eV. Given that the unoccupied boxes are already defined, it is a simple matter to draw the boxes over the occupied states.

Figure 5.5 shows the range of occupied states from which electrons may scatter and the range of unoccupied states to which the electrons may scatter to make the -9.1 eV feature. There are two possibilities that are immediately obvious. The first is that the -9.1 eV feature consists of simple *d*-*d* inner-shell scattering, shown by the green boxes. Although there are multiple peaks in the area highlighted by the left green box which could generate some spectral weight around -9.1 eV loss, there is a major problem with assigning the -9.1 feature wholly to scattering from these states. There is no reason to expect that the scattering processes highlighted by the green box transitions should behave any differently than any other *d*-*d* transition seen thus far, so one should expect to see structure commensurate with the lower energy loss features. After all, the electrons in the occupied states highlighted by the left green box are scattering to the same unoccupied states as every other electron participating in a *d*-*d* scattering transition. However, the -9.1 eV feature is largely featureless (with the exception of the 705.7 eV spectrum seen in Figure 5.3), in stark contrast to the sharp features seen in the unoccupied states. It would seem that there is another process occurring at -9.1 eV energy loss that must be understood. That being said, however, there is undoubtedly some *d*-*d* scattering happening around -9.1 eV, they merely have such low intensity that they contribute no structure to the -9.1 eV feature.

The fact that the *d*-*d* transitions around -9.1 eV have such low intensity strengthens the earlier argument that the -5.6 eV, -5.9 eV, and -6.9 eV features are the result of scattering from the small spin-down occupied DOS. The aforementioned three RIXS transitions experience an increased probability to scatter because the electron requires no spin-flip, thus eliminating the need to couple to a magnon. However, the spin-up states in the vicinity of these spin-down occupied states, shown in Figure 5.3, still take part in net RIXS transitions, just at a much reduced probability, and form part of the low energy loss tail of the -9.1 eV feature. Therefore, *d*-*d* inner-shell scattering may be part of the reason for the -9.1 eV feature, but more investigation is necessary.

A commonly held practice is to assign the -9.1 eV feature as a charge transfer peak, with an electron transferring between the Fe site and one of the surrounding O sites. There are two possibilities. The first is that an electron transfers from the negatively charged anion to the cation. In the case of $LiFePO_4$, the cation is the Fe site and the anion is one of the O ligands. Proving or disproving this particular process is however beyond the scope of this thesis, as it involves a full simulation of the RIXS spectra using the Kramers-Heisenberg formula. Charge transfer cannot be accurately understood with the DFT calculations displayed earlier, as charge transfer is not a charge neutral excitation, in the sense that the charge density is changed (in principle) in the vicinity of the transfer. This alters the ground state electron charge density, upon which the DOS calculations and everything else in DFT theory are based. That being said, Augustsson *et al.* simulated to a reasonable degree of accuracy the XAS spectrum using the crystal field multiplet program of Thole, and they did not need to include charge transfer effects [45]. Their RIXS simulations were not as successful, suggested that the density of states calculated using an atomic Hamiltonian, even if it includes crystal field effects, is nevertheless insufficient for an accurate portrayal of the $LiFePO_4$ crystal. XAS spectra for transition metals are easier to calculate than RIXS spectra because the strong overlap of the core hole and valence wavefunctions changes the local charge density environment to such a degree that many subtle characteristics of the crystal are overpowered. This, of course, does not happen in the less drastic one-step RIXS process that has no core hole. It should be also noted that the experimental spectra of Augustsson *et al.* does not show the -9.1 eV feature seen in all of the $LiFePO_4$ spectra, and thus he did not present an explanation for its presence.

Although proving or disproving that the -9.1 eV feature is due to charge transfer is beyond the scope of this thesis, the argument is made here that charge transfer of the type mentioned above is not possible, due to the very nature of resonant inelastic x-ray scattering. Charge transfer satellites in RIXS spectra come about as the result of mixing of two configurations, the ground state and the configuration wherein an electron has transferred from a ligand to the metal ion. In the case of $LiFePO_4$, where the Fe site has a charge of 2+ in the ground state, the two configurations that would mix are $3d6$ and $3d7\underline{L}$, where $\underline{L}$ represents a ligand valence hole. Although this charge transfer can happen spontaneously if the energies of the configurations are within thermal energies, this is often not the case. The ground and charge transfer configurations can differ by several eV. Therefore, the charge transfer can only occur when an x-ray photon has created a core hole. Core hole-induced charge transfer is a well-documented phenomenon, especially in the rare earth oxides [46]. However, in the case of Moewes *et al.*, the charge transfer was observed in the non-resonant fluorescence spectrum. The -9.1 eV spectrum is a RIXS event. As discussed earlier, there is significant difference between RIXS and fluorescence, namely that resonantly scattered photons describe the net transition between initial and final states, whereas a fluorescence photon is simply the result of a valence electron refilling a core hole.

The probability that a RIXS event will occur is calculated using the Kramers-Heisenberg formula. In this formula, the dipole matrix elements of the excitation and relaxation paths are multiplied together, divided by a complex denominator which is responsible for the resonance effect. When simulating RIXS spectra, the matrix elements are calculated as two separate steps before they are combined in the Kramers-Heisenberg formula. Although this is how a RIXS spectrum is simulated, it can lead to some conceptual problems because it appears as if the RIXS event is the result of two separate events. This is not the case. A RIXS event is a one-step process, wherein the core hole is virtual and does not really exist for any purpose other than simulating the RIXS cross-section. Thus, any charge transfer effects in the intermediate state that require the presence of a core hole cannot occur.

Another possible charge transfer occurs when an electron skips from an Fe site to an O site, as a result of orbital hybridization. In this case, the electron follows the tendency to diffuse from highly localized to delocalized states, where the charge is spread over a greater volume. This diffusion of electron charge among hybridized orbitals is one of the ways that electrons conduct through covalently bonded materials. One of the reasons why highly correlated materials do not conduct well is that correlated materials do not hybridize strongly due to strong localization effects, and thus the isolated electrons may not move freely. This type of charge transfer requires the electron to first be excited to the hybridized unoccupied states. For the purposes of this thesis, the excitation mechanism is RIXS. Such a charge transfer mechanism would be described by either the green or the red sets of boxes, because both colors highlight O unoccupied PDOS, although there are few states under the right green box. The problem is that there are no Fe 3*d* states to speak of in the range of 4.0 to

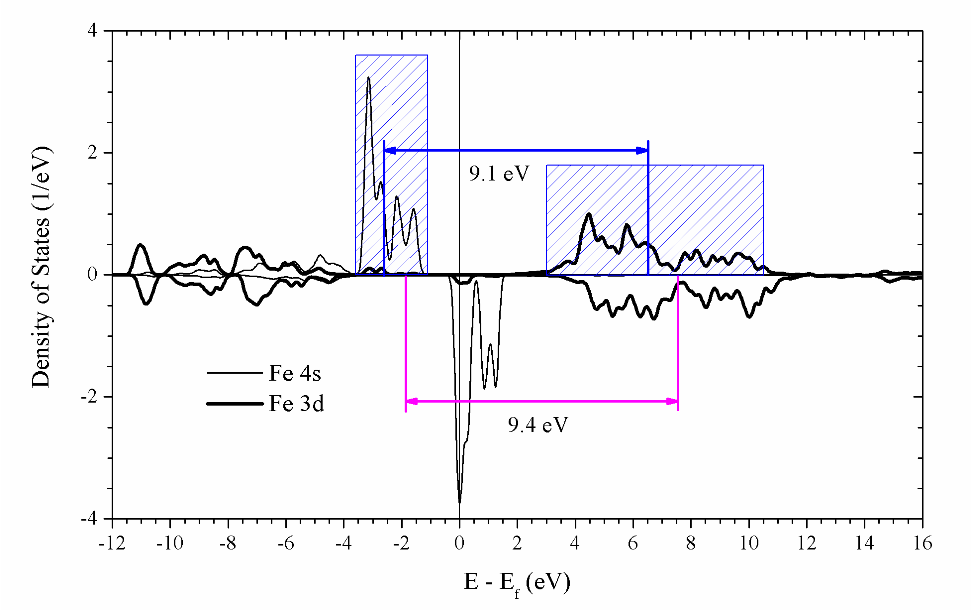

Figure 5.6: $LiFePO_4$ and $FePO_4$ Fe 3*d* and 4*s* spin-polarized PDOS. The dark lines are the 4*s* states, while the thinner lines are the 3*d* states. The 3*d* PDOS have been divided by 10 so that the structure of the 4*s* PDOS would be easier to see. There are two RIXS net transitions displayed, one for each of the spin-up and spin-down channels in $LiFePO_4$. In each case, electrons are scattered from the 3*d* occupied to the 4*s* unoccupied states with the same spin orientation, such that $\Delta S = 0$ in both cases.

10.0 eV highlighted by the right red box. There must be some Fe states hybridized with O states where the electrons can initially scatter, or there can be no charge transfer. According to the analysis shown in Figure 5.5, the near-Fermi occupied Fe states highlighted by the left red box cannot participate in the Fe-O charge transfer.

However, there is another possibility. A RIXS event is the net transition resulting from virtual core hole creation and annihilation processes, each of which is dipole-allowed. Therefore, the momentum selection rules for RIXS state that $\Delta L = 0, \pm 2$. This selection rule allows electrons from the 3*d*-shell to jump to the 4*s*-shell; for Fe^{2+}, this band is mostly empty. Figure 5.6 displays the Fe 3*d* and 4*s* PDOS. In this figure, the spin-up and spin-down states are separated for the 4*s* and 3*d* bands.

Figure 5.6 shows the theorized 3*d*-4*s* scattering event in $LiFePO_4$. As before in Figure 5.5, boxes are drawn around the states that are participating in the net scattering transition. As stated, the 3*d* and 4*s* PDOS in Figure 5.6 are separated according to spin orientation. The spin-up states will be discussed first. The left blue box, which highlights the occupied states that are participating in the -9.1 eV scattering event, was drawn first. It was drawn so that the most dense section of the $LiFePO_4$ Fe spin-up PDOS was included in the box, which seems logical as it is in this energy range that electrons will most probably be found. With the left blue box in the occupied states drawn, the limits of the right blue box must be found. As before, the right edge of the right box highlighting the unoccupied states was calculated to be 14.1 eV away from the left edge of the left box; this represents the maximum possible loss of energy observed in the $LiFePO_4$ RIXS spectra. The left edge of the right box is 4.1 eV away from the right edge of the left box; this represents the smallest possible energy loss feature that can be under the broad envelope of the -9.1 eV feature. Therefore, for the spin-up states, the right blue box covers the entire spin-up $4s$ unoccupied states, and the left blue box neatly highlights the densest part of the spin-up $3d$ states.

Thus far, the proposed $3d$-$4s$ transition in the spin-up channel describes what was seen in the experimental $LiFePO_4$ RIXS spectra. It then remained to find the center of the $3d$-$4s$ transition. To this end, the centers of gravity (or simply the centroids) of the Fe $3d$ occupied PDOS and the Fe $4s$ unoccupied PDOS were calculated. Since there are an equal number of states to either side of the centroid, the energy separating the centroids should reflect the approximate center of the transition in question as there will be an equal amount of spectral weight to either side of the center. For the spin-up states, the centroids of the $3d$ occupied and $4s$ unoccupied states highlighted by the blue boxes were calculated. These centroids are represented by the thick vertical blue lines; the energy separation is shown by the horizontal blue arrow. As it turns out, the centroids do not correspond to the geometrical centers of their respective boxes, as both centroids are shifted to deeper energies. However, the centroids are separated by -9.1 eV, exactly as shown by experiment.

A similar analysis was performed for the spin-down channel, but the results were not as encouraging. The centroids for the entire $3d$ and $4s$ spin-down bands were calculated, and they are displayed in Figure 5.6 as the magenta vertical lines. However, boxes were not drawn to highlight the states involved because the $3d$ spin-down band is so very asymmetrical. The states are divided between a sharp, very dense peak right at the Fermi level and a very broad expanse at low energies; these two areas are separated by a gulf of about 3.8 eV in which there are no states whatsoever. This division would certainly be resolved by the spectrometer, so the -9.1 eV feature would be divided into two features. Given that only one feature is seen, it would seem that the spin-up channel dominates the $3d$-$4s$ scattering channel.

This analysis method deviates from that conducted earlier. When the boxes were drawn in Figure 5.5, the center of the $3d$-$4s$ RIXS feature was assumed to be the energy separation between the geometric centers of the boxes themselves. This assumption is inaccurate, as it assumes the DOS under each of the boxes is symmetrical about the geometrical center of the box. Although inaccurate, the assumption was sufficient to discuss simply whether scattering among the states highlighted by the boxes in Figure 5.5 could explain the -9.1 eV feature seen in the experimental spectra. However, a more accurate description is necessary for the proposed $3d$-$4s$ RIXS mechanism. As it turns out, the $3d$-$4s$ RIXS transition survives the more rigorous analysis. This shows that scattering between the spin-up $3d$ and $4s$ states can easily contribute spectral weight to the -9.1 eV feature.

A scattering transition to the $4s$ states has two attractive qualities to it. Firstly, it fulfills the RIXS requirement that the angular momentum quantum number change by 2. Secondly, the $4s$ shell is a highly delocalized band that is thoroughly mixed with the high-energy unoccupied O $2p$ states. This of course allows for a charge transfer to O, in the sense that the electron is scattered to a band that has O character as well as Fe character. In fact, this characteristic of the hybridized $4s$-$2p$ unoccupied band is necessary in terms of the relative probability for excitation. As will be discussed in more depth later, the number of states at a given energy strongly affects the probability that the states at that energy will be involved in a photoexcitation process. This is intuitive; the more densely packed the states are at a given energy, the more likely an electron will be present at that energy. That being said, the $4s$ band itself has insufficient density to produce scattering transitions that are measurable comparable to $3d$ inner shell scattering transitions seen at lower energy loss. The $3d$ DOS displayed in Figure 5.6 had to be divided by 10 so that the $4s$ DOS would be visible in the figure. However, hybridization with the O $2p$ states to form an *sp* band would significantly increase the number of states at the energies in question. This phenomenon, whereby hybridization of a transition metal with ligand states increases the intensity of $3d$-$4s$ RIXS scattering transitions, has been observed before by MacNaughton *et al.* in their study of metallic DNA [47].

A qualitative look at the RIXS spectra for $FePO_4$ suggests that a high energy loss feature lay within the spectra. However, as mentioned above, the $FePO_4$ spectra are much broader than that of $LiFePO_4$. This innate broadness made impossible any retrieval of useful and reproducible results from the Voigt function fits in the high energy loss areas of the $FePO_4$ spectra.

5.2.2 Magnon-Exciton Coupling

A closer look at the net transition assignments in Figure 5.4 reveals a problem concerning the intensity of the -5.6 eV loss feature compared to the intensity of the -3.0 eV loss feature in the $LiFePO_4$ 709.7 eV spectrum. In short, the -5.6 eV feature appears to be too intense in the experimental spectrum. The -3.0 eV feature has four possible transitions contributing to its strength; in each transition, electrons are scattered from the densest part of the Fe $3d$ occupied spin-up PDOS. The -5.6 eV scattering event also has four possible transitions, but the occupied states are more sparsely populated. The -3.0 eV transition has 360% more occupied states from which electrons may be scattered, yet the measured -3.0 eV peak is only 64% more intense than the -5.6 eV peak. Obviously, the RIXS transition probability matrix elements for the two events are grossly unequal. This inequality is due to the involvement of the spin-down occupied states that help give rise to the -5.6 eV energy loss feature.

Strictly speaking, in pure Russells-Saunders coupling the selection rules for RIXS state that $\Delta S = 0$. Thus, during any scattering event that begins with the $3d$ occupied spin-up states, the scattered electron must flip its spin before coming to rest

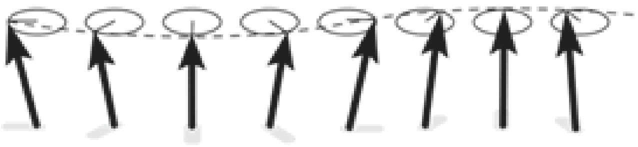

Figure 5.7: Conceptual drawing of a magnon propagating through a crystal. This figure was adapted from the material presented by Ref. 52.

in the spin-down unoccupied states. At finite temperatures, this can be accomplished via magnon-exciton coupling [48–51]. This concept has been used extensively to explain the presence of dipole-allowed peaks in optical absorption spectra. These dipole-allowed peaks should not be present in optical spectra, because of the spin selection rule $\Delta S = 0$. Optical absorption and RIXS share the same $3d$ inner-shell net transition, and like RIXS, dipole-allowed peaks in optical absorption spectra must also obey the spin selection rule. Magnon-exciton coupling allows the electron component of the exciton pair to couple with a magnon, thus flipping the spin of the electron.

A magnon, which is also known as a spin wave, is a quantum of spin that propagates through the crystal with of discrete spin of 1. The wavefront is represented by the sinusoidal pattern of precession of electron spin about the z-axis within the crystal. This concept is displayed in Figure 5.7. The figure shows how the electrons are precessing about the z-axis. The magnon represents how the precession is propagating through the crystal. It should be noted that the precession shows that the electron is varying from a pure eigenstate of the spin Hamiltonian, but this is not the case. The spin state of the electron, if it is sampled, will either be spin-up or spin-down. The variation from straight up or down in the figure is a graphically illuminating, if somewhat misleading, way to show that the spin state of the electron is a linear combination of the pure 1/2 and -1/2 states.

At room temperature, the magnon can be a randomly generated event from heat-induced fluctuations in the spin orientation of an electron. In antiferromagnetic systems, however, the magnon can be deliberately produced through interaction of the magnetic atom being excited by the incoming radiation and another magnetic atom on a neighboring anti-parallel magnetic plane. Either way, transitions that require this mechanism to flip the spin of the excited electron, such as the -3.0 eV transition, rely upon the presence of another particle. Thus the probability that the transition will happen suffers in comparison to a transition that does not require an external mechanism to flip the spin of the electron, such as the -5.6 eV transition. Therefore, magnon-exciton coupling provides the means by which the -3.0 eV transition may occur while simultaneously causing the rate-determining step that limits the probability that the transition will occur. The fact that the -5.6 eV and -3.0 eV features are of comparable size is further evidence that the DOS presented in this thesis are accurate, as the DOS provides a physically reasonable explanation why the -5.6 eV loss is so intense despite the hindrance of low density in the source states.

Chapter 6

Discussion

6.1 Comparison of Theoretical Models

The RIXS data of both $LiFePO_4$ and $FePO_4$ agree extremely well with the PDOS calculated for these systems. However, the quality of agreement between theory and experiment for $LiFePO_4$ is surprising, for two reasons. Firstly, the Fe PDOS displayed in Figures 5.4 and 5.6 assumed $LiFePO_4$ to be ferromagnetic, because the ferromagnetic solution was energetically favorable. This contradicts the experimental evidence that the compound is antiferromagnetic in its ground state [53, 54]. Secondly, the theory that produced the DOS for $LiFePO_4$ and $FePO_4$ was the LDA-based orthogonalized OLCAO approach, which does not explicitly take into account electron correlation effects that cause the large band gaps and insulating behavior demonstrated by many transition metal oxides. As stated in the introduction, there is a debate in the literature as to how to correctly treat these materials, with the argument centering on the question of electron correlation.

Both sides of the debate (correlated vs. uncorrelated functionals) have the support of experimental evidence. To support the uncorrelated DOS, there is the evidence found within the RIXS spectra of the compounds, wherein the presented RIXS spectra and DOS match extremely well. There is also the fact that Xu *et al.* measured an activation energy of 0.36 to 0.50 eV, which fits best with the small band gap solutions [3]. Despite the low activation energy, $LiFePO_4$ has extremely poor conductivity, which is typically characteristic of a wide gap insulator. This supports the solution that incorporates explicit electron correlation effects. Also, optical reflectance measurements presented in the same paper as the wide gap DOS show that the band gap is on the order of 3.8 to 4.0 eV, in accordance with their predicted result. It should be noted, however, that the lowest energy that is displayed in the optical reflectance spectrum is on the order of 2 eV. Although the spectrum shows that the reflectance of $LiFePO_4$ drops off sharply in the vicinity of 3.8-4.0 eV, all this really shows is that crystal begins to absorb more photons at that energy. It does not show that the compound does not begin absorbing photons at earlier energies. Thus, the optical absorption spectrum shown by Xu *et al* does not rule out the possibility that structure near 0.5 eV was simply missed because the energy range did not go low enough.

In another paper by Zhou *et al.*, they showed that LDA-based techniques predict that off-stoichiometric samples of $LiFePO_4$, such as $Li_{0.7}FePO_4$, have a negative enthalpy of formation [55]. A negative enthalpy of formation means that energy is released when the crystal is formed. Exothermic reactions have an better chance of spontaneously occurring than endothermic reactions, therefore it stands to reason that one should observe off-stoichiometric samples spontaneously forming. This has never been observed, at least at room temperature. At room temperature, an incomplete delithiation of $LiFePO_4$ will result in a multi-phase compound with zones of $LiFePO_4$ and $FePO_4$ spread throughout the sample. Zhou and coworkers used this fact to conclude that the uncorrelated calculations were inaccurate. However, this reasoning does not account for activation energy. An exothermic reaction, although energetically favorable, may still not occur if there is insufficient energy in the system to initiate the reaction. Off-stoichiometric compounds, wherein the Fe^{2+} and Fe^{3+} valence states form a solid solution, do occur at higher temperatures, typically within 40 K of 500 K [56]. This implies that the formation of off-stoichiometric solid solutions required more energy than was available at room temperature. However, it is not clear if the reaction was exothermic. Nevertheless, simply considering the enthalpy of formation is insufficient for determining if a reaction will occur.

It would seem that two mutually exclusive scenarios are both accurate. In an attempt to solve this conundrum, Zhou and coworkers suggested that the principle conduction mechanism in $LiFePO_4$ was polaronic in nature. The term polaron was coined to describe a quasiparticle that describes the coupling of an electron with a phonon, or possibly with multiple phonons. A phonon, much like a magnon, represents a quantum of disturbance that propagates through the crystal with a discrete, quantized value for energy. The difference is that a phonon is a quantum of elastic disturbance of the atoms within the crystal from their equilibrium positions. In this way, phonons are the method by which vibrations move through the crystal. The mathematical description of phonons and photons are closely related in that they each are modeled using a quantum simple harmonic oscillator [57]. A polaron is therefore a quasiparticle that forms when an electron that is propagating through the crystal deforms the crystal lattice through electrodynamic interactions with the ions; this deformation is represented by the coupling of the electron to phonons. The number of phonons involved depends upon how strongly the electron interacts with the lattice. A strong interaction results in a large but highly localized deformation of the crystal, and so the superposition of many phonons is required to correctly describe the distortion. This case is known as a small polaron. A large polaron conversely results from weak electron-lattice interaction that causes a small-amplitude but long-range effect [58].

Polarons require a strong electrodynamic interaction with the atoms on the lattice sites, and so strong polaronic effects are usually seen in crystals in which the bonding is mostly ionic in nature. Pure covalent bonding does not leave sufficient charge on the atomic sites to interact with the electron in any meaningful way. The distortion that arises from the interaction of the electron with the ionic lattice changes the nature of the bonding within the area, because the charge density is different. Although the electron has vanishingly small mass compared to the ions on the lattice, nevertheless it has a full unit of charge which carries with it substantial of force on the atomic scale. The lattice seeks a new energy minimum, which to a zeroth approximation means that the positively charged ions will move closer to the electron and the negatively charged ions will move away. This arrangement is energetically favorable given the change in the charge density of the region. However, the distortion builds a potential well that traps the electron in place, because the new lattice arrangement is only energetically favorable with the electron present.

The bonds that the Fe sites in $LiFePO_4$ have with their ligand neighbors have a very low bond order [3]. The bond order is a measure of how many electrons are involved in the covalent bond that two atoms share. A purely covalent single bond, for example, has a bond order of one, whereas a purely covalent double bond has a bond order of two [59]. When the bond is not purely covalent, which can often be the case when there is a large electronegativity difference between the two atoms sharing the bond, then the bond order is no longer a whole integer. A low bond order means the bonding is more ionic than covalent. The $LiFePO_4$ crystal, with its highly ionic, low order bonds, therefore seems to be a suitable environment for polaron formation, at least when the electron resides in the states that are most closely associated with the Fe sites. The supposition of Zhou and coworkers has been supported by the experimental findings of Ellis *et al* [56]. Ellis and coworkers performed Mössbauer spectroscopy on pure $LiFePO_4$ and $FePO_4$ samples, as well as partially delithiated samples. The details of how Mössbauer spectroscopy functions are beyond the scope of this thesis, and will not be discussed here. Suffice is to say here that Mössbauer spectroscopy uses gamma rays to excite nuclear transitions, much as XAS and RIXS techniques use x-rays to excite electronic transitions [60]. However, the gamma rays used to excite the nuclear transitions have hyperfine FWHM, and as such each of the nuclear transitions is individually resolved. The resolution is so fine that the interaction of the nucleus with the electronic environment can be detected. Dynamic interaction of the lattice nuclei with conduction electrons is what brings about polaron formation, so Mössbauer is uniquely suited to the study of polarons. They found that small polarons are an important conduction mechanism in $LiFePO_4$.

Polaron formation has been shown to be the process with constitutes a large part of electron conduction through the $LiFePO_4$ crystal. Polarons do not necessarily adhere to one-electron states calculated by DFT, because they also alter the local density of states. Small polarons in particular, which Ellis *et al.* showed to be the type of polaron present in $LiFePO_4$, severely distort the lattice over a short range. This would alter the local charge density distribution, which also changes the electronic structure according to density functional theory. The polaron idea reconciles the RIXS results, which show that the small band gap solution is correct, with the optical absorption measurements, which show that $LiFePO_4$ has a large band gap. The presence of a polaron reconciles these two mutually exclusive results because the electron promoted to the conduction band changes the band structure such that $LiFePO_4$ has a smaller band gap. The optical absorption measurements were simply probing the onset of a different gap, just not the smallest band gap that could be measured.

A possible variation on this polaron idea may be applicable: a bound magnetic polaron, or possibly a ferron, defines the conductivity. Originally used to account for surprisingly high values of magnetic susceptance in antiferromagnetic samples, bound magnetic polarons are capable of changing the local magnetic environment from antiferromagnetic to ferromagnetic [61–65]. Ferrons have been suggested as the mechanism that hinders conductivity in some antiferromagnetic semiconductors. This idea is intriguing because the ferromagnetic ground state seems to be, in some formalisms, energetically advantageous, although only slightly. This small difference between ferromagnetic and antiferromagnetic alignment may mean that it is relatively easy for conduction electrons to realign the local environment.

This effect is not limited to low temperatures. Ferrons have been predicted to exist at high temperatures even after random fluctuations have mostly destroyed the magnetic ordering of the compound [64]. The bound magnetic polaron effect suggested here and the simple polaron effect suggested by Zhou *et al.* are phenomena that are catalyzed by the presence of impurities [66]. This suggests that $LiFePO_4$ is extremely sensitive to impurity concentration, but this is not a new realization; $LiFePO_4$ has already been proven to be dopant-sensitive by previous efforts.

Whether the polaron is a simple one or something more exotic that alters the local magnetic environment as well as the structural, the implication is the same: The electronic structure that one probes when measuring RIXS spectra is not the ground state electronic structure. Polarons alter the local structure in a way that is completely beyond typical DFT calculations that have been performed for $LiFePO_4$

and $FePO_4$. Unless a DFT calculation is set up to specifically see the effects of altering the lattice positions of the ions, then a DFT calculation will assume the energy of the ion-ion interactions to be a constant value as the electron charge distribution is altered to bring the system to its ground state. Polarons, of course, violate this idea of an unchanging lattice. The potential well that the polaron creates as it changes the lattice means that it requires less energy to excite a polaron. In effect, a polaron sees a smaller band gap than does a conduction electron that does not alter the lattice configuration.

Thus, the presence of a polaron has a profound effect on what one measures. All of the analysis performed thus far strongly suggests that the small band gap solutions in general, and the solution presented by Xu *et al* [3,16] in particular, correctly simulate the total DOS in $LiFePO_4$. However, when the concept of polarons is incorporated into the interpretation of any spectra measured from $LiFePO_4$, it becomes clear that the XAS and RIXS spectra probe only the density of states as seen by a polaron, which does not correspond to the unperturbed one-electron DOS. The degree to which the polaronic and the ground state electronic DOS disagree is not known. It may be that they are very close, and the perturbation to the local crystallographic and/or magnetic structure wrought by the polaron is relatively minor. Regardless of what the band structure was in the ground state, it is clear at this point that the distorted polaronic structure agrees well with the small band gap picture.

This idea, namely that the electronic structure probed by XAS and RIXS experimentation was not the ground state structure, of course implies that the agreement between experiment and theory shown in the previous chapters is entirely accidental. The band structure calculations performed by Xu *et al.* most certainly were not sufficiently robust to account for polaron formation, nor indeed were any band structure simulations performed by any other author. Thus we have entered an interesting realm wherein the simulation is correct even though the physics behind the simulation are incorrect.

Although this concept seems strange, this is not the first time that such a conundrum has been encountered in physics, nor even within this thesis. Twice before discussion has arisen of concepts introduced that simulate spectra properly even as the assumptions behind the simulations were wrong. The Kramers-Heisenberg formula, as a first example, was originally derived without the use of quantum mechanics. Rather, it was derived using the correspondence principle, which was an early attempt to reconcile the wave-particle duality of light. The Kramers-Heisenberg formula was later derived again by Dirac using quantum mechanics and was found to be accurate, despite the erroneous assumptions made at its inception. The second example where accurate simulation can be based upon incorrect physics concerns the -9.1 eV feature. It is clear from the analysis of MacNaughton *et al*, and from the analysis presented here, that such a feature can be readily and easily explained with the use of a $3d$-$4s$ net transition. However, a much more common interpretation is that this feature results from ligand-to-metal electron transfer. It would seem that these two interpretations are mutually exclusive, as both rely upon very different understandings of the Kramers-Heisenberg formula as well as resonant inelastic x-ray scattering as a whole. However, both interpretations simulate the spectrum well.

6.2 Probing Electron Self-Trapping

The concept that the previously displayed XAS and RIXS spectra probed the polaronic structure, which differs in some unknown way from the theorized electronic structure, is intriguing. However, it would seem at first glance that it is impossible to show this conclusively. Any excitation which promotes an electron to the conduction band, or even to continuum states, may provoke the formation of a polaron. Strictly speaking, it is not knowable within the confines of a single x-ray absorption or emission spectrum whether or not one is probing the unperturbed electronic structure without a polaron present. There is a possibility in soft x-ray absorption spectra, because XAS spectra can be measured using multiple techniques. The three techniques of concern here are total electron yield (TEY), total fluorescence yield (TFY), and partial fluorescence yield (PFY). While each of these techniques is supposed to yield the same information as its counterparts because each probes unoccupied local

PDOS, in practice each has unique benefits and limitations that make them applicable in different situations. Therefore, one or more of the three techniques may yield some information about the presence of polarons in $LiFePO_4$ and $FePO_4$. XAS is a great technique to use when searching for polarons, because XAS probes the unoccupied density of states, precisely where polaron formation should occur.

The polaron search experiment was conducted at Beamline 8.0.1 at the Advanced Light Source. The apparatus of Beamline 8.0.1 was described in depth earlier, and so it will not be repeated here. Four samples were measured; these samples were Fe metal (for calibration purposes), $LiFePO_4$, $FePO_4$, and Fe_3P. Each of the samples was excited across the entire Fe $L_{2,3}$ threshold. Fe_3P was measured as part of a different experiment that concerned the effect of impurity concentrations in $LiFePO_4$. The impurity experiment did not yield results of any significance, however the Fe_3P spectra did help shed some light on the $LiFePO_4$ and $FePO_4$ results. The entrance and exit slit widths on either side of the monochromator were set such that the resolving power was set to $E/\Delta E \approx 3000$. At the Fe $L_{2,3}$ edge, this means that one can resolve features that are more than 0.25 eV apart. This resolving power is less than that reported for the XAS spectra shown at the top of Figure 5.1. For that experiment, the resolving power was approximately 4000. The resolving power had to be reduced for the polaron search experiment, because the increased flux was necessary to get decent signal-to-noise ratios for the PFY spectra measured on the three samples of importance. The results of the experiment are displayed in Figure 6.1.

The three panels in Figure 6.1 show the TEY, TFY, and PFY spectra measured from one of $LiFePO_4$, $FePO_4$, and Fe_3P. Vertical dotted lines within each panel line up features that are common to the three spectra. Simple visual inspection is sufficient to note that the three spectra look very different. However, the dotted lines draw attention to a very important point: The three spectra seem to have similar structure, in the sense that local maxima that appear in the TEY also appear in the PFY and TFY spectra. The difference is the relative intensities of the peaks. This is true for $LiFePO_4$, $FePO_4$, and Fe_3P, despite the fact that the TFY, PFY, and TEY

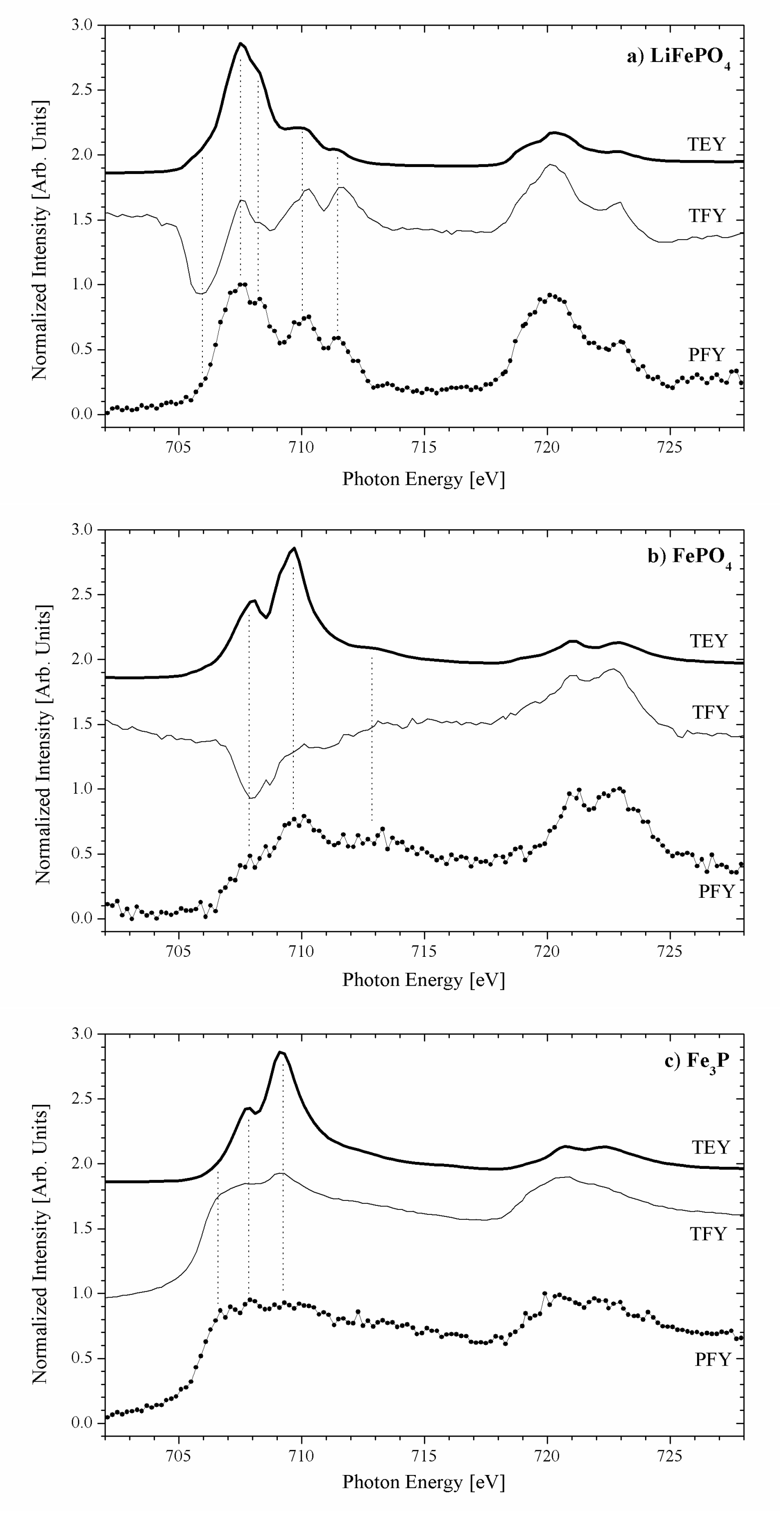

Figure 6.1: XAS spectra of LiFePO$_4$, FePO$_4$, and Fe$_3$P measured using TEY, TFY, and PFY techniques. The heavy lines in each panel are the TEY spectra. The lighter lines and the dotted lines are the TFY and PFY spectra, respectively. The dotted lines in each panel line up important features. In all spectra, the minimum point has been set to 0 and the spectra have been all normalized to 1.

of the first two compounds look so very different from one another.

Figure 6.1 shows that the TFY, PFY, and TEY spectra of $LiFePO_4$ seem to have very stark differences between them. The same can be said for the $FePO_4$ XAS spectra. Although this is highly interesting, the differences one should expect first need to be understood. Although TFY, PFY, and TEY measure the same quantity, namely the probability that an x-ray will be absorbed at a given energy, each technique nevertheless measures this cross-section in a different manner. Therefore, discrepancies are to be expected to a certain degree.

The Fe_3P XAS spectra show the differences that one should expect to see among the three techniques. The TEY spectrum differs quite strongly from the PFY and TFY spectra, and the PFY and TFY spectra look very similar. This makes sense, because recording PFY and TFY spectra entails counting photons that are emitted from the sample. Therefore, any process which affects the cross-section of TFY will affect PFY as well. One such process that affects the measurement of emitted photons is self-absorption. Whenever an atom within a crystal emits a photon through radiative decay of an excited state, that photon could very well be resonantly absorbed by another atom within that same crystal. The more probable a radiative decay is, the more probable it is that the photon will be absorbed by another atom before it can escape the crystal. Self-absorption therefore tends to reduce the size of prominent features while leaving smaller features alone. This generally makes any quantitative analysis of relative peak heights within a photon-out spectrum more difficult to conduct accurately.

Self-absorption would certainly seem to be an important effect in Fe_3P, because the most prominent features seen in the TEY spectrum are severely curtailed in both the TFY and PFY spectra. Although reduced in intensity, the features are still there. TEY does not suffer from self-absorption like photon-out spectra because the electrons emitted by Auger decay cannot be resonantly absorbed in the way that photons can. While it is true that electrons have a very short penetration depth into a crystal, this is because the electron will scatter off valence electrons and steadily lose energy. TFY and PFY are both more bulk sensitive than TEY, which allows photon-out spectra to probe the electronic structure of the bulk. This may grant structure to TFY and PFY spectra that the TEY technique will not have, simply because TEY cannot probe deeply enough.

In short, the TEY, TFY, and PFY spectra of Fe_3P are different from one another, but they differ in ways that are expected. The deeper penetration depth of soft x-rays lends to photon-out processes bulk sensitivity and self-absorption, two effects that will cause differences between photon-out spectra and TEY spectra measured from the same sample. Even with this understanding in mind, however, the differences seen among the three techniques when used on $LiFePO_4$ and $FePO_4$ are spectacular. Of particular interest are the marked dips seen at 706.0 eV in $LiFePO_4$ and at 707.9 eV in $FePO_4$ in the TFY spectra. These dips do not seem possible, because they dip below the pre-edge background threshold. This implies the sample produces less photons when it being excited resonantly than when it is being excited non-resonantly. This is completely counter-intuitive. It also seems remarkable that the PFY spectra of $LiFePO_4$ and $FePO_4$ do not register the same dip. As explained above, the PFY and TFY techniques have more in common with each other than either does with TEY, because both techniques sense emitted photons. However, the $LiFePO_4$ panel in Figure 6.1 in particular shows that the PFY and TEY have more in common than do the PFY and TFY spectra.

The dips in the TFY spectra of $LiFePO_4$ and $FePO_4$ can be understood if one takes into account two important considerations. The first is the nature of the TFY technique. The TFY technique counts the photons coming from the sample, but it does not simply count the photons in the energy range of the edge that is resonantly excited. The Channeltron counts all of the photons within its detection limits. The Channeltron at Beamline 8.0.1 is designed to detect fluorescence photons at all energies that the monochromator at Beamline 8.0.1 can reach. This covers the span of photon energies from 65 to 1400 eV [24]. Note that the Channeltron may be able to detect photons with energies lower than 65 eV, but the true limit to the detection range of the Channeltron is not known. Whatever the lower limit may be, the Channeltron can assuredly detect photons produced by the non-resonant annihilation of core holes created at all excitation thresholds between 65 eV and the Fe $L_{2,3}$ edge. This includes the O K edge, the P $L_{1,2,3}$ edges, and the Fe M_1 edge. Two other possibilities include the Li K edge and the Fe $M_{2,3}$ edges, although these lie at 55 and 53 eV respectively. Although the energy of the incident photons is far off resonance for these other edges, core holes at these edges are still created, and their annihilation produces a constant background signal.

Secondly, one must understand what happens to a photon when it impinges a crystal wherein one of the atomic species is being resonantly excited. The resonantly excited atomic species functions as a photon vacuum; the photons impinging the sample preferentially interact with that atomic species. The other elements within the crystal become starved for photons, and as such their non-resonant photoemission flux rates fall as long as the element in question is being resonantly excited [28].

If the intensity drop in the TFY happens when the ligand states stop interacting with the incident light, than the PFY spectrum should not have recorded the dip because the detection window of the spectrometer is much smaller than that of the Channeltron. All of the low energy photons produced by the lower lying thresholds are not focused by the optical components of the spectrometer onto the MCP. The dip is clearly not in either $LiFePO_4$ or $FePO_4$ PFY spectra, which would indicate that the dip is caused by ligand photoemission suppression.

Although the ligan photoemission suppression scenario explains the data, the problem still remains why it is that the Fe photoemission did not make up the difference. Although the other elements within the $LiFePO_4$ crystal are not producing photons as efficiently, the Fe site is being resonantly excited, and should overcompensate for this drop in ligand photoemission intensity. The problem is made more complex by the fact that this drop in measured intensity is not seen in the TEY spectra of either sample. The PFY spectra do not have any dips, but as discussed earlier, this is due to the method used to detect the photons. TFY and TEY spectra, however, share the common trait that they measure photon emission (TFY) and electron replenishment (TEY) as functions of excitation photon energy. It seems obvious that the Auger decay channel is immune to the effect that is altering the radiative decay channel.

There would seem to be some process which is suppressing the radiative decay channel while simultaneously leaving the Auger decay channel unaffected. It is possible that this effect is due to polaron formation, in particular a magnetic polaron. When the polaron couples to the antiferromagnetic lattice and changes it to a ferromagnetic one, this may cause the spin of the polaron to flip, or possibly cause it to cant sufficiently so that the spin selection rule for radiative decay is no longer satisfied. The participator electron, promoted from the core $2p$ core state to the unoccupied $3d$ band, changes the local crystallographic, electronic, and magnetic environments sufficiently that radiative de-excitation from the altered conduction band becomes much more improbable. In other words, the bound magnetic polaron becomes a metastable state. Of course, the Auger decay process remains unaffected because it does not have the stringent selection rules to which radiative decay must abide [67]. The bound magnetic polaron is not a metastable state to the Auger decay mechanism, and as such the participator electron may refill the core hole. Thus, the TEY spectrum remains unaffected whereas the TFY spectrum is suppressed at certain energies.

For both $LiFePO_4$ and $FePO_4$, the suppression is greatest at the very beginning of the the L_3 edge. The significance of these energies at which the radiative decay suppression is strongest is not known. At the energies indicated, the highest energy core electrons are promoted to the first bound states. These bound states are interesting because they occur before the ionization threshold, although how this property would play into self-trapping or magnetic polaron formation is not understood. The only way to test the theory that the TFY spectra of $LiFePO_4$ and $FePO_4$ show signs of radiative decay channel suppression through bound magnetic polaron formation is to perform simulations which account for such phenomena. Such intensive simulations are certainly beyond the scope of this thesis, if such simulations are even currently possible. It is clear that more work is required.

CHAPTER 7

SUMMARY AND CONCLUSIONS

$LiFePO_4$ and $FePO_4$ were probed using XAS and RIXS techniques to gain greater understanding of the electronic density of states of these two compounds. In particular, this study was motivated by the need to understand the electronic structure that gives rise to the insulating resistivity of $LiFePO_4$. The element-specific techniques of XAS and RIXS, when measured with highly tunable, high resolution synchrotron light, makes this study highly appropriate for understanding local electronic structure within $LiFePO_4$. The electronic structure has been predicted to have an Fe PDOS band gap as small as 0.0 eV, and up to 4.0 eV. The calculations that predict a small gap are collectively called the small gap solutions, as there are several authors that show a band gap of 0.0-1.0 eV. The opposing electronic structure calculations are called the large gap solutions. The band gap varies according to the method with which a particular author calculated the effects of electron correlation. The small gap solutions use electron correlation functionals that are usually more applicable in delocalized systems, whereas the large gaps solutions use the Hubbard U parameter to account for electron correlation in the way preferred for transition metal oxides. The purpose of this study is to see which solution is more accurate.

Voigt functions were fit to the $LiFePO_4$ and $FePO_4$ RIXS spectra. This was done because the individual RIXS features overlapped with one another due to the limited resolving power of the spectrometer, and Voigt function fitting would allow them to be differentiated from one another. Voigt functions were chosen because they are a convolution of Gaussian and Lorentzian profiles; the Gaussian part represents instrumental broadening caused by the sampling apparatus, and the Lorentzian part represents lifetime broadening inherent to the system. Though Voigt peak fitting analysis, it was found that the energy loss features seen in the RIXS spectra correspond very well to Fe $3d$ inner-shell valence-to-conduction band transitions, as predicted by the presented DOS calculations. Evidence was also uncovered for $3d$-$4s$ scattering, which may also lead to charge transfer between the Fe and O sites via the highly hybridized $4s$-$2p$ band.

The success of the small gap solution contradicts expectation, as DFT+U calculations are historically the more accurate method when describing systems such as $LiFePO_4$ and $FePO_4$. The explanation tentatively put forward in this thesis is that our experimental spectra suffer from the effects of a bound magnetic polaron, which would distort the local PDOS and cause a local ferromagnetic environment to form around the excited conduction electron. The presence of polarons in $LiFePO_4$ was already proven in other work, so it is a small leap to believe that polaron formation could influence the DOS probed by the XAS and RIXS techniques.

The polaron could drastically change the local density of states, which is of course because the charge density and the lattice configuration in the local environment are different. This has two very important ramifications. Firstly, the agreement between experiment and the small gap calculation is false, in the sense that the physical assumptions behind the calculation are false. This is referring to the fact that, in the final state of either an XAS or a RIXS excitation, the atom is left in an excited state wherein the local charge density is altered. Therefore, calculations performed with the crystal in the ground state are not accurate. Secondly, any agreement to the large gap solution will also be false. Optical absorption measurements have apparently shown that the band gap is somewhere around 4 eV, but if one takes into account the band structure altering properties of a polaron, it is unknown what that experiment actually probed.

To conclude, a definitive statement as to which band structure calculation regime (small gap vs. large gap) is the more accurate cannot be made. The answer can only be found if one could account for the magnitude of the DOS distortion instigated by the polaron. With this capability, it could then be determined what the ground state DOS was before polaron-induced band structure distortion.

REFERENCES

[1] A. K. Pahdi, K. S. Nanjundaswamy, and J. B. Goodenough. *J. Electrochem. Soc.*, 144:1188, 1997.

[2] G. Ceder, Y.-M. Chiang, D. R. Sadoway, M. K. Aydinol, Y.-I. Jang, and B. Huang. *Lett. Nature*, 392:694, 1998.

[3] Y.-N. Xu, S.-Y. Chung, J. T. Bloking, Y.-M. Chiang, and W.-Y. Ching. *Electrochem. Solid State Lett.*, 7:A131, 2004.

[4] A. Yamada, S. C. Chung, and K. Hinokuma. *J. Electrochem. Soc.*, 148:A224, 2001.

[5] A. S. Andersson, J. O. Thomas, B. Kalska, and L. Häggström. *Electrochem. Solid State Lett.*, 3:66, 200.

[6] A. Deb, U. Bergmann, E. J. Cairns, and S. P. Cramer. *J. Phys. Chem. B*, 108:7046, 2004.

[7] S. Yang, Y. Song, K. Ngala, P. Y. Zavalij, and M. S. Whittingham. *J. Power Sources*, 119-121:239, 2003.

[8] M. Takahashi, H. Ohtsuka, K. Akuto, and Y. Sakurai. *J. Electrochem. Soc.*, 152:A899, 2005.

[9] M. Takahashi, S. Tobishima, K. Takei, and Y. Sakurai. *J. Power Sources*, 97-98:508, 2001.

[10] N. Ravetand Y. Chouinard, J. F. Magnan, S. Besner, M. Gauthier, and M. Armand. *J. Power Sources*, 97-98:503, 2001.

[11] K. Amine, J. Liu, and I. Belharouak. *Electrochem. Comm.*, 7:669, 2005.

[12] C. H. Mi, G. S. Cao, and X. B. Zhao. *Mat. Lett.*, 59:127, 2005.

[13] S.-Y. Chung, J. T. Bloking, and Y.-M. Chiang. *Nat. Mater.*, 1:123, 2002.

[14] S. Shi, L. Liu, C. Ouyang, D.-S. Wang, Z. Wang, L. Chen, and X. Huang. *Phys. Rev. B*, 68:195108, 2003.

[15] D. Wang, H. Li, S. Shi, X. Huang, and L. Chen. *Electrochem. Acta*, 50:2955, 2005.

[16] Y.-N. Xu, W.-Y. Ching, and Y.-M. Chiang. *J. Applied Physics*, 95:6583, 2004.

[17] P. Tang and N. A. W. Holzwarth. *Phys. Rev. B*, 68:165107, 2003.

[18] S. Shi, C. Ouyang, Z. Xiong, L. Liu, Z. Wang, H. Li, D.-S. Wang, L. Chen, and X. Huang. *Phys. Rev. B*, 71:144404, 2005.

[19] F. Zhou, K. Kang, T. Maxisch, G. Ceder, and D. Morgan. *Solid State Comm.*, 132:181, 2004.

[20] A. L. Robinson. *X-ray Data Booklet*, chapter 2.2 History of Synchrotron Radiation, pages 17–23. Lawrence Berkeley National Laboratory and Univeristy of California, Berkeley, CA, 2nd edition edition, 2001.

[21] *Synchrotron Science: How is synchrotron light created?* Australian Synchrotron, http://www.synchrotron.vic.gov.au/.

[22] Kwang-Je Kim. *X-ray Data Booklet*, chapter 2.1 Characteristics of Synchrotron Radiation, pages 1–16. Lawrence Berkeley National Laboratory and Univeristy of California, Berkeley, CA, 2nd edition edition, 2001.

[23] D. Attwood. *Soft X-rays and Extreme Ultraviolet Radiation: Principles and Applications*. Cambridge University Press, Cambridge, UK, 2000.

[24] *Beamlines at the ALS*. Lawrence Berkeley National Laboratory, Univeristy of California, http://www-als.lbl.gov/.

[25] *What is a spectrograph?* Andor Technology, http://www.andor.com/.

[26] H. A. Rowland. *Phil. Mag.*, 13:469, 1882.

[27] W. B. Peatman. *Gratings, Mirrors, and Slits: Beamline Design for Soft X-ray Synchrotron Radiation Sources*. Overseas Publishers Association, Amsterdam B.V., 1997.

[28] A. Moewes, E. Z. Kurmaev, D. L. Ederer, and T. A. Callcott. *Phys. Rev. B*, 62:15427, 2000.

[29] P. L. Cowan. *Resonant Anomalous X-ray Scattering: Theory and Applications*, chapter Resonant X-ray Raman scattering from atoms and molecules, page 449. Elsevier Science B. V., 1994.

[30] H. A. Kramers and W. Heisenberg. *Zeitschrift f. Physik*, 48:15, 1925.

[31] G. Breit. *Rev. Mod. Phys.*, 4:504, 1932.

[32] Jorge Kohanoff. *Electronic Structure Calculations for Solids and Molecules: Theory and Computational Methods*. Cambridge University Press, New York, 2006.

[33] W. Y. Ching and Chun C. Lin. *Phys. Rev. B*, 12:5536, 1975.

[34] X.-F. Zhong, Y.-N. Xu, and W. Y. Ching. *Phys. Rev. B*, 41:10545, 1990.

[35] E. Wigner. *Phys. Rev.*, 46:1002, 1934.

[36] E. Wigner. *Trans. Faraday Soc.*, 34:678, 1938.

[37] E. Wimmer, A. Neckel, and K. Schwarz. *J. Phys. C: Solid State Phys.*, 12:5441, 1979.

[38] E. Z. Kurmaev, A. Moewes, L. Ouyang, L. Randaccio, P. Rulis, W. Y. Ching, M. Bach, and M. Neumann. *Europhys. Lett.*, 62:582, 2003.

[39] R. M. Martin. *Electronic Structure: Basic Theory and Practical Methods*. Cambridge University Press, Cambridge, UK, 2004.

[40] J. J. Jia, T. A. Callcott, J. Yurkas, A. W. Ellis, F. J. Himpsel, M. G. Samant, J. Sthr, D. L. Ederer, J. A. Carlisle, E. A. Hudson, L. J. Terminello, and D. K. Shuh. *Rev. Sci. Instrum.*, 66:1394, 1995.

[41] A. Moewes, E. Z. Kurmaev, L. D. Finkelstein, A. V. Galakhov, S. Gota, M. Gautier-Soyer, J. P. Rueff, and C. F. Hague. *J. Phys.: Cond. Matter*, 15:2017, 2003.

[42] E. Z. Kurmaev, A. L. Ankudinov, J. J. Rehr, L. D. Finkelstein, P. F. Karimov, and A. Moewes. *J. Elec. Spec. Rel. Phen.*, 148:1, 2005.

[43] Z. B. Alfassi, Z. Boger, and Y. Ronen. *Statistical Treatment of Analytical Data*. Blackwell Science Ltd., 9600 Garsington Road, Oxford, UK OX4 2DQ, 2005.

[44] D. Muir. Design of a high performance soft x-ray emission spectrometer for the reixs beamline at the canadian light source. Master's thesis, University of Saskatchewan, Saskatoon, Saskatchewan, 2006.

[45] A. Augustsson, G. V. Zhuang, S. M. Butorin, J. M. Osorio-Gullien, C. L. Dong, R. Ahuja, C. L. Chang, P. N. Ross, J. Nordgren, and J.-H. Guo. *J. Chem. Phys.*, 123:184717, 2005.

[46] A. Moewes, S. Stadler, R. P. Winarski, D. L. Ederer, M. M. Grush, and T. A. Callcott. *Phys. Rev. B*, 58:R15951, 1998.

[47] J. B. MacNaughton, M. V. Yablonskikh, A. H. Hunt, E. Z. Kurmaev, J. S. Lee, S. D. Wettig, and A. Moewes. *Phys. Rev. B.*, 74:125101, 2006.

[48] R. J. Elliot, M. F. Thorpe, G. F. Imbusch, R. Loudon, and J. B. Parkinson. *Phys. Rev. Lett.*, 21:150, 1968.

[49] S. Freeman and J. J. Hopfield. *Phys. Rev. Lett.*, 21:910, 1968.

[50] R. S. Meltzer, M. Y. Chen, D. S. McClure, and M. Lowe-Pariseau. *Phys. Rev. Lett.*, 21:913, 1968.

[51] M. F. Thorpe. *Phys. Rev. Lett.*, 23:472, 1969.

[52] *Highlight of Yamashita Team at 6th Research Area Meeting: Observation of the Collective Magnetic Excitation in the Single-Chain Magnet.* Japan Science and Technology Agency, http://www.nanostruct-mater.jst.go.jp/.

[53] R. P. Santoro and R. E. Newnham. *Acta Crys.*, 22:344, 1967.

[54] G. Rousse, J. Rodriguez-Carvajal, S. Patoux, and C. Masquelier. *Chem. Mater.*, 15:4083, 2003.

[55] F. Zhou, C. A. Marianetti, M. Cococcioni, D. Morgan, and G. Ceder. *Phys. Rev. B*, 69:201101, 2004.

[56] B. Ellis, L. K. Perry, D. H. Ryan, and L. F. Nazar. *J. Am. Chem. Soc.*, 128:11416, 2006.

[57] Charles Kittel. *Introduction to Solid State Physics.* John Wiley and Sons, Hoboken, NJ, 7th edition, 1996.

[58] A. S. Alexandrov and Sir Nevill Mott. *Polarons and Bipolarons.* World Scientific Publishing Company, Singapore, 1995.

[59] R. H. Petrucci, W. S. Harwood, and F. G. Herring. *General Chemistry: Principles and Modern Applications.* Prentice-Hall, Upper Saddle River, New Jersey 07458, 8th edition, 2002.

[60] A. Maddock. *Mössbauer spectroscopy: principles and applications.* Horwood Publishing, Chichester, United Kingdom, 1997.

[61] T. Kasuaya, A. Yanase, and T. Takeda. *Solid State Comm.*, 8:1543, 1970.

[62] T. Kasuaya. *Solid State Comm.*, 8:1635, 1970.

[63] A. Mauger and D. L. Mills. *Phys. Rev. B*, 31:8024, 1985.

[64] E. L. Nagaev. *Phys. Rev. B*, 60:R6984, 1999.

[65] I. Gonzalez, J. Castro, D. Baldomir, A. O. Sboychakov, A. L. Rakhmanov, and K. I. Kugel. *Physica B*, 359-361:1418, 2005.

[66] I. G. Austin and N. F. Mott. *Adv. Phys.*, 50:757, 2001.

[67] J. J. Lander. *Phys. Rev.*, 91:1382, 1953.